ÇUKUROVA UNIVERSITY
INSTITUTE OF NATURAL AND APPLIED SCIENCES

PhD THESIS

Evrim Ersin KANGAL

SEACRH FOR DARK MATTER AND LARGE EXTRA DIMENSIONS IN MONOJET EVENTS IN pp COLLISIONS AT $\sqrt{s}$ = 8 TeV

DEPARTMENT OF PHYSICS

ADANA, 2013

ÇUKUROVA UNIVERSITY
INSTITUTE OF NATURAL AND APPLIED SCIENCES

SEACRH FOR DARK MATTER AND LARGE EXTRA DIMENSIONS IN MONOJET EVENTS IN pp COLLISIONS AT $\sqrt{s}$ = 8 TeV

Evrim Ersin KANGAL

A THESIS OF DOCTOR OF PHİLOSOPHY

DEPARTMENT OF PHYSICS

We certify that the thesis titled above was reviewed and approved for the award of degree of the Doctor of Philosophy (PhD) by the board of jury on 10/09/2013.

………………....................	………………………………….	....
Prof. Dr. İsa DUMANOĞLU	Prof. Dr. Aysel Kayiş TOPAKSU	Prof. Dr. Sefa ERTÜRK
SUPERVISOR	MEMBER	MEMBER

………………...................	……………………………...
Prof. Dr. Ayşş POLATÖZ	Asst.Prof. Dr. Sezgin AYDIN
MEMBER	MEMBER

This PhD Thesis is written at the Department of Institute of Natural And Applied Sciences of Çukurova University.
Registration Number:

Prof. Dr. Mustafa GOK
Director
Institute of Natural and Applied Sciences

This study was supported by Çukurova University Scientific Research fund.
Project Number: FEF2011D24

ABSTRACT

PhD THESIS

SEACRH FOR DARK MATTER AND LARGE EXTRA DIMENSIONS IN MONOJET EVENTS IN pp COLLISIONS AT $\sqrt{s}$ = 8 TeV

Evrim Ersin KANGAL

ÇUKUROVA UNIVERSITY
INSTITUTE OF NATURAL AND APPLIED SCIENCES
DEPARTMENT OF PHYSICS

Supervisor :Prof. Dr. İsa DUMANOĞLU
Year: 2013, Pages: 131
Jury :Prof. Dr. Aysel Kayış TOPAKSU
:Prof. Dr. Sefa ERTÜRK
:Prof. Dr. Ayşe POLATÖZ
:Asst. Prof. Dr. Sezgin AYDIN

We present a search for new physics in the final state containing a single jet and missing transverse energy using pp collision data at 8 TeV at the LHC. The data sample is collected by the CMS detector, corresponding to an integrated luminosity of 19.5 fb^{-1}. The number of observed events is in agreement with the Standard Model prediction. Limits are set on parameters of models of dark matter and large extra dimensions.

Key Words: Dark Matter, Extra Dimension, ADD Model, LHC, CMS, Mono-Jet.

ÖZ

DOKTORA TEZİ

$\sqrt{s}$ = 8 TeV *pp* ÇARPIŞMALARINDA TEK-JET OLAYLARINDA KARANLIK MADDE VE EKSTRA BOYUT ARAŞTIRMALARI

Evrim Ersin KANGAL

ÇUKUROVA ÜNİVERSİTESİ
FEN BİLİMLERİ ENSTİTÜSÜ
FİZİK BÖLÜMÜ

Danışman :Prof. Dr. İsa DUMANOĞLU
Yıl: 2013, Sayfa: 131
Jüri :Prof. Dr. Aysel Kayış TOPAKSU
:Prof. Dr. Sefa ERTÜRK
:Prof. Dr. Ayşe POLATÖZ
:Asst. Prof. Dr. Sezgin AYDIN

Büyük Hadron Çarpıştırıcısında (BHÇ) 8 TeV kütle merkezi enerjisinde *pp* çarpışmalarından alınan veri ile yüksek enerjili bir jet ve bunu dengeleyen dik momentum içeren olaylar araştırılmıştır. Işıklılık değeri 19.5 fb^{-1} olan veriler CMS detektörü tarafından kaydedilmektedir. Gözlenen olay sayıları Standart Modelin öngörüsü ile uyumludur. Karanlık madde ve ekstra boyut modellerinin parametrelerinin limitleri belirlenmiştir.

Anahtar Kelime: Karanlık Madde, Ekstra Boyut, LHC, CMS, Tek-Jet.

ACKNOWLEDGEMENTS

I wish to thank my advisor, İsa DUMANOĞLU, for his encouragement and guidance during my PhD. program.

I sincerely thank my thesis committee for their precious suggestions.

I thank the mono-jet group members especially Shuichi KUNORİ, Steven WORM, Mehmet VERGİLİ, Bayram TALİ, Yalçın GÜLER, Ümit KAYA and Anwar BHATTİ for their suggestions.

Finally I thank my dear family for their love and Selime KILIÇ.

CONTENTS **PAGE**

LIST OF TABLES **PAGE**

LIST OF FIGURES **PAGE**

ABBREVIATIONS

ADD Model	: Arkani-Hamed Dimopoulos Dvali's Model
ALEPH	: Apparatus for LEP Physics
ALICE	: A Large Ion Collider Experiment
ATLAS	: A Toroidal LHC ApparatuS
CDF	: Collider Detector at Fermilab
CMS	: Compact Muon Solenoid
SST	: Silicon Strip Tracker
TIB	: Tracker Inner Barrel
TOB	: Tracker Outer Barrel
TEC	: Tracker End Caps
TID	: Tracker Inner Disks
ECAL	: Electromagnetic Calorimeter
HCAL	: Hadron Calorimeter
HB	: Hadronic Barrel
HE	: Hadronic Endcap
HO	: Hadronic Outer
CTF	: Combinatorial Track Finder
GSF	: Gaussian Sum Filter
DAF	: Deterministic Annealing Filter
MTF	: Multi Track Finder
QED	: Quantum ElectroDynamics
QCD	: Quantum ChromoDynamics
LHC	: Large Hadron Collider
UE	: Underlying Event
PU	: PileUp
CMSSW	: CMS Software
PF	: Particle Flow
DM	: Dark Matter
GR	: General Relativity

SR	: Special Relativity
SM	: Standard Model
EW	: ElectroWeak
FRW	: Flat Robertson-Walker
WIMP	: Weakly Interacting Massive Particle
SI	: Spin Independent
SD	: Spin Dependent
PDF	: Parton Distribution Function
BS	: Bjorken Scale
EFT	: Effective Field Theory
JES	: Jet Energy Scale
MC	: Monte Carlo

1. THE COMPACT MUON SOLENOID DETECTOR

The Compact Muon Solenoid (CMS) experiment is one of the largest particle detectors. It has 22 m length and 16 m diameter. The detector consists of various subdetectors which are arranged in layers around the interaction point. CMS consists of a central barrel which is arranged symmetrically around the interaction point and so-called Endcaps on the both sides of the barrel. Detector components are aligned perpendicular to the beam pipe in the Endcaps.

CMS detector has a tracker, an electromagnetic calorimeter, a hadronic calorimeter, a magnet system and the muon system. These systems are explained in more detail in the following sections.

1.1. Tracker System

One of the methods of calculating the momentum of a particle is to track its trajectory through a magnetic field. If particle has a more curved the path, the momentum of particle will be less or vice versa. The CMS tracker records the trajectory of charged particles by finding their positions at certain points. The tracker is geometrically divided into several substructures; pixel and silicon strip detectors (Bayatian, 1998).

1.1.1. Pixel Detector

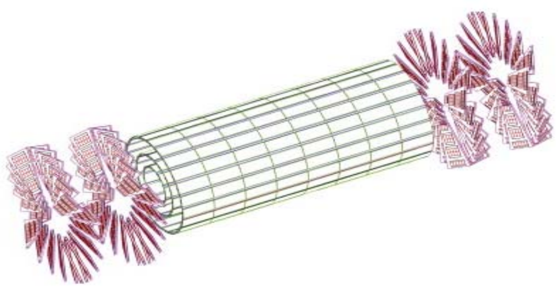

Figure 1.1. CMS tracker pixel detector.

The pixel detector consists of three cylindrical layers surrounding the interaction point. They have same length of 53 cm but different radius like 4.4, 7.3 and 10.2 cm. Also, you can find two endcaps disks which are built from pixel detector. They are located on each side at 34.5 cm and 46.5 cm with the radius from 6 to 15 cm (CMS Collaboration, 2008).

1.1.2. Strip Detectors

The Silicon Strip Tracker (SST) (Manfred KRAMMER, 2010) covers the mean radius from 20 cm to 110 cm. The SST is divided into four sub detectors which are called the Tracker Inner Barrel (TIB), the Tracker Outer Barrel (TOB), the Tracker EndCaps (TEC) and the Tracker Inner Disks (TID), respectively. The TIB covers radius from 20 cm to 64 cm with four layers using sensors with a thickness of 320 µm and a strip pitch of 80 µm to 120 µm. The TOB consists of six layers and covers radius up to 110 cm. The TEC cover both ends of the tracker. The TID consists of 3 small disks with 3 rings of modules.

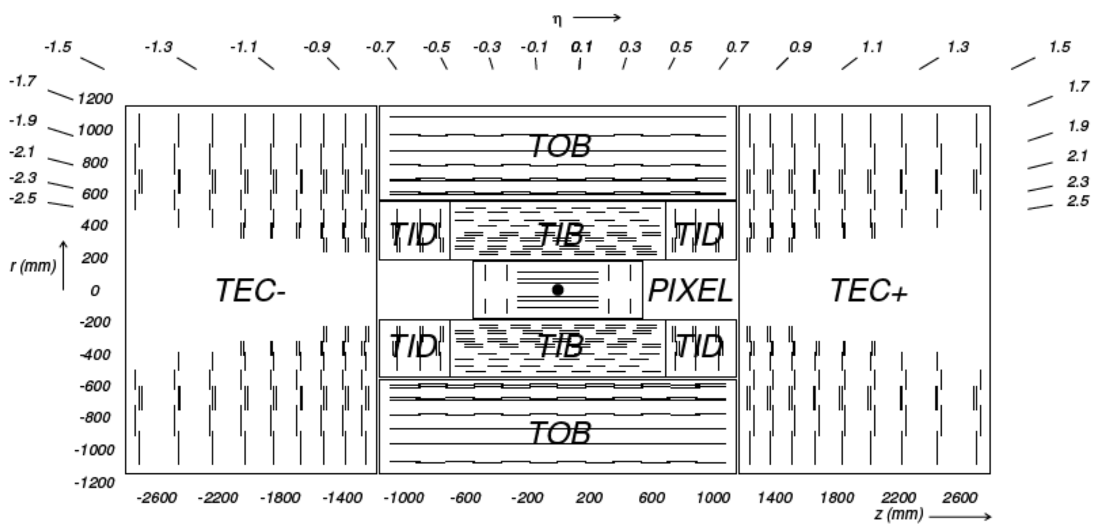

Figure 1.2. The silicon strips tracker is composed of multiple components: the TIB region with 4 layers, the TID region with 3 layers, the TOB region with 6 layers and the TEC regions with 9 layers.

1.2. Electromagnetic Calorimeter

CMS has an Electromagnetic Calorimeter (ECAL). The aim of using this calorimeter is to stop and measure the energy of electromagnetically interacting particles, i.e. photons and charged particles. The ECAL consists of about 70,000 crystals of lead-tungstate, PbWO4. Charged particles emit photons via bremsstrahlung when they traverse them. Photons create electron-positron pairs which then create bremsstrahlung photons again. This process repeats until the energy of the particles is below the pair production threshold. The PbWO4 has a short radiation length ($\chi_0 = 0.89\ cm$) because of its high density ($8.2\ g/\mathrm{cm}^3$) and the Molière radius is very small ($R_M = 2.19\ cm$) allowing to design a compact calorimeter for narrow showers (Bayatian, 1997a).

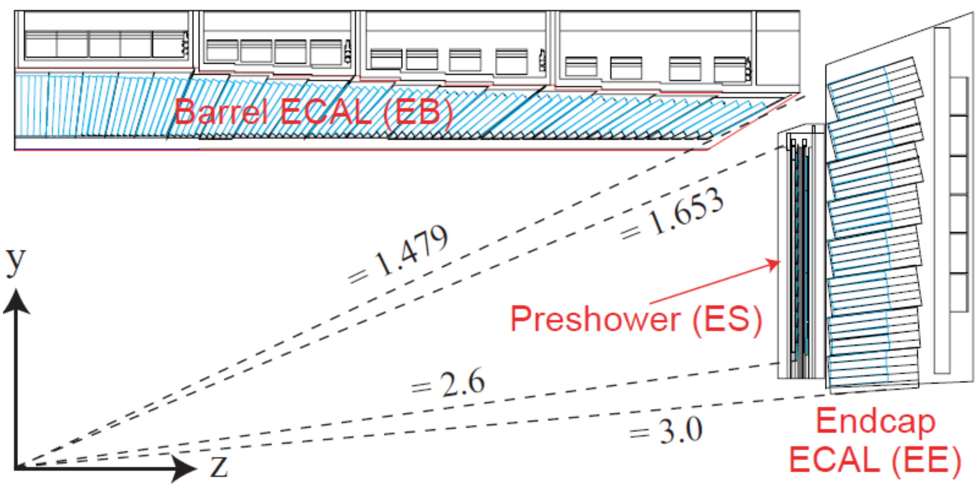

Figure 1.3. CMS electromagnetic calorimeter.

1.3. Hadronic Calorimeter

The Hadronic Calorimeter (HCAL) measures the energy of hadrons. Hadron is particles which are made of quarks and gluons, for example protons, neutrons, pions and kaons. The HCAL calorimeter consists of four subdetectors: Hadronic Barrel, Hadronic EndCap, Hadronic Outer and Hadronic Forward (Bayatian, 1997b).

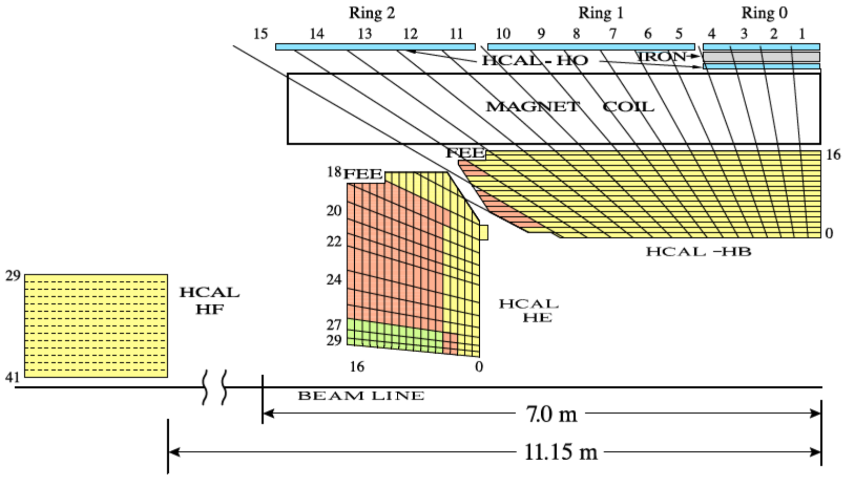

Figure 1.4. CMS Hadronic calorimeter.

1.4. Magnet System

The CMS detector is built around a huge solenoid magnet. The magnet is a cylindrical coil of superconducting cable and it generates 3.8 Tesla magnetic field which is almost 100000 times the magnetic field of the Earth. There is a steel "yoke" which confines the field (Bayatian, 1997c).

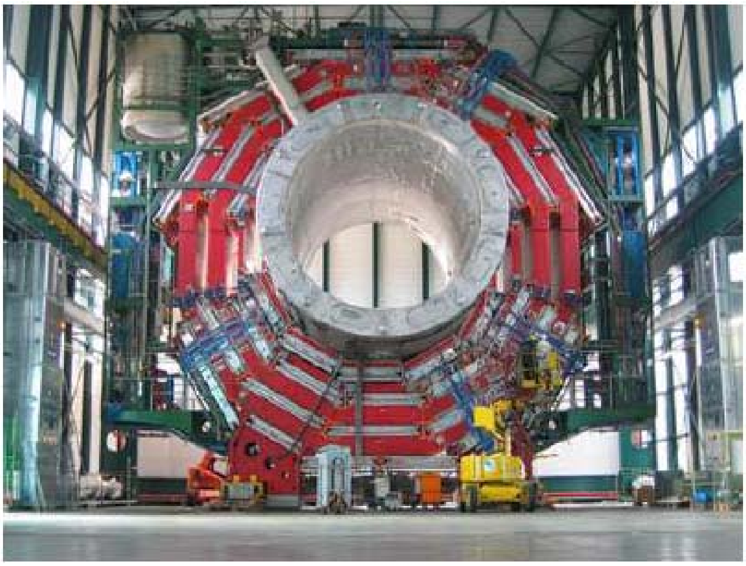
Figure 1.5. CMS superconducting magnet.

1.5. Muon System

Behind the hadronic calorimeter only minimum ionizing particles have not yet been stopped. Apart from neutrinos, which cannot be detected by CMS, the only stable particles that can reach this point are muons. Therefore, outside of the hadronic calorimeter and also outside of the magnet coil, additional detector components have been installed. They are commonly referred to as the muon system and they are dedicated for identifying muons and increasing precision of the measurement of muon tracks. The muon system covers a pseudo rapidity range of $|\eta| < 2.4$ (Bayatian, 1997d).

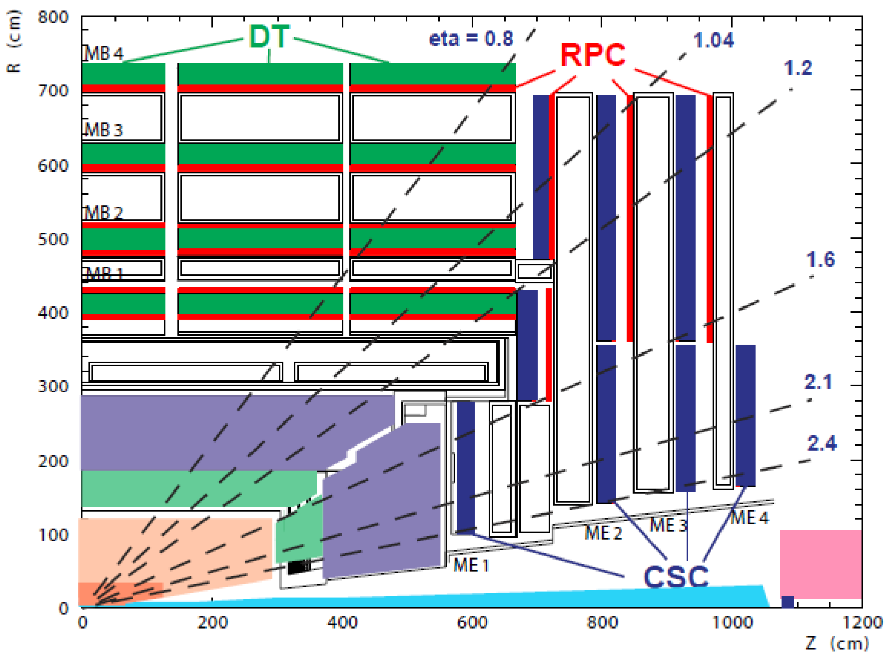

Figure 1.6. CMS muon system.

2. EVENT RECONSTRUCTION

Individual hits in the detector components are reconstructed through the following procedures.

2.1. Track Fitting

Hits in the silicon pixel and strip detectors are combined to tracks of charged particles. The fit starts with three subsequent hits in the innermost layers of the detector. The search stops when the end of the tracker is reached or no more hits are found. Eventually, a curved track is fitted to the whole collection of hits in order to obtain the track parameters from which particle properties such as its four-momentum can be deduced.

The algorithm described above is called the Combinatorial Track Finder (CTF) (CMS Collaboration, 2010) and is used for track reconstruction in CMS. There exist other algorithms such as the Gaussian Sum Filter (GSF) (Wolfgang Adam, R Frühwirth, Are Strandlie, and T Todor, 2005), the Deterministic Annealing Filter (DAF) or the Multi Track Finder (MTF) which can be used for special purposes such as electron reconstruction or track reconstruction in jets (J.R. Vlimant, 2007).

2.2. Vertex Reconstruction

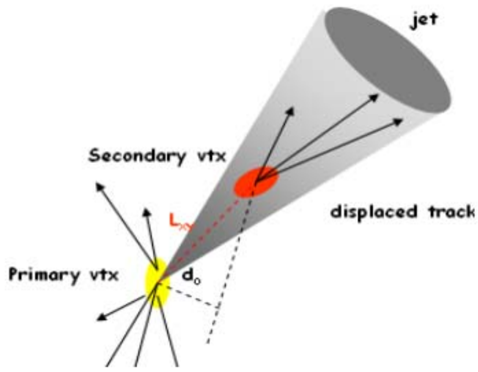

Figure 2.1. Primary interaction vertex.

A primary interaction vertex in Fig. 2.1 is the point in space where the collision of two protons occurred (R Frühwirth, Wolfgang Waltenberger, and Pascal Vanlaer, 2007). The points of subsequent decays of collision products are called secondary vertices. Primary vertices can be reconstructed by finding a common set of tracks which can be extrapolated to the same position within the beam pipe. The vertex position is fitted based on candidate tracks with an adaptive vertex fit.

2.3. Jet

When a high-energetic quark or gluon is created in particle collisions, their energy is high enough to produce one quark-antiquark pair. This leads to the formation of a whole bunch of hadrons all of which move into approximately the same direction. Such a bunch is called a jet.

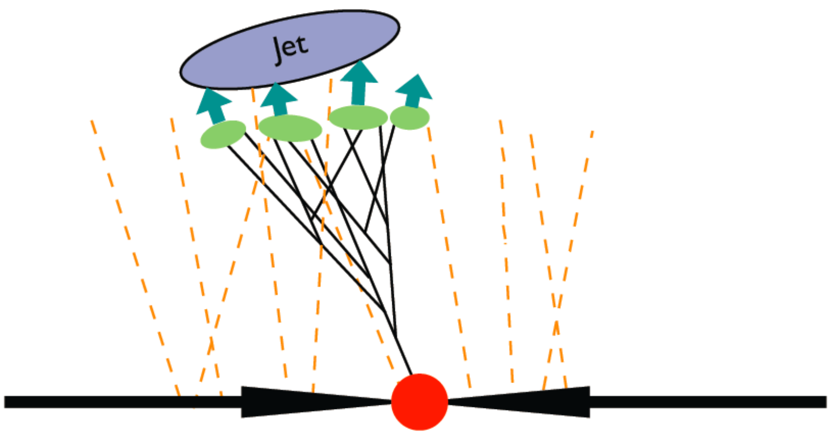

Figure 2.2. Jet productions.

In Fig. 2.2, background radiation (underlying event and/or pileup) can affect jets momentum in at least two ways:

- Some background radiation will be clustered with the jet, increasing its momentum.

- Some hard particles (from the parton fragmentation process) may not cluster with the rest of the jet because of the disturbing presence of other nearby particles (they will form other jets with them).

2.3.1. Effects of Jet Radius

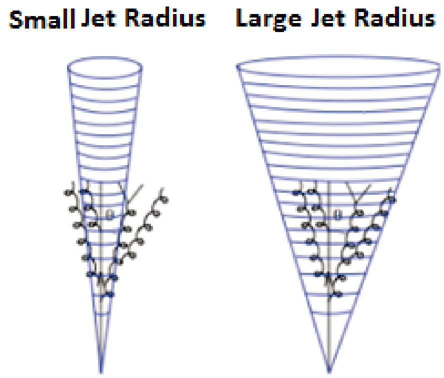

Figure 2.3. Perturbative radiations in jet area.

The perturbative radiation in Fig. 2.3 is coming from the coupling constant which determines the area of phase-space in Feynman diagrams. This is not a problem in Quantum Electrodynamics (QED) but it is a problem in the Quantum Chromodynamics (QCD) because of asymptotic freedom. Because of that there are many perturbative radiations at Large Hadron Collider (LHC). So, there will be many events with perturbative radiation. Whether the emitted particle due to this radiation should be observed in jet's area depending on its radius.

- if jet's radius is big enough, this particle will appear in the jet's area.
- if jet's radius is small enough, this particle will not enter the jet's area.

So, the energy of the jet will be affected in both cases. This effect can be written as;

$$\Delta P_T \cong \frac{\alpha_s(C_A,C_F)}{\pi} P_T \ln R \qquad 2.1$$

where C_F is strength of gluon coupling to quarks, C_A is strength of gluon self-coupling, α_s is strong coupling constant, R is cone radius and P_T is jet momentum. According to eq. 2.1, contribution of perturbative radiation is proportional with logarithm of R.

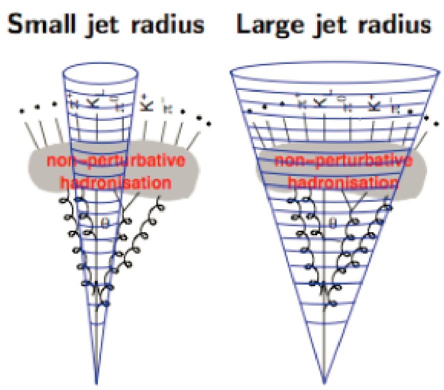

Figure 2.4. Hadronization of non-perturbative radiations in a jet area.

Hadronization in Fig. 2.4 is a process in which hadrons are formed out of quarks and gluons in particle physics. This can happen after colliding particles at high energies in a particle collider and in this case free quarks or gluons can be created. This particle-flow is known as hadronization. So, detector should measure the energy of these particles. This means that bigger the radius, better the energy record in calorimeter. A relation between deposited energy and radius (R) is given as

$$\Delta P_T \cong -\frac{\alpha_s(C_A, C_F)}{R} \times 0.4\, GeV. \quad 2.2$$

According to eq. 2.2, contribution from hadronization is inversely proportional to R. So, it is small effect for big radius but it is big for small radius.

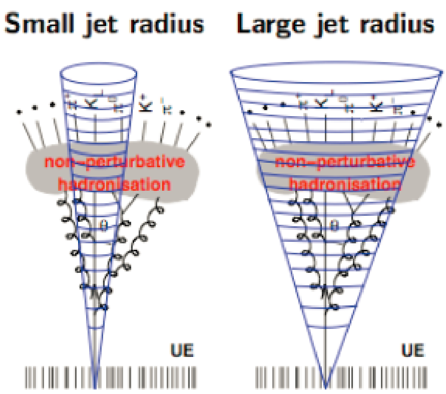

Figure 2.5. Underlying event in jet area.

Sometimes, soft interactions will happen at proton-proton collisions. These interactions give rise to contamination of the jet area (see Fig. 2.5). So, if jet's radius gets bigger, it will be worse for its energy. Because jet area starts to cover these interactions. In other words, relation is given as;

$$\Delta P_T \cong \frac{R^2}{2} \times 15\ GeV. \qquad 2.3$$

Bigger radius gives rise to more contamination of jet area (Matteo Cacciari, 2012).

2.3.2. Definition of Jet Area

The underlying event (UE) and pileup (PU) can affect a jet in two different ways. If particles from the UE and PU were clustered into the jet, then this would increase transverse momentum of the jet. On the other hand the presence of the UE/PU particles can change the way of clustering particles which are created from hard scattering. In order to study the first effect, it should be introduced the concept of the 'jet area'. So, a good measure of a jet's susceptibility to contamination due to UE and PU should be given by the region of jet area. This measure is called as the jet's "catchment area" (Matteo Cacciari, Gavin P. Salam, Gregory Soyez, 2008). For this area, there are two definitions.

- **Passive Area (Point-like Radiation)**

Suppose an event composed of a set of particles P_i which are clustered into a set of jets J_i. In this case, one adds a single infinitely soft ghost particle g which has rapidity of y and azimuthal angle of φ to the P_i and repeats the jet-finding. As long as the jet algorithm is infrared safe, the set of jets J_i should be not changed by this operation. So, the passive area of the jet J can be defined as a scalar;

$$A(J) = \int dy\, d\varphi\, f(g(y,\varphi),J) \qquad 2.4$$

where

$$f(g(y,\varphi),J) = \begin{cases} 1 & g \in J \\ 0 & g \notin J \end{cases}. \qquad 2.5$$

- **Active Area (Diffuse Radiation)**

In this case, a set of ghosts added to the event, with density v_g (per unit area). If n_j ghosts are clustered with a jet J, its area to that set of ghosts will be $\frac{n_j}{v_g}$. We then define the active jet area of J as the limit of $\langle\frac{n_j}{v_g}\rangle$, averaged over all ghosts distributions, when v_g goes to infinity, i.e. in the limit of infinitely dense ghost coverage. So, jet area is written as sum over number of cluster like;

$$A(J) = \sum_i lim_{v_{g_i}\to\infty} \langle\frac{n_{J_i}}{v_{g_i}}\rangle. \qquad 2.6$$

2.3.3. Jet Algorithm

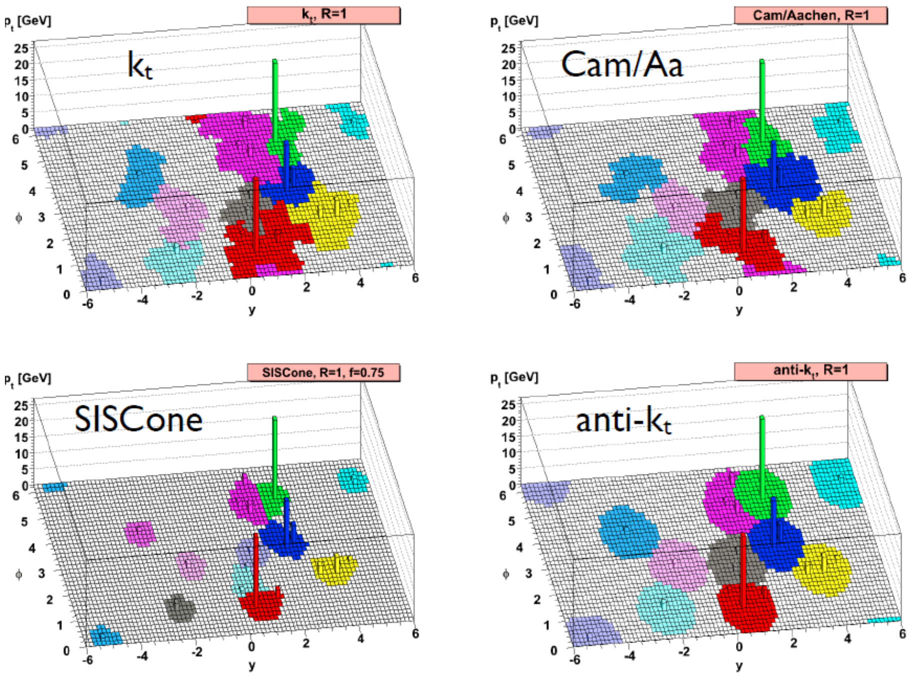

Figure 2.6. Algorithms of jet.

The jet is defined by an algorithm. There are two kind of algorithm whose names are Cluster and Cone algorithms (see Fig 2.6).

- **Cluster Algorithms**

This algorithm starts from all the elementary objects available and performs an iterative clustering to build larger objects. This algorithm has three kinds whose names are k_t, anti-k_t (S. Catani, Yu. L. Dokshitzer, M. H. Seymour, and B. R. Webber, 1993) and Cambridge/Aachen (Stan Bentvelsen and Irmtraud Meyer, 1998).

- **Cone Algorithms**

This generally seeks to find geometric regions which maximize the momentum in a given area. So, there is one cone algorithm whose name is SISCone (Gavin P. Salam and Gregory Soyez, 2007).

So we have four different types of algorithm for defining a jet. But each has a different jet area. Let's try to understand this effect.

Table 2.1. Comparison of jet area for different algorithms.

Areas	$\boldsymbol{k_t}$	**Cam/Aa**	**SISCone**	**anti-$\boldsymbol{k_t}$**
$A/_{\pi R^2}$	0.81	0.81	0.25	1

According to Table 2.1, the best algorithm is anti-k_t because ratio is equal to one. So, anti-k_t generates a circular hard jet as can be seen from Fig. 2.6 and only the softer jets have more complex shapes. On the other hand, for SISCone, single-particle jets are regular while composite jets have more varied shapes (see Fig. 2.6).

2.4. Muon Reconstruction

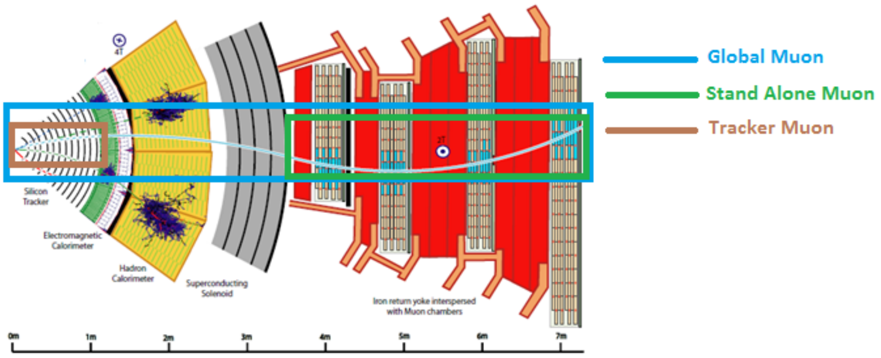

Figure 2.7. Muon reconstruction.

There are three steps for muon reconstruction (see Fig. 2.7). Firstly, tracker muon is defined in the silicon tracker region. Next, stand-alone muons should be found in the muon system alone. After that, the tracks from the muon chambers are extrapolated to tracks from the silicon tracker region in order to find a matching track. When such a match can be found, a global fit between the tracker and muon chamber system can be done and this fit is a called global muon (CMS Collaboration, 2013).

2.5. Particle Identification

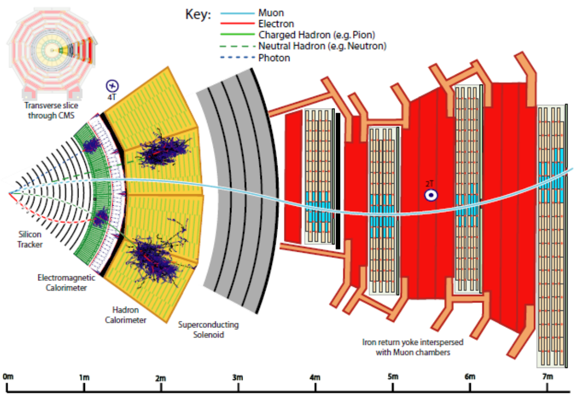

Figure 2.8. Particle identification.

CMS is capable of distinguishing between photons, electrons, muons, neutral hadrons (e. g. neutrons) and charged hadrons (e. g. pions, protons or kaons) as all of them lead to different signatures in the detector (CMS outreach, 2012);

- Photons, since they are not charged, do not produce any hits in the silicon tracker. They deposit all their energy in the electromagnetic calorimeter.
- Electrons produce hits in the silicon tracker and are stopped in the electromagnetic calorimeter.
- Muons also produce hits in the silicon tracker; however they only deposit very little energy in the calorimeters. Muons are the only particles causing a signal in the muon chambers.
- Charged Hadrons leaves hits in the tracking detector and little energy deposits in the electromagnetic calorimeter. They are stopped in the hadronic calorimeter.
- Neutral Hadrons will neither produce tracker hits nor electromagnetic calorimeter hits. They are fully stopped in the hadronic calorimeter.

2.6. Data Acquisition System

When running under design conditions the LHC will produce about 40 million bunch crossings every second in CMS. The data recorded by the detector after a bunch crossing is called an event. The average size of an event is about 1.0 MB. If all recorded events in CMS were stored this would correspond to a rate of several TB/s. Since this rate could never be archived, a sophisticated trigger system is required to reduce the event rate to a manageable amount of about 200 events per second. So, low energetic interactions occur and contaminate any real physics processes during the interaction. So, such events do not need to be stored and can be safely filtered out. The purpose of the trigger system is to decide quickly whether an event is worth storing or not. This decision is based on energy, multiplicity and combination of measured particles and missing transverse momentum. Various different triggers are exists for different purposes to eliminate bad events. There are twofold triggering systems for LHC (see Fig.2.9). The first step is called the Level 1 Trigger (L1) which reduces the rate to 100 kHz. The Level 1 Trigger is implemented in hardware for efficiency reasons. The event data is stored in hardware buffer while the trigger makes its decision. The buffer size limits the runtime of the trigger algorithm. At maximum, it has 3 ms to make a decision, including latency for data retrieval (CMS Collaboration, 2002). The Level 1 Trigger does not have access to the full detector data but only the calorimeters and the muon chambers. The second step is the High Level Trigger (HLT). It is implemented in software and runs on a computer farm based on available CPUs. The event rate is reduced from 100 kHz to about 100 Hz. This size is better to make analysis for short time (Armin Burgmeier, 2011).

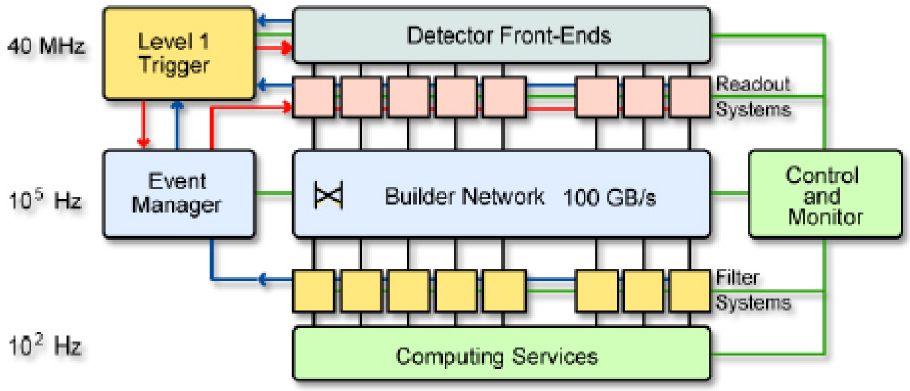

Figure 2.9. Data acquisition.

2.7. Event Labeling System

Every event recorded by CMS is uniquely identified by a three-tuple of run number, luminosity section and event number. The run number is a number which increases with LHC-time. For example, we need to make configuration, add or update trigger algorithms because of high luminosity. So, this requires starting a new run. Meanwhile, the luminosity section number starts at 1 and is incremented about every 23 s for each run. It is assumed that the instantaneous luminosity is constant during a luminosity section. Finally the event number uniquely identifies the event within a run and luminosity section (Armin Burgmeier, 2011).

2.8. The Simulation

2.8.1. The Full Simulation

The parton-parton hard scattering is generated using software tool such as PYTHIA (T. Sjostrand, S. Mrenna and P. Skands, 2006). The full simulation takes simulated particles and transports them through the detector. At each step, the interaction of particles with the detector material is computed by including the detector noise and the digitization steps applied by each sub-detector's electronics. Also, pile-up events can be randomly sampled from generated source files according to Poisson distribution (i.e. 20 events per bunch crossing), mixed with the primary event and setting of the Level-1 and high level triggers. Finally, the simulation has been tuned to experimental data but there are difficult challenges in modeling such highly stochastic phenomena as hadron. This whole process is known as full simulation. For the full simulation of the CMS experiment, CMS Software (CMSSW) framework were used. CMS uses the GEANT4 (Agostinelli, 2003) simulation toolkit and a number of similar packages to simulate beam transport and particular detector effects. The simulation covers all physical regions of the detector, and models the magnetic field's effect on the detector's response. The full simulation is estimated to contain some 1.3 million geometrical volumes and uses over 400 materials in GEANT4 database.

2.8.2. The Fast Simulation

The fast simulation takes the same generated particles as the full simulation and decays them in a similar way. It also provides an emulation of the Level-1 and high level triggers and pile-up. The fast simulation makes use of physics processes to gain a speed increase of 100-1000 per event over the full simulation.

Five different material effects should be taken into account in order to model accurately the propagation of the particles through the layers of the tracker. These effects are bremsstrahlung, photon conversions, multiple Coulomb scattering, energy loss through ionization and nuclear interactions. Apart from nuclear interaction all other effects were taken into account analytically. But nuclear interactions were simulated in a different manner. So, there is no analytical method to describe the effect of nuclear interaction. This effect is only found in the full simulation. In tracker, photon pair conversion from electrons in the fast (left) and full (right) simulations are given in the Fig. 2.10;

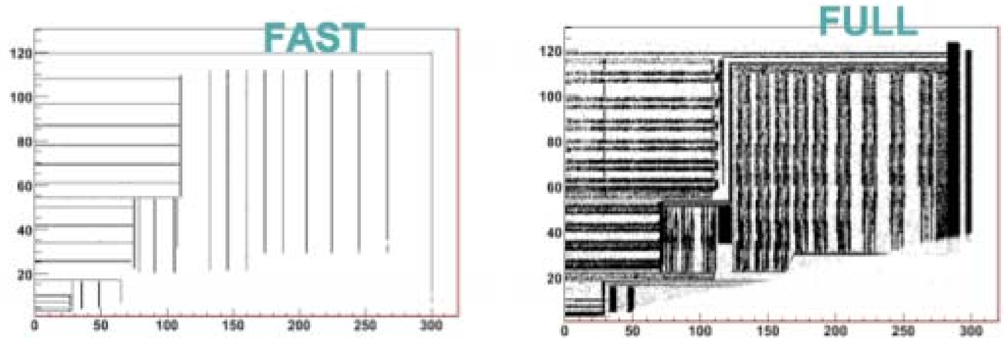

Figure 2.10. Comparison of fast and full simulation.

Our aim to mention about fast and full simulation is to explain how to reduce time taken for analysis, because full simulation takes too much time. But, we need to understand how many events we lose and how much shape of plots has changed during the signal production by the fast simulation. So, we produce some kinematics plots for fast and full simulation as is shown in figures below.

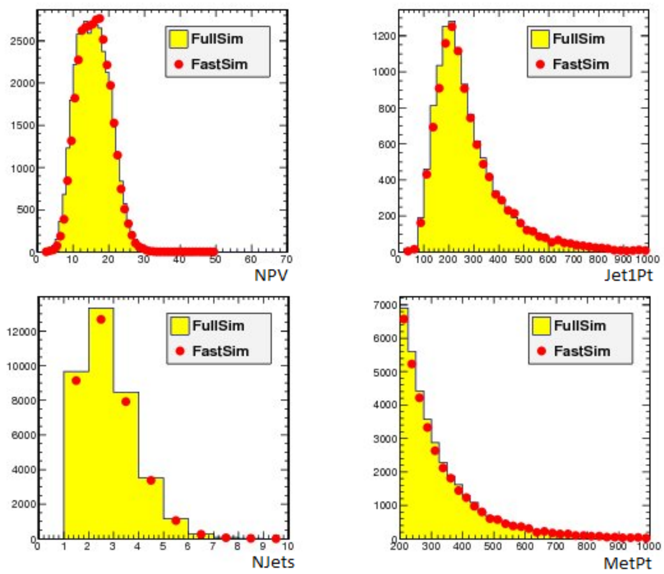

Figure 2.11. Comparison of fast and full simulation for monojets events.

These plots have been produced using Q_{11} (Maria Beltran, Dan Hooper, Edward W. Kolb, Zosia A. C. Krusberg and Tim M. P. Tait, 2010) model with the beam energy of 8 TeV and the dark matter mass of 100 GeV. According to Fig. 2.11, kinematic plots do not behave differently. Now, we need to check the difference between the fast and full simulation. Because this difference directly affects the limit value of cross section. In order to determine this difference, we need some basic plots which have information about parton (Generating) and reco (reconstruction) level.

- **Paton Level**

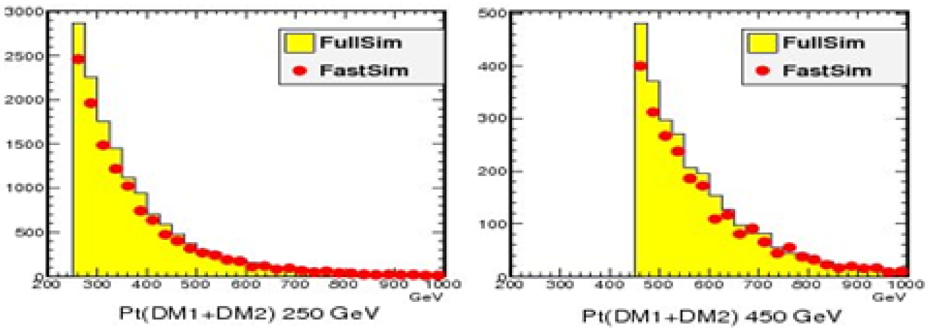

Figure 2.12. $\boldsymbol{P_T}$ distribution of $\boldsymbol{\chi\bar{\chi}}$ system.

There are two candidates for dark matter signal in generator level. They are known as χ and $\bar{\chi}$. So, we need to make a plot for χ and $\bar{\chi}$, separately or two-body system ($\chi\bar{\chi}$). The best way to observe behavior of generator level for fast and full simulation is to take a look at P_T distribution of the two-body system for different cut of $P_T(\vec{E}^T_{miss} + \overrightarrow{Mu}^T)$: $P_T(\vec{E}^T_{miss} + \overrightarrow{Mu}^T) > 250\ GeV$ and $P_T(\vec{E}^T_{miss} + \overrightarrow{Mu}^T) > 450\ GeV$ (shown in Fig. 2.12).

• **Reconstruction Level**

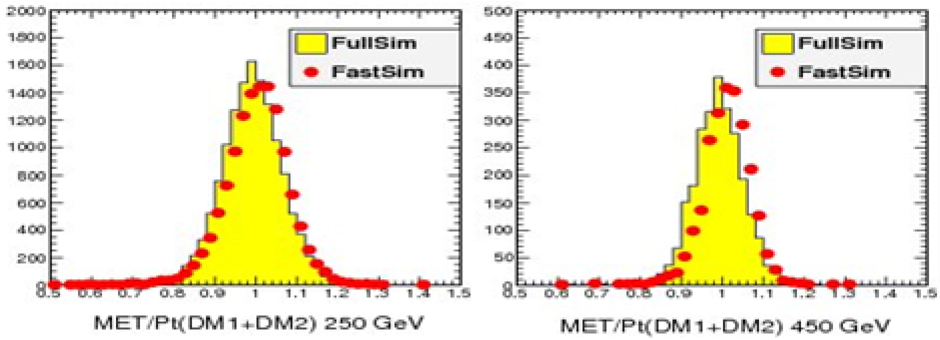

Figure 2.13. Distribution of missing energy and $\boldsymbol{P_T}$ ratio for $\chi\bar{\chi}$ system.

As known, two-body system in parton level does not appear as a particle in reco level, instead it can be observed as missing energy. Now, we need to check reconstruction efficiency for two-body system. E^T_{miss} distribution should be divided with P_T distribution of the two-body system. We expect mean value to be around 1 if efficiency of detector's reconstruction for dark matter signal is working well for different cut of $P_T(\vec{E}^T_{miss} + \overrightarrow{Mu}^T)$ (see above). It will be enough to look at plots in Fig. 2.13 for understanding of the difference between fast and full simulation. So, the mean value of each plot in Fig. 2.13 is given in Table 2.2.

Table 2.2. Mean value for fast and full simulation.

$\frac{P_T(Met)}{P_T(DM_1+DM_2)}$ **mean**	**Fast**	**Full**
P_T *(Met + Mu) > 250 GeV*	1.004	0.989
P_T *(Met + Mu) > 450 GeV*	1.013	0.989

According to Table 2.2, deviation of mean value between fast and full simulation is almost 2% and this deviation does not create a big effect for calculating the limit value of cross section. So, fast simulation can be used instead of full simulation for dark matter signal production. Also, as can be seen from Table 2.3 acceptances are not so different for fast and full simulation for various cut values.

Table 2.3. Acceptance for $\boldsymbol{Q_{11}}$ case.

Selection	Fast	Full
P_T *(Met + Mu) > 250 GeV*	12.52	11.09
P_T *(Met + Mu) > 300 GeV*	8.07	7.13
P_T *(Met + Mu) > 350 GeV*	5.30	4.74
P_T *(Met + Mu) > 400 GeV*	3.51	3.15
P_T *(Met + Mu) > 450 GeV*	2.33	2.14
P_T *(Met + Mu) > 500 GeV*	1.61	1.52
P_T *(Met + Mu) > 550 GeV*	1.09	1.07

2.9. Pileup Subtraction

Main challenge for the LHC is extraction of precise information from hadronic final states when large number of additional soft p-p collisions is present. These soft collisions are known as pileup and they occur simultaneously with any hard interaction in high luminosity runs. A technique which is based on jet area was suggested and it provides jet-by-jet corrections for pileup. In order to subtract pileup effect, it is needed to define a jet area as stated above. The jet area is different for each jet and depends on the details of its substructure. Given a suitable definition of jet area, the modification of a jet's transverse momentum is given as (T. Sjostrand, 2001);

$$p_t^{sub} = p_t - A\rho \qquad 2.7$$

where ρ is the level of diffuse noise which corresponds to the amount of transverse momentum and A is jet area (M. Cacciari, G. P. Salam and G. Soyez, 2008). This provides a correction to the jet's scalar transverse momentum.

Three conditions should be satisfied in order to pileup subtraction procedure is to be valid;

- The noise due to pileup should not dependent on rapidity and azimuthal angle.

- The number of jets coming from hard interaction should be much smaller than the number of jets from the pile up.
- The R which is the radius used for jet reconstruction should not be smaller than the typical distance between minimum bias particles. If this is not the case the extraction of ρ from the median will be biased by the large amount of empty area not associated with jets. Otherwise the median will be significantly biased by the hard jets.

2.10. Particle Flow Algorithm

The Particle Flow(PF) algorithm(James Ballin, 2010) attempts to reconstruct stable particles in the CMS detector(see Fig. 2.14). Stable particles mean photons, electrons, muons, charged pions, protons and neutrons. Firstly, every subdetector is considered individually and a clustering of calorimeter cells is performed. At this point, individual particles cannot be identified yet since for example a track in the silicon detector can belong to any charged particle. Therefore, in the next step geometric links between tracks, electromagnetic and hadronic calorimeter clusters are established. This combines information from all of these three systems.

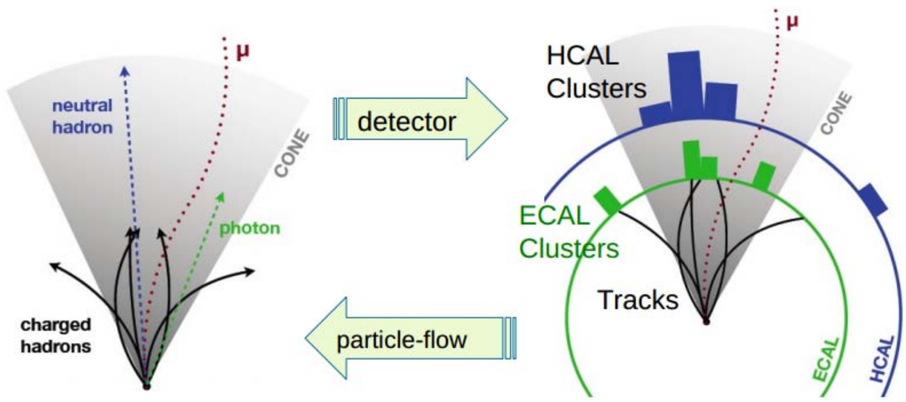

Figure 2.14. Particle-flow algorithm.

3. DARK MATTER

In astronomy and cosmology, Dark Matter(DM) is covering large part of the total mass in the universe. It is impossible to detect DM directly using telescopes. But if it exists its properties can be extracted from its effects on radiation and visible matter. According to literature, the total mass–energy of the universe consists of ordinary matter (4.9%), DM(26.8%) and dark energy(68.3%). Thus, DM and dark energy is estimated to constitute ~85% of the total matter-energy in the universe (V Trimble, 1987).

3.1. General Relativity

General Relativity (GR) is the geometric theory of gravitation submitted by Albert Einstein in 1916. According to GR, the curvature of space-time is directly connected with the energy-momentum tensor. This connection is specified by the Einstein's field equations.

3.1.1. Metric

The basic idea in GR is the metric.

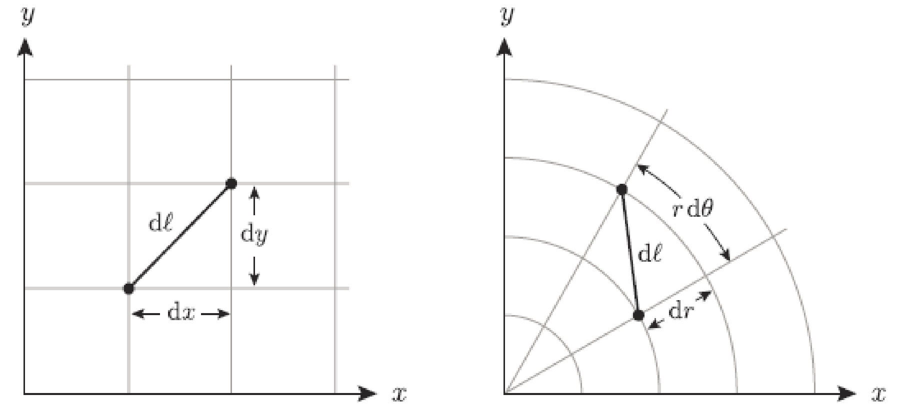

Figure 3.1. Left-hand part is defined as cartesian coordinate system and right hand side is known as polar coordinate system (Daniel Baumann, 2008).

The physical distance between two points is;

$$dl^2 = dx^2 + dy^2 \qquad 3.1$$

$$dl^2 = dr^2 + r^2 d\theta^2 \qquad 3.2$$

where dl^2 is an invariant variable. In relativity, it is encountered four-dimensional space-time metrics. These relate coordinate four-vectors dx^μ to the invariant ds;

$$ds^2 = \sum_{\mu,\nu=0}^{3} g_{\mu\nu}\ dx^\mu\ dx^\nu. \qquad 3.3$$

The $g_{\mu\nu}$ is a metric tensor. In Special Relativity (SR), the components of $g_{\mu\nu}$ are constants and given by;

$$g_{\mu\nu} = \begin{pmatrix} 1 & 0 & 0 & 0 \\ 0 & -1 & 0 & 0 \\ 0 & 0 & -1 & 0 \\ 0 & 0 & 0 & -1 \end{pmatrix} \text{ this gives rise to } ds^2 = dt^2 - dx^2. \qquad 3.4$$

This is known as Minkowski metric.

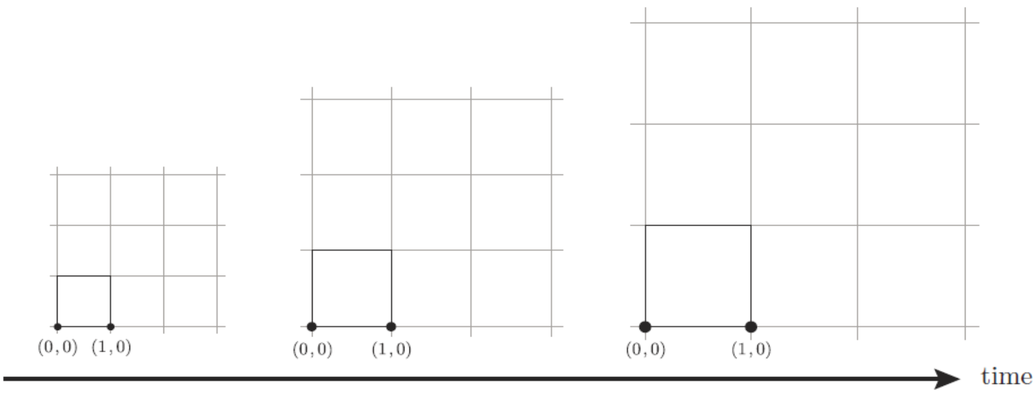

Figure 3.2. This figure illustrates expansion of the universe. While universe expands the comoving (coordinate) distance between points on grid will not change. The physical distance is given by the scale factor $\boldsymbol{a(t)}$ times the comoving distance. Hence, it is getting larger as time evolves (Daniel Baumann, 2008).

In an expanding space, there is a relation between comoving distance and physical distance. If the comoving distance between two points today is Δx_0, then the physical distance between the same two points at some earlier time t was $\Delta x_p = a(t)\Delta x_0$. The scale factor $a(t)$ is an increasing function. If space is approximately Euclidean, then the space-time metric is approximately Minkowski except that comoving distances must be multiplied by the scale factor. The resulting metric is called the Robertson-Walker metric.

$$g_{\mu\nu} = \begin{pmatrix} 1 & 0 & 0 & 0 \\ 0 & -a^2(t) & 0 & 0 \\ 0 & 0 & -a^2(t) & 0 \\ 0 & 0 & 0 & -a^2(t) \end{pmatrix} \text{ This leads to } ds^2 = dt^2 - a^2(t)d\boldsymbol{x}^2. \qquad 3.5$$

The evolution of the scale factor $a(t)$ depends on the density of the universe, $\rho(t)$.

3.1.2. Geodesic Equation

Figure 3.3. An arbitrary path in space-time, $x^\mu(\lambda)$, (Daniel Baumann, 2008).

When the motion of a test particle is considered in an arbitrary space-time $g_{\mu\nu}(t,x)$ the geodesic become a curve which can be considered as the length functional between a starting point A and a final point B;

$$\tau_{AB} = \int_A^B d\tau = \int_A^B \frac{d\tau}{d\lambda}\, d\lambda = \int_A^B \frac{1}{c}\left[g_{\beta\gamma}\frac{dx^\beta}{d\lambda}\frac{dx^\gamma}{d\lambda}\right]^{1/2} d\lambda \qquad 3.6$$

so the Lagrangian and action can be written as;

$$L(x^{\mu}, \dot{x}^{\mu}, \lambda) = \frac{1}{c}\left[g_{\beta\gamma}\frac{dx^{\beta}}{d\lambda}\frac{dx^{\gamma}}{d\lambda}\right]^{1/2} \tag{3.7}$$

$$A = \tau_{AB} = \int_{A}^{B} L(x^{\mu}, \dot{x}^{\mu}, \lambda)\, d\lambda. \tag{3.8}$$

Using Euler-Lagrange equations, equation of motion for curved space-time can be found (see Appendix 1.A) as;

$$\frac{d^2x^{\delta}}{d\tau^2} + \Gamma^{\delta}_{\beta\gamma}\frac{dx^{\beta}}{d\tau}\frac{dx^{\gamma}}{d\tau} = 0 \tag{3.9}$$

where $\Gamma^{\delta}_{\beta\gamma}$ is the Christoffel variable. This is the equation of motion for a particle moving on a geodesic in curved space-time. In particular, determination of how the energy of the particle changes as the universe expands is needed. In order to able to do that the Christoffel symbols associated with the Robertson-Walker (RW) metric is required. The only non-zero components are;

$$\Gamma^{0}_{ij} = a\dot{a}\delta_{ij} \quad \text{and} \quad \Gamma^{i}_{0j} = \frac{\dot{a}}{a}\delta_{ij} \tag{3.10}$$

where the dots denote derivatives with respect to time.

Consider application of geodesic equation to a massless particle. The energy-momentum 4-vector, $P^{\alpha} = (E, \vec{p})$ of the massless particle can be defined using parameter λ as (Daniel Baumann, 2008);

$$P^{\alpha} = \frac{dx^{\alpha}}{d\lambda}\,. \tag{3.11}$$

λ can be eliminated by noting that $\frac{d}{d\lambda} = \frac{dx^0}{d\lambda}\frac{d}{dx^0} = E\frac{d}{dt}$, and the 0-component of the geodesic equation can be written as;

$$E\frac{dE}{dt} = -a\dot{a}\delta_{ij}\, p^i p^j. \tag{3.12}$$

For a massless particle, the energy-momentum vector has zero magnitude;

$$g_{\mu\nu}P^{\mu}P^{\nu} = E^2 - \delta_{ij}a^2P^iP^j = 0$$
$$E^2 = \delta_{ij}a^2P^iP^j. \qquad 3.13$$

Substituting eq. 3.13 into eq. 3.12, it becomes

$$\frac{dE}{dt} + \frac{\dot{a}}{a}E = 0. \qquad 3.14$$

The energy of a massless particle decreases as the universe expands;

$$E \sim \frac{1}{a}. \qquad 3.15$$

These results show what it is known in basic physics: $E \sim \lambda^{-1}$ (where λ is the wavelength) and since $\lambda \sim a$ it is stretched with the expansion (Daniel Baumann, 2008).

3.1.3. Einstein Equation

It has been described before how a massless test particle moves in curved space-times. The motion in the curvature of space-time is determined by the local matter distribution. This means that;

$$\left\{\begin{matrix}\text{a measure of local} \\ \text{spacetime curvature}\end{matrix}\right\} = \left\{\begin{matrix}\text{a measure of local} \\ \text{stress} - \text{energy density}\end{matrix}\right\} \qquad 3.16$$

It has seen that the information about the curvature of space-time is contained in the metric. You can't get it easily from the Christoffel symbols ($\Gamma^{\mu}_{\alpha\beta}$) since they can be zero or not depending on the coordinate system. The information about curvature is contained in the Ricci tensor. This important object is given in terms of the Christoffel symbols by the formula;

$$R_{\mu\nu} = \partial_\alpha \Gamma^\alpha_{\mu\nu} - \partial_\nu \Gamma^\alpha_{\mu\alpha} + \Gamma^\alpha_{\alpha\beta}\,\Gamma^\beta_{\mu\nu} - \Gamma^\beta_{\mu\alpha}\,\Gamma^\alpha_{\nu\beta}. \qquad 3.17$$

If space is flat then all of the components of $R_{\mu\nu}$ vanish. This means that it is possible to find a global coordinate system in which all the components of the metric are constant everywhere. The trace of the Ricci tensor yields the Ricci scalar;

$$R = R^\mu_\mu = g^{\mu\nu} R_{\mu\nu}. \qquad 3.18$$

An important combination of Ricci tensor and Ricci scalar is the Einstein tensor;

$$G_{\boldsymbol{\mu\nu}} = R_{\mu\nu} - \frac{1}{2} R g_{\mu\nu}. \qquad 3.19$$

Einstein equation: the "equation of motion" for the metric is the famous Einstein equation;

$$G_{\mu\nu} = 8\pi G\, T_{\mu\nu} \qquad 3.20$$

where G is Newton's constant and $T_{\mu\nu}$ is the energy-momentum tensor or sometimes called the stress-energy tensor. The meaning of the different components of the stress-energy tensor is;

$$T_{\mu\nu} = \left(\begin{array}{c|c} T_{00} & T_{0i} \\ T_{i0} & T_{ij} \end{array}\right) = \left(\begin{array}{c|c} \text{Energy Density} & \text{Energy Flux} \\ \text{Momentum Density} & \text{Stress Tensor} \end{array}\right). \qquad 3.21$$

The symmetric tensor $T_{\mu\nu}$ includes all information about the energy and momentum of the matter fields, which act as a source for gravity. For expanding universe, Einstein's equation is the fundamental equation of cosmology. Let’s consider the

Robertson-Walker metric for the expanding universe. From the Christoffel symbols, the Ricci tensor is;

$$R_{00} = -3\frac{\ddot{a}}{a} \ ; \ \ R_{0i} = 0 \ ; \ R_{ij} = [2\dot{a}^2 + \ddot{a}a]\delta_{ij} \tag{3.22}$$

and the Ricci scalar is;

$$R = -6\left[\frac{\ddot{a}}{a} + \left(\frac{\dot{a}}{a}\right)^2\right]. \tag{3.23}$$

The 0-component of the Einstein equation therefore is;

$$\begin{aligned} G_{00} = R_{00} - \frac{1}{2}g_{00}R = 3\left(\frac{\dot{a}}{a}\right)^2 \\ = 8\pi G T_{00} = 8\pi G\rho \end{aligned} \tag{3.24}$$

where T_{00} is energy density for universe. Defining the Hubble parameter, $H = \partial_t \, ln\, a$, this becomes the Friedmann equation;

$$H^2 = \frac{8\pi G}{3}\rho. \tag{3.25}$$

This is the key evolution equation in cosmology (Daniel Baumann, 2008).

3.2. Thermodynamics in an Expanding Universe

The early universe was very hot and dense. (For example, when the age of the universe was 1 second, the mean free path of a photon was about the size of an atom). So, the interactions between particles were occurring very frequent. As long as the interaction rate Γ is bigger than the expansion rate H, these particles were in equilibrium. Otherwise, equilibrium does not appear in this universe. In other word, we can say like;

- $\Gamma > H$ Thermal Equilibrium
- $\Gamma < H$ Decouple time or Beyond Thermal Equilibrium

3.2.1. Thermodynamic Variables

The general relation between the wavelength λ and the box size L is;

Figure 3.4. One dimensional box.

The de Broglie wavelength in a given direction under the condition of quantization is defined as below;

$$\lambda = \frac{2L}{n} \qquad n = 1,2,3,4 \ldots. \qquad 3.26$$

where n is the quantum number of the state. In this case allowed values of the momentum of the particles are given by;

$$p = \frac{h}{\lambda} = \frac{h}{\left(\frac{2L}{n}\right)} = \frac{nh}{2L}. \qquad 3.27$$

The solutions can be added independently in three dimensions since the directions are orthogonal;

$$E = \frac{p^2}{2m} = \frac{h^2}{8mL^2}\left(n_x^2 + n_y^2 + n_z^2\right). \qquad 3.28$$

We should examine the behavior of E if we would like to extract the number of states in a given phase space volume. To do so energy is fixed to its maximum value E_{max}. Corresponding to E_{max} there is a maximal momentum p_{max} given by;

$$E = \frac{p_{max}^2}{2m}. \qquad 3.29$$

The maximum value of *n* is then;

$$n_{max} = \frac{2Lp_{max}}{h}. \qquad 3.30$$

The allowed states of the system correspond to any combination of n_x, n_y or $n_z$which satisfies;

$$n_x^2 + n_y^2 + n_z^2 \leq n_{max}^2 . \qquad 3.31$$

As a consequence, neither of n_x, n_y or n_z can be greater than n_{max}.

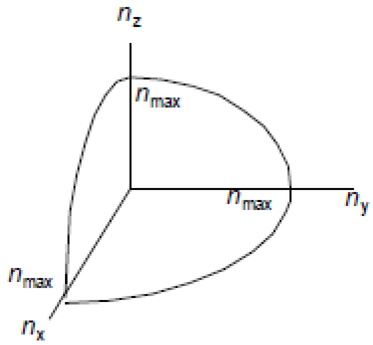

Figure 3.5. The volume of the octant.

Each of n_x, n_y or n_z in the box represents one unique state. Hence, N is the number of states whose energy is $E \leq E_{max}$ in the volume of the octant with positive side;

$$N(E \leq E_{max}) = \frac{1}{8}\frac{4\pi}{3}n_{max}^3 \qquad 3.32$$

where the factor of 1/8 arises from the volume of the octant. We switch from n to physical quantities as follows;

$$N = \frac{1}{8}\frac{4\pi}{3}n_{max}^3 = N(E \leq E_{max}) = \frac{1}{8}\frac{4\pi}{3}\left(\frac{2Lp_{max}}{h}\right)^3$$

$$N = \frac{L^3}{h^3}\left(\frac{4\pi}{3}p_{max}^3\right). \qquad 3.33$$

The first part on the right-hand side of the above equation is the volume of physical space while the second part is the volume of momentum space. So, the density of states must be given by;

$$density = \frac{N}{L^3\left(\frac{4\pi}{3}p_{max}^3\right)} = \frac{1}{h^3}. \qquad 3.34$$

This is the state density in phase space $\{x, p\}$ and it is equal to $\frac{1}{h^3}$. If the particle has g internal degrees of freedom (e.g. spin), then the density of states is given as;

$$\frac{g}{h^3} = \frac{g}{(2\pi)^3} \qquad 3.35$$

where in the second equality we used natural units with $\hbar = \frac{h}{2\pi}$ and $\hbar = 1$. If we multiply density of states with particle occupation number we get the particle density in phase space;

$$\frac{g}{(2\pi)^3} \times f(p) \qquad 3.36$$

where $p \equiv |p|$ and $f(p)$ is called the phase space distribution function. Since this equation is independent of the volume V, we can apply it for arbitrarily large systems. That means we can use it for large system. The particle density in ordinary space is found by integrating over momentum space (Daniel Baumann, 2008);

$$n = \frac{g}{(2\pi)^3} \int d^3p\, f(p). \qquad 3.37$$

During the early universe, the interaction energies between particles can be ignored. So, the particle energy is;

$$E(p) = \sqrt{m^2 + p^2}. \qquad 3.38$$

We use this to define the energy density;

$$\rho = \frac{g}{(2\pi)^3} \int d^3p\, f(p)\, E(p). \qquad 3.39$$

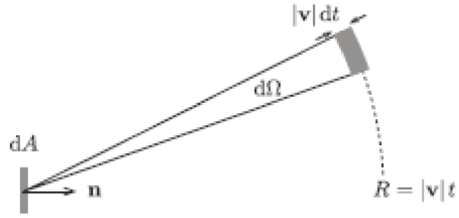

Figure 3.6. Pressure in a weakly interacting gas of particles (Daniel Baumann, 2008).

Consider a small area element of size dA with unit normal vector n. All particles with velocity $|v|$, striking this area element in the time interval between t and $t + dt$, were located at $t = 0$ in a spherical shell of radius $R = |v|t$ and width $|v|dt$. The total number of particles with energy $E(|v|)$ within a solid angle $d\Omega$ of this shell is equal to (Daniel Baumann, 2008);

$$dN = \frac{g}{(2\pi)^3} f(E) \times R^2 |v| dt d\Omega. \qquad 3.40$$

Not all particles in the shell reach the target, only those with velocities directed to the area element. Taking into account the isotropy of the velocity distribution, the total number of particles striking the area element $\boldsymbol{dA}\,.\boldsymbol{n}$ with velocity v is (Daniel Baumann, 2008);

$$dN_A = \frac{(\boldsymbol{v}.\boldsymbol{n})dA}{|v| 4\pi R^2} dN = \frac{g}{(2\pi)^3} f(E) \times \frac{(\boldsymbol{v}.\boldsymbol{n})}{|v| 4\pi} dA\, dt\, d\Omega. \qquad 3.41$$

If these particles are reflected elastically, each transfer momentum of $\mathbf{2}(\boldsymbol{p}.\boldsymbol{n})$ to the target. Therefore, the contribution of particles with velocity $|v|$ to the pressure is;

$$dP(v) = \int \frac{2(\boldsymbol{p}.\boldsymbol{n})\, dN_A}{dA\, dt} = \frac{g}{(2\pi)^3} f(E) \times \frac{p^2}{2\pi E} \int cos^2\theta\ sin\,\theta\ d\theta\, d\varphi$$
$$= \frac{g}{(2\pi)^3} \times \frac{p^2}{3E} f(E) \qquad 3.42$$

where we have used $|v| = |p|/E$ and integrated over the hemisphere. By integrating over energy $E(p)$, we obtain;

$$P = \frac{g}{(2\pi)^3} \int d^3p \; f(p) \frac{p^2}{3E} \,. \qquad 3.43$$

For species in kinetic equilibrium, the phase space occupancy is given by;

$$f(p) = \frac{1}{e^{(E(p)-\mu)/T} \pm 1} \qquad 3.44$$

where the + sign is for fermions and the − sign for bosons. The equilibrium distribution can be described by the temperature T and chemical potential μ. There is relation between temperature T and energy density ρ of the system. On the other hand also there is relation between chemical potential μ and the number density of particles in the system. As the universe expands, T and μ change in such a way that energy and particle number are conserved (Daniel Baumann, 2008).

3.2.1.1. Energy Density

Setting the chemical potential to zero, we get;

$$\rho = \frac{g}{2\pi^2} \int_0^\infty dp \; \frac{p^2 \sqrt{p^2+m^2}}{exp\left[\sqrt{p^2+m^2}/T\right] \pm 1} \,. \qquad 3.45$$

Defining $x = p/T$ and $\varepsilon = m/T$, this can be written as;

$$\rho = \frac{g}{2\pi^2} T^4 I_{\pm}(\epsilon) \qquad 3.46$$

where

$$I_{\pm}(\epsilon) = \int_0^{\infty} dx \frac{x^2\sqrt{x^2+\epsilon^2}}{exp[\sqrt{x^2+\epsilon^2}]\pm 1}. \qquad 3.47$$

In general, $I_{\pm}(\epsilon)$ has to be evaluated numerically. However, in the relativistic and nonrelativistic limits we can get analytic results (Daniel Baumann, 2008).

• **Relativistic Limit ($m \ll T$):** In the limit $\epsilon \to 0$, the integral reduces to;

$$I_{\pm}(0) = \int_0^{\infty} \frac{x^3}{e^x \pm 1} dx. \qquad 3.48$$

For bosons, this gives (see Appendix 1.B);

$$I_{-}(0) = \frac{\pi^4}{15}, \qquad 3.49$$

while for fermions, we find (see Appendix 1.C);

$$I_{+}(0) = \frac{7}{8} I_{-}(0). \qquad 3.50$$

Hence, we get;

$$\rho = \frac{\pi^2}{30} g T^4 \begin{pmatrix} 1 \ boson \\ \frac{7}{8} \ fermion \end{pmatrix}. \qquad 3.51$$

• **Non-Relativistic Limit ($m \gg T$):** In the absence of a chemical potential, very few particles are expected in the limit ($\epsilon \gg 1$). Consider again;

$$I_{\pm}(\epsilon) = \int_0^{\infty} dx \frac{x^2\sqrt{x^2+\epsilon^2}}{exp[\sqrt{x^2+\epsilon^2}]\pm 1} \qquad 3.52$$

$\epsilon \gg 1$ the exponential in the denominator dominates and increases rapidly if x is comparable to ϵ. The square root in the numerator can be replaced by ϵ and Taylor expanding the square root in the denominator to lowest order in x gives;

$$I_{\pm}(\epsilon) \approx \int_0^{\infty} dx \frac{x^2\epsilon}{exp\left[\epsilon\left(1+\left(\frac{x}{\epsilon}\right)^2\right)^{1/2}\right] \pm 1} = \epsilon e^{-\epsilon} \int_0^{\infty} dx\, x^2\, e^{-\frac{x^2}{2\epsilon}}. \qquad 3.53$$

The last integral is Gaussian and evaluates to $\sqrt{\pi/2}\,\epsilon^{3/2}$. Hence, we get;

$$I_{\pm}(\epsilon) = \sqrt{\frac{\pi}{2}}\epsilon^{5/2} e^{-\epsilon}. \qquad 3.54$$

Using eq. 3.49, we find

$$\frac{I_{\pm}(\epsilon)}{I_{-}(0)} = \frac{15}{\sqrt{2\pi^7}}\, \epsilon^{5/2} e^{-\epsilon} \ll 1. \qquad 3.55$$

This equation shows that heavy species ($m \gg T$) contribute much less to the energy density than light species ($m \ll T$), (Daniel Baumann, 2008).

3.2.1.2. The Particle Density

In the absence of a chemical potential, the particle density is written as;

$$n = \frac{g}{(2\pi)^3} \int d^3p\, \frac{1}{e^{\frac{E}{T}} \pm 1}. \qquad 3.56$$

Defining $x = p/T$ and $\varepsilon = m/T$, we can rewrite as;

$$n = \frac{g}{2\pi^2} T^3 Z_{\pm}(\varepsilon) \qquad 3.57$$

where

$$Z_{\pm}(\varepsilon) = \int \frac{x^2 dx}{e^{\sqrt{x^2+\varepsilon^2}} \pm 1}. \tag{3.58}$$

• **Relativistic Limit ($m \ll T$):** In the limit $\epsilon \to 0$, the integral reduces to

$$Z_{\pm}(\varepsilon) = \int \frac{x^2 dx}{e^{x} \pm 1}. \tag{3.59}$$

This integral has different solution for different statistical case like fermion or boson. In this case, our particle density is;

$$n = \frac{g}{\pi^2} T^3 \begin{pmatrix} 1 & \text{Boson} \\ \frac{3}{4} & \text{Fermion} \end{pmatrix}. \tag{3.60}$$

• **Non-Relativistic Limit ($m \gg T$):** In the absence of a chemical potential, we get;

$$Z_{\pm}(\varepsilon) = e^{-\varepsilon} \int x^2 e^{-\frac{x^2}{2\varepsilon}} \, dx. \tag{3.61}$$

Here, we can use Gaussian integral definition. In this case, we get;

$$n = \frac{g}{\sqrt{2\pi^3}} \varepsilon^{\frac{3}{2}} e^{-\varepsilon}. \tag{3.62}$$

When we compare relativistic with non-relativistic limit, we get;

$$\frac{n^{NG}}{n^{G}} \sim \varepsilon^{\frac{3}{2}} e^{-\varepsilon}. \tag{3.63}$$

According to this result, $n_{m \gg T} > n_{m \ll T}$. That means particle density in relativistic case is less than in non-relativistic case (Daniel Baumann, 2008).

3.2.1.3. Pressure

Setting the chemical potential to zero, we get;

$$P = \frac{g}{(2\pi)^3} \int \frac{p^2}{3E} \frac{1}{e^{\frac{E}{T}} \pm 1} d^3p = \frac{g}{2\pi^2} \int \frac{p^4 dp}{3E\left(e^{\frac{E}{T}} \pm 1\right)} \quad . \qquad 3.64$$

Defining $x = p/T$ and $\varepsilon = m/T$, we can rewrite as;

$$P = \frac{g}{2\pi^2} \frac{T^4}{3} K_{\pm} \qquad 3.65$$

where

$$K_{\pm} = \int \frac{x^4 dx}{\sqrt{x^2+\varepsilon^2}\left(e^{\sqrt{x^2+\varepsilon^2}} \pm 1\right)}. \qquad 3.66$$

• **Relativistic Limit ($m \ll T$):** In the limit $\epsilon \to 0$, the integral reduces to;

$$K_{\pm} = \int \frac{x^3\, dx}{e^x \pm 1}. \qquad 3.67$$

This result is equal to eq. 3.48. For this case, pressure can be written as;

$$P = \frac{\rho}{3}. \qquad 3.68$$

• **Non-Relativistic Limit ($m \gg T$):** if there is no chemical potential, we expect;

$$K_{\pm} = \varepsilon^{-1} e^{-\varepsilon} \int \left(1 - \frac{1}{2}\left(\frac{x}{\varepsilon}\right)^2\right) x^4 e^{-\frac{x^2}{2\varepsilon}} \quad .$$

In this case, pressure is proportional to;

$$P \approx e^{-\varepsilon}. \tag{3.69}$$

By comparing the relativistic $m \ll T$ and non-relativistic $m \gg T$ limits, it can be seen that the number density, energy density, and pressure of a system of particles exponentially decreases as the temperature gets much smaller than the mass of the particle. This is interpreted as the annihilation of particles and anti-particles. At higher energies this annihilations also occur, but they are balanced by particle-antiparticle pair production. At low temperatures, the thermal energy of particles are not sufficient enough for pair production (Daniel Baumann, 2008).

3.2.1.4. Effective Number of Degrees of Freedom

Imagine a system with a collection of different species, possibly in equilibrium at different temperatures T_i. The total energy density ρ_{tot} is the sum over all contributions;

$$\rho_{tot} = \sum_i \frac{g_i}{2\pi^2} T_i^4 \, I_{\pm}(\epsilon_i). \tag{3.70}$$

It is common to write this in terms of the temperature of the universe T for photon;

$$\rho_{tot} = \frac{g_*(T)}{2\pi^2} T^4 I_{-}(0) \tag{3.71}$$

where we have defined the effective number of degrees of freedom at the temperature T as;

$$g_*(T) = \sum_i g_i \left(\frac{T_i}{T}\right)^4 \frac{I_{\pm}(\epsilon_i)}{I_{-}(0)}. \tag{3.72}$$

Since the energy density of relativistic species is much greater than that of non-relativistic species, it can be written as;

$$g_*(T) = \sum_{i=bosons} g_i \left(\frac{T_i}{T}\right)^4 + \frac{7}{8}\sum_{i=fermion} g_i \left(\frac{T_i}{T}\right)^4 \quad . \qquad 3.73$$

The Friedman equation relates the Hubble expansion rate to the energy density of the universe. At early times, the universe is dominated by relativistic species and curvature is negligible (Daniel Baumann, 2008). Hence,

$$H^2 = \left(\frac{1}{a}\frac{da}{dt}\right)^2 = \frac{\rho_{tot}}{3M_{pl}^2} \cong \frac{\pi^2}{90} g_* \frac{T^4}{M_{pl}^2} \qquad 3.74$$

where

$$M_{pl} = (8\pi G)^{-1} = 2.4 \times 10^{18} GeV. \qquad 3.75$$

3.2.1.5. Entropy and Expansion History

In order to describe the evolution of the universe it is useful to track a conserved quantity. Entropy is a good candidate. The first law of thermodynamics for a system in equilibrium with negligible chemical potential is given by;

$$dE = TdS - PdV. \qquad 3.76$$

Using $E = \rho\, V$ and $S = s\, V$, we can write this as;

$$d\rho - Tds = (Ts - \rho - P)\frac{dV}{V}. \qquad 3.77$$

For example, one could consider a volume change at constant temperature, $dT = 0$, which implies that the coefficient of dV term must be zero. This relates the entropy density to the energy density and pressure;

$$s = \frac{\rho + P}{T}. \qquad 3.78$$

Using eq. 3.51 and eq. 3.68, the total entropy density for a collection of different particle species is;

$$s = \sum_i \frac{\rho_i + P_i}{T_i} = \frac{2\pi^2}{45} g_{*S}(T) T^3 \qquad 3.79$$

where we have defined the effective number of degrees of freedom in entropy;

$$g_{*S}(T) = \sum_{i=bosons} g_i \left(\frac{T_i}{T}\right)^3 + \frac{7}{8} \sum_{i=fermion} g_i \left(\frac{T_i}{T}\right)^3. \qquad 3.80$$

Under equilibrium conditions, one expect entropy to be conserved and the entropy density to scale as $s \propto a^{-3}$. To show this, consider the time derivative of sa^3;

$$\frac{T}{a^3} \frac{d(sa^3)}{dt} = \frac{T}{a^3} \frac{d}{dt} \left(\frac{\rho + P}{T} a^3 \right)$$
$$= \frac{d\rho}{dt} + 3\frac{\dot{a}}{a}(\rho + P) + \frac{dT}{dt}\left(\frac{dP}{dT} - \frac{\rho + P}{T}\right) \qquad 3.81$$

from the Appendix 1.D;

$$\frac{d\rho}{dt} + 3\frac{\dot{a}}{a}(\rho + P) = 0. \qquad 3.82$$

In this case, our results become;

$$\frac{T}{a^3} \frac{d(sa^3)}{dt} = \frac{dT}{dt}\left(\frac{dP}{dT} - \frac{\rho + P}{T}\right). \qquad 3.83$$

From this results, it can be found (see Appendix 1.E) that;

$$\frac{T}{a^3}\frac{d(sa^3)}{dt} = 0. \qquad 3.84$$

Hence, entropy is conserved for comoving system;

$$\frac{d(sa^3)}{dt} = 0 \qquad \rightarrow \qquad sa^3 = const. \qquad 3.85$$

In cosmology, this is a more useful conservation law than the conservation of energy. Entropy conservation provides the missing relationship between the temperature T and the scale factor a. Substituting eq. 3.79 into eq. 3.84, we have;

$$\frac{2\pi^2}{45} g_{*S}(T)T^3a^3 = const = s_e \qquad 3.86$$

where s_e is the extrapolated entropy density of the universe if there were no new sources of entropy. As long as $g_{*S} = const$, the temperature therefore decreases as the inverse of the scale factor;

$$T(a) = s_e^{1/3}\left(\frac{45}{2\pi^2 g_{*S}}\right)^{1/3} a^{-1}. \qquad 3.87$$

When this results is substituted to eq. 3.25 then;

$$H^2 = \left(\frac{1}{a}\frac{da}{dt}\right)^2 = \frac{\rho_{tot}}{3M_{pl}^2} \cong \frac{\pi^2}{90} g_* \frac{T^4}{M_{pl}^2} \qquad 3.88$$

found. By integrating, we get;

$$a(t) = \frac{s_e^{1/3}}{M_{pl}}\left(\frac{45}{2\pi^2 g_{*S}}\right)^{1/12}\left(\frac{g_*}{g_{*S}}\right)^{1/4}\left(\frac{t}{t_{pl}}\right)^{1/2}. \qquad 3.89$$

This is the usual result for a radiation dominated universe, $a \propto t^{1/2}$, except that there is changes in g_* all the time. Finally, from eq. 3.89, we obtain the temperature as a function of time (Daniel Baumann, 2008);

$$\frac{T}{M_{pl}} = \left(\frac{45}{2\pi^2 g_*}\right)^{1/4} \left(\frac{t_{pl}}{t}\right)^{1/2} \qquad \text{or} \qquad \frac{T}{1MeV} \cong 1.5\, g_*^{-1/4} \left(\frac{1}{t}\right)^{1/2}. \qquad 3.90$$

3.3. Thermal Equilibrium

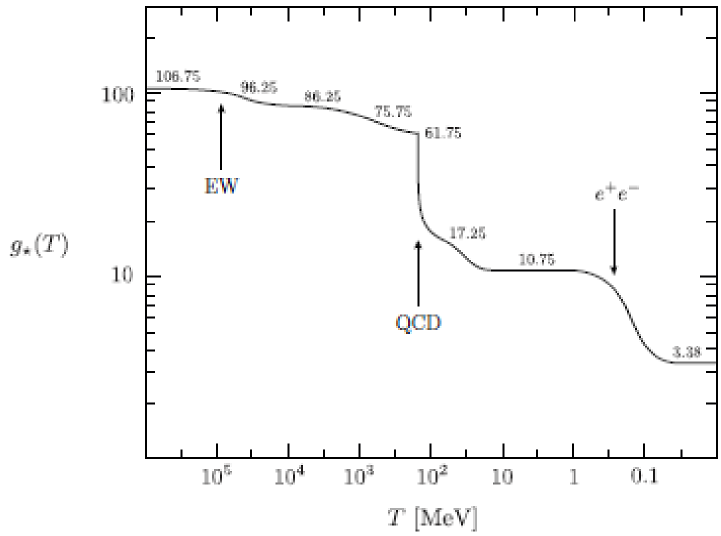

Figure 3.7. Evolution of relativistic degrees of freedom assuming the standard model particle (Daniel Baumann, 2008).

In Fig. 3.7, the history of the universe is shown between 100 GeV and 0.5 MeV. We assume that the primordial plasma initially consists of all the particles of the Standard Model (SM). Now, we can define their internal degrees of freedom.

Quarks	t	173 GeV	$\bar{t}$	spin= $\frac{1}{2}$	$g = 2 \cdot 2 \cdot 3 = 12$
	b	4 GeV	$\bar{b}$	3 colors	
	c	1 GeV	$\bar{c}$		
	s	100 MeV	$\bar{s}$		
	d	5 MeV	$\bar{d}$		
	u	2 MeV	$\bar{u}$		
Gluons		0		spin= 1	$g = 8 \cdot 2 = 16$
Leptons	τ^-	1777 MeV	τ^+	spin= $\frac{1}{2}$	$g = 2 \cdot 2 = 4$
	μ^-	106 MeV	μ^+		
	e^-	511 keV	e^+		
	ν_τ	< 2 eV	$\bar{\nu}_\tau$	spin= $\frac{1}{2}$	$g = 2 \cdot 1 = 2$
	ν_μ	< 2 eV	$\bar{\nu}_\mu$		
	ν_e	< 2 eV	$\bar{\nu}_e$		
Gauge bosons	W^+	80 GeV		spin= 1	$g = 3$
	W^+	80 GeV			
	Z^0	91 GeV			
	γ	0			$g = 2$
Higgs boson	H^0	125 GeV		spin= 0	$g = 1$

Figure 3.8. Particle Content of the SM (Daniel Baumann, 2008).

For $T > 100$ GeV, all known particles are relativistic. Adding up their internal degrees of freedom (see Fig. 3.8), we get;

$$g_b = 28 \qquad \text{photon}(2), \text{W}^{\pm} \text{ and } \text{Z}^0(3 * 3),\ \text{gluons}(8 * 2), \text{and Higgs } (1)$$

$$g_f = 90 \qquad \text{quarks}(6 * 12),\ \text{leptons}(3 * 4),\ \text{neutrinos}(3 * 2)$$

and hence;

$$g_* = g_b + \frac{7}{8} g_f = 106.75. \tag{3.91}$$

As the temperature drops, various particle species become non-relativistic and annihilate. In order to estimate g_* at a temperature T, we simply add up the contributions from all relativistic degrees of freedom and discard the rest (Daniel Baumann, 2008).

3.3.1. Electroweak Symmetry Breaking

Table 3.1. History of the effective number of relativistic species (Daniel Baumann, 2008).

T	Event	g_*
$\sim 100\ GeV$	EW Transition	106.75
$< 170\ GeV$	Top Annihilation	96.25
$< 80\ GeV$	$W^{\pm}$, Z^0, H^0	86.25
$< 4\ GeV$	Bottom	75.75
$< 1\ GeV$	Charm, τ	61.75
$\sim 150\ MeV$	QCD Transition	17.25
$< 100\ MeV$	π, μ	10.75
$\sim 1\ GeV$	Neutrino Decoupling	10.74

At sufficiently high energies, all particles of the SM are massless. After the electroweak (EW) phase transition ($T \sim 100\ GeV$ in Table 3.1), particles receive their masses through the Higgs mechanism. The top quark therefore begins to annihilate efficiently after the EW transition. In fact, the transition from relativistic to non-relativistic behavior is not complete until $T \sim \frac{1}{6}$ m. For the top quark this corresponds to $T \sim 30\ GeV$ at which point the effective number of relativistic species is reduced to $g_* = 106.75 - \frac{7}{8} \times 12 = 96.25$. The Higgs boson and the gauge bosons $W^{\pm}, Z^0$ annihilate consequently. At $T \sim 10\ GeV$, we have $g_* = 96.26 - (1 + 3 * 3) = 86.25$. Next, the bottom quark annihilates $g_* = 75.75$ followed by the charm quarks and the tau lepton $g_* = 61.75$ (Daniel Baumann, 2008).

3.3.2. QCD Phase Transition

Before the strange quarks had time to annihilate, something else happens: matter undergoes the QCD phase transition. This takes place at $T \sim 150\ MeV$ (see Table 3.1). While quarks are asymptotically free at high energies, interactions between quarks and gluons become important below 150 MeV. It becomes energetically favorable for asymptotically free quarks and gluons to form bound states and the quark-gluon plasma becomes hadron plasma. Three-quark systems called baryons and quark-antiquark pairs known as mesons are formed from bound states of quarks and gluons. The lightest baryons and the lightest mesons are the nucleons (the proton and the neutron) and the pions ($\pi^{\pm}$, π^{0}), respectively (Daniel Baumann, 2008).

3.3.3. Neutrino Decoupling

Neutrinos feel the weak interaction. When the particle energies are at the level of the masses of the W and Z bosons, the weak interaction was not so weak and neutrinos couple to other species. But as the temperature drops, the weak interaction becomes rapidly weaker and weaker. A particle species falls out of chemical equilibrium when the interactions become too weak to maintain their coupling to the other species as the universe expands. This happens when the interaction rate Γ becomes smaller than the expansion rate, $\Gamma < H$. The interaction rate can be written as;

$$\Gamma = n < \sigma v > \quad 3.92$$

where n is the number density of the particles, σ is the interaction cross section, v is the particle velocity and the brackets represents an average over the phase space. If the cross section is independent of velocity, we can take it out of the average, and if the particles are relativistic, we can approximate $v = 1$. In that case, we have simply $\Gamma = n\,\sigma$. For the weak interaction for neutrinos, the cross section is given by;

$$\sigma \sim G_F^2\, T^2 \quad 3.93$$

where $G_F \approx 1.17 \times 10^{-5}\ GeV^{-2}$ is the Fermi constant. The interaction rate is then;

$$\Gamma \sim G_F^2\, T^5 \ . \quad 3.94$$

Using the Friedman equation, $H \sim \frac{T^2}{M_{pl}}$, we have;

$$\frac{\Gamma}{H} \sim G_F^2\, M_{pl} T^3 \sim \left(\frac{T}{MeV}\right)^3 \quad . \tag{3.95}$$

We conclude that neutrinos decouple when temperature is around $T \sim 1\,MeV$ (see Table 3.1), after that temperature they move freely without interacting (Daniel Baumann, 2008).

3.4. Beyond Thermal Equilibrium

Beyond thermal equilibrium there was times in which interaction rate was smaller than expansion rate ($\Gamma < H$). So, all of thermodynamic variables at thermal equilibrium are not valid for this case. This is problem for physics to understand its history. To solve this problem, Boltzmann has suggested an equation which defines out of thermal equilibrium. This equation is known as Boltzmann Equation (Daniel Baumann, 2008).

3.4.1. Boltzmann Equation

In order to study non-equilibrium processes, we need to follow the evolution of the distribution function $f_i(x^\mu, P^\mu)$ for a particle species i in the presence of interactions. Boltzmann equation is applied for this system. This equation is given by;

$$\hat{L}\, f_i = \hat{C}_i\big[\{f_j\}\big] \tag{3.96}$$

where $\hat{L}$ is the Liouville operator and $\hat{C}_i\big[\{f_j\}\big]$is a collision operator that represents the effect of interactions. The Liouville operator is just equal to the total time derivative in the non-relativistic limit. This relation is given by;

$$\hat{L}_{NR} = \frac{d}{dt} = \frac{\partial}{\partial t} + \frac{\partial x}{\partial t}\frac{\partial}{\partial x} + \frac{dp}{dt}\frac{\partial}{\partial p} \quad . \qquad 3.97$$

For a particle species of mass m subject to a force, this can be written as;

$$\hat{L}_{NR} = \partial t + \boldsymbol{v}.\boldsymbol{\partial x} + \frac{\boldsymbol{F}}{\boldsymbol{m}}.\boldsymbol{\partial_v} \quad . \qquad 3.98$$

The relativistic generalization of the Liouville operator is the total derivative with respect to an affine parameter λ;

$$\hat{L}_{NR} = \frac{d}{d\lambda} = \frac{\partial x^{\mu}}{\partial \lambda}\frac{\partial}{\partial x^{\mu}} + \frac{dP^{\mu}}{d\lambda}\frac{\partial}{\partial P^{\mu}} \quad . \qquad 3.99$$

The second term defines the change in the distribution function from changes in momentum as particles move along geodesics. As it was discussed before, the following normalization can be chosen for the affine parameter;

$$P^{\mu} = \frac{dx^{\mu}}{d\lambda}. \qquad 3.100$$

So that the geodesic equation becomes;

$$\frac{dP^{\mu}}{d\lambda} = -\Gamma^{\mu}_{\alpha\beta}P^{\alpha}P^{\beta}. \qquad 3.101$$

When eq. 3.101 and eq. 3.100 are substituted to eq. 3.99, it can be found that;

$$\hat{L}_{GR} = P^{\mu}\frac{\partial}{\partial x^{\mu}} - \Gamma^{\mu}_{\alpha\beta}P^{\alpha}P^{\beta}\frac{\partial}{\partial P^{\mu}} \, . \qquad 3.102$$

In Flat Robertson-Walker (FRW), the phase space density is homogeneous and isotropic, $f_i(E,t)$, and so the action of the Liouville operator becomes;

$$\hat{L}f_i = E\frac{\partial f_i}{\partial t} - \frac{\dot{a}}{a}p^2\frac{\partial f_i}{\partial E} \ . \qquad 3.103$$

We obtain the integrated Boltzmann equation (see Appendix 1.F) as;

$$\frac{1}{a^3}\frac{d(n_i a^3)}{dt} = 2\int \hat{C}_i \frac{d^3 p_i}{(2\pi)^3 2E_i} \, . \qquad 3.104$$

In the absence of interactions, the r.h.s. of eq. 3.104 vanishes and the l.h.s. simply expresses the fact that the number of particles in a fixed physical volume is conserved.

Let us consider the following process;

$$1 + 2 \ \rightarrow 3 + 4. \qquad 3.105$$

Particle 1 can interact with particle 2 to produce particles 3 and 4, or the inverse process can produce 1 and 2. The Boltzmann equation simply formalizes this statement. For the process in eq. 3.105, the Boltzmann equation is;

$$\frac{1}{a^3}\frac{d(n_1 a^3)}{dt} = \int_{p_1,p_2}^{p_3,p_4} (2\pi)^4\, \delta^4(P_1 + P_2 - P_3 - P_4) \times |M|^2 \times (f_3 f_4 - f_1 f_2). \qquad 3.106$$

To understand the structure of the interaction terms, let us read the r.h.s. of eq. 3.106;

- First, consider the factor $(f_3 f_4 - f_1 f_2)$. This simply expresses the fact that the rate of producing species 1 is proportional to the occupation numbers of species 3 and 4, while the rate of eliminating of them is proportional to the occupation numbers of 1 and 2.
- Moving along, we encounter the amplitude M. This is determined from the fundamental physics in question.
- Next, we see a delta function. This simply enforces energy and momentum conservation for the process.

Equation 3.106 would be very hard to solve. Fortunately, in many practical applications in cosmology further simplifications are justified;

- First, although the system is not in chemical equilibrium, to a good approximation it remains in kinetic equilibrium. That is, scattering takes place so rapidly that the distribution functions of the various species still take on the Bose-Einstein or Fermi-Dirac form.
- We will be in regime $T \ll E - \mu$. In this limit, the distribution function (eq. 3.44) reduces to the Maxwell-Boltzmann distribution;

$$f(E) \approx e^{\frac{\mu}{T}} e^{-\frac{E}{T}}. \qquad 3.107$$

Using this gives us;

$$f_3 f_4 - f_1 f_2 \approx e^{-(E_1+E_2)/T} \left(e^{\frac{(\mu_3+\mu_4)}{T}} - e^{\frac{(\mu_1+\mu_2)}{T}} \right) \qquad 3.108$$

where we used energy conservation ($E_1 + E_2 = E_3 + E_4$). The number densities themselves were used as the time-dependent function to be solved for, instead of μ. The number density of species *i* as a function of μ_i is given by;

$$n_i = e^{\frac{\mu_i}{T}} n_i^{(0)} \qquad 3.109$$

where $n_i^{(0)}$ is the equilibrium number density;

$$n_i^{(0)} = \frac{g_i}{(2\pi)^3} \int d^3p \; e^{-\frac{E(p)}{T}}. \qquad 3.110$$

In this case, eq. 3.108 becomes;

$$f_3 f_4 - f_1 f_2 \approx e^{-(E_1+E_2)/T} \left(\frac{n_3}{n_3^{(0)}} \frac{n_4}{n_4^{(0)}} - \frac{n_1}{n_1^{(0)}} \frac{n_2}{n_2^{(0)}} \right). \tag{3.111}$$

With these approximations, the Boltzmann equation simplifies to;

$$\frac{1}{a^3} \frac{d(n_1 a^3)}{dt} = n_1^{(0)} n_2^{(0)} < \sigma v > \left(\frac{n_3}{n_3^{(0)}} \frac{n_4}{n_4^{(0)}} - \frac{n_1}{n_1^{(0)}} \frac{n_2}{n_2^{(0)}} \right) \tag{3.112}$$

where we have defined the thermally averaged annihilation cross section;

$$< \sigma v > \equiv \frac{1}{n_1^{(0)} n_2^{(0)}} \int \int \int \int (2\pi)^4 \delta^4 (P_1 + P_2 - P_3 - P_4) \times |M|^2. \tag{3.113}$$

The equality can be maintained when the term in the parenthesis in eq. 3.113 is cancelled when reaction rates are large. Then it can be found that;

$$\frac{n_3}{n_3^{(0)}} \frac{n_4}{n_4^{(0)}} = \frac{n_1}{n_1^{(0)}} \frac{n_2}{n_2^{(0)}}. \tag{3.114}$$

This is called as chemical equilibrium equation (Daniel Baumann, 2008).

3.4.2. DM Relics

In order to understand the world around us, it is therefore crucial to understand the deviations from equilibrium that led to the freeze-out of massive particles. These particles are called **W**eakly **I**nteracting **M**assive **P**article**s** (WIMPs). For concreteness, we will focus on the hypothesis that WIMPs were in close contact with the rest of the cosmic plasma in the hot and dense early universe. As the temperature dropped below their mass they experienced freeze-out. Our purpose is to solve the Boltzmann equation for such a particle. Imagine that two heavy particles χ and $\bar{\chi}$ can annihilate to produce two light (essentially massless) particles l and $\bar{l}$;

$$\chi + \bar{\chi} \leftrightarrow l + \bar{l}. \qquad 3.115$$

For this interaction, Boltzmann equation can be written as;

$$\frac{1}{a^3}\frac{d(n_\chi a^3)}{dt} = n_\chi^{(0)} n_{\bar{\chi}}^{(0)} < \sigma v > \left(\frac{n_l}{n_l^{(0)}}\frac{n_{\bar{l}}}{n_{\bar{l}}^{(0)}} - \frac{n_\chi}{n_\chi^{(0)}}\frac{n_{\bar{\chi}}}{n_{\bar{\chi}}^{(0)}}\right)$$

$$\frac{1}{a^3}\frac{d(n_\chi a^3)}{dt} = < \sigma v > \left(n_\chi^{(0)} n_{\bar{\chi}}^{(0)} \frac{n_l}{n_l^{(0)}}\frac{n_{\bar{l}}}{n_{\bar{l}}^{(0)}} - n_\chi n_{\bar{\chi}}\right). \qquad 3.116$$

The light particles are tightly coupled to the cosmic plasma, so that throughout they maintain their equilibrium densities, $n_l = n_l^{(0)}$ because chemical potential is zero. The Boltzmann equation (eq. 3.116) for the evolution of the WIMP density n_χ then becomes;

$$\frac{1}{a^3}\frac{d(n_\chi a^3)}{dt} = < \sigma v > \left(\left(n_\chi^{(0)}\right)^2 - n_\chi^2\right). \qquad 3.117$$

Since the temperature of the universe scales as $T \sim a^{-1}$, it is useful to define $Y = \frac{n_\chi}{T^3}$. In this case, Boltzmann equation is;

$$\frac{dY}{dt} = T^3 < \sigma v > (Y_0^2 - Y^2) \qquad 3.118$$

where $Y_0 = \frac{n_\chi^{(0)}}{T^3}$. Since most of the action will take place when the temperature is at the order of the particle mass ($T \sim m$), it is convenient to define a new measure of time;

$$x = \frac{m}{T} \ . \qquad 3.119$$

From Appendix 1.G and eq. 3.118, we can write;

$$\frac{dY}{dx}\frac{dx}{dt} = \frac{m^3}{x^3} < \sigma v > (Y_0^2 - Y^2)$$

$$\frac{dY}{dx} = \frac{<\sigma v> m^3}{H}\frac{1}{x^3}(Y_0^2 - Y^2)$$

$$\frac{dY}{dx} H\, x = \frac{m^3}{x^3} < \sigma v > (Y_0^2 - Y^2)$$

$$\frac{dY}{dx}\frac{H_1}{x} = \frac{m^3}{x^3} < \sigma v > (Y_0^2 - Y^2)$$

$$\frac{dY}{dx} = \frac{\lambda}{x^2}(Y_0^2 - Y^2) \qquad 3.120$$

where $\lambda = \frac{m^3 <\sigma v>}{H_1}$ and $H = \frac{H_1}{x^2}$ .This equation is so-called Riccati equation (Daniel Baumann, 2008). Even for constant λ, there are no analytic solutions of eq. 3.120. In Fig. 3.19, we see results for different λs.

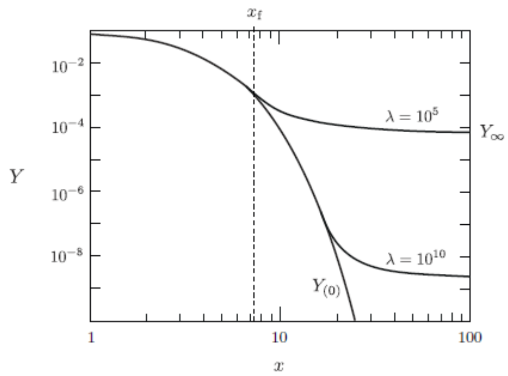

Figure 3.9. Abundance of DM particles as the temperature drops below to its mass (Daniel Baumann, 2008).

As expected, at very high temperatures $x < 1$, we have $Y \approx Y_{(0)} \cong 1$. However, at low temperatures $x \gg 1$, the equilibrium abundance becomes exponentially suppressed $Y_{(0)} \sim e^{-x}$. The abundance of WIMPs at equilibrium cannot be maintained because of this suppression and χ particles become rarer. The final relic abundance ($Y_\infty = Y(x = \infty)$) determines the freeze-out density of DM. Let us estimate its magnitude as a function of λ. Well after freeze-out, Y will be much larger than $Y_{(0)}$ .Thus at late times, we can drop $Y_{(0)}$ from the Boltzmann equation;

$$\frac{dY}{dx} \cong -\frac{\lambda Y^2}{x^2} \quad 3.121$$

where $x \gg 1$. We can integrate this equation to get;

$$\frac{1}{Y_\infty} - \frac{1}{Y_f} = \frac{\lambda}{x_f} \quad 3.122$$

where x_f is the time of freeze-out and $Y_f \equiv Y(x_f)$. Typically, $Y_f \gg Y_\infty$, so a simple analytic approximation is;

$$Y_\infty \cong \frac{x_f}{\lambda}. \quad 3.123$$

This still depends on the unknown freeze-out time (or temperature) x_f. As we can see from Fig. 3.9, a magnitude estimate of x_f is ~ 10. More importantly, eq. 3.123 predicts that the freeze-out abundance Y_∞ decreases as the interaction rate λ increases (Daniel Baumann, 2008).

It just remains to relate the freeze-out abundance of DM relics to the DM density today Ω_χ. After freeze-out, the DM density dilutes as a^{-3}. Hence, the energy density today is (see Appendix 1.H);

$$\rho_{\chi,0} \equiv \rho_\chi(a_0) = mn_\chi(a_1)\left(\frac{a_1}{a_0}\right)^3 \quad 3.124$$

where a_1 corresponds to a time sufficiently late, so that $Y(a_1) \approx Y_\infty$. Using $n_\chi(a_1) = Y_\infty T_1^3$ (definition is $Y = \frac{n_\chi}{T^3}$), we can write eq. 3.124 as;

$$\rho_{\chi,0} = mY_\infty T_0^3 \left(\frac{a_1 T_1}{a_0 T_0}\right)^3 \quad 3.125$$

where

$$\left(\frac{a_1 T_1}{a_0 T_0}\right)^3 = \frac{g_{*S}(T_0)}{g_{*S}(T_1)} \cong \frac{1}{30} \, . \qquad 3.126$$

Hence, we get ;

$$\rho_{\chi,0} = \frac{m Y_\infty T_0^3}{30} \, . \qquad 3.127$$

Inserting the freeze-out abundance eq. 3.123 equation and λ, we find;

$$\rho_{\chi,0} = \frac{x_f}{30}\frac{m T_0^3}{\lambda} = \frac{x_f}{30}\frac{H}{m^2}\frac{T_0^3}{<\sigma v>} \qquad 3.128$$

where

$$H = \frac{\pi}{3}\left(\frac{g_*}{100}\right)^{1/2}\frac{m^2}{M_{pl}} \, . \qquad 3.129$$

Dividing eq. 3.128 by the critical density $\rho_{crit,0} = 3H_0^2 M_{pl}^2$, we get;

$$\Omega_\chi = \frac{\rho_{\chi,0}}{\rho_{crit,0}} = \left(\frac{x_f}{10}\right)\left(\frac{g_*}{100}\right)^{1/2}\frac{1}{3H_0^2}\frac{T_0^3}{M_{pl}^3}\frac{1}{<\sigma v>} \, . \qquad 3.130$$

Using $T_0 = 2.7K \cong 10^{-31} M_{pl}$ and $H_0 \cong 10^{-28} h \; cm^{-1}$, this is;

$$\Omega_\chi h^2 = 0.3\left(\frac{x_f}{10}\right)\left(\frac{g_*}{100}\right)^{1/2}\frac{10^{-37} cm^2}{<\sigma v>}. \qquad 3.131$$

This density parameter does not depend on the mass of the WIMP, instead depends on the value of the annihilation cross section. The main result is that the smaller the annihilation cross section, the greater the relic abundance (Daniel Baumann, 2008).

3.5. Detections

The effective Lagrangian for the interaction between WIMP and nucleon is given by (T. Falk, A. Ferstl, and K. A. Olive, 2000);

$$L = \lambda_N \bar{\psi}_\chi \gamma_\mu \psi_\chi \bar{\psi}_N \gamma_\mu \psi_N + K_1 \bar{\psi}_\chi \psi_\chi \bar{\psi}_N \gamma_5 \psi_N + K_2 \bar{\psi}_\chi \gamma_5 \psi_\chi \bar{\psi}_N \psi_N + K_3 \bar{\psi}_\chi \gamma_5 \psi_\chi \bar{\psi}_N \gamma_5 \psi_N + K_4 \bar{\psi}_\chi \gamma_\mu \gamma_5 \psi_\chi \bar{\psi}_N \gamma_\mu \psi_N + \varepsilon_N \bar{\psi}_\chi \gamma_\mu \gamma_5 \psi_\chi \bar{\psi}_N \gamma_\mu \gamma_5 \psi_N \quad 3.132$$

where γ_μ and γ_5 are Dirac matrices, ψ_χ is dark matter wave function, ψ_N is nuclei wave function. The operators K_i are suppressed in the limit of small momentum transfer by a factors of $\frac{q^2}{M_N^2}$ or $\frac{q^2}{M_\chi^2}$ where $q^2 = -Q^2$. So, this factor is so small that we can ignore the contribution coming from K_i. Therefore, only operator λ_N for vector or spin independent (SI) interaction and ε_N for axial-vector or spin dependent(SD) interaction survives.

3.5.1. Direct Detection

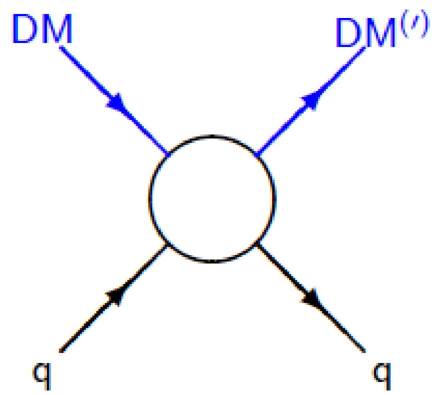

Figure 3.10. Direct detection.

As DM particle passes through the Earth, it may collide elastically with nuclei which are made of parton like quark and gluon. After the collision, DM particle will have a different momentum, because some momentum has been transferred into parton in nuclei. So, this experiment can be interpreted as a scattering event between DM and SM particles.

The experiments of a direct detection whose names are XENON100, COUPP, CoGeNT and CDMSII have a simple idea. According to their idea, detector has a very sensitive device and can detect very small motions and interactions of the atoms within it. So, if candidates of dark matter (WIMP's or χ) are everywhere in the universe, some of them should travel through the earth. Therefore, they should be observed in the direct detection apparatus at any times. Now, it is important to determine what kind of interaction (like elastic or inelastic) happens between WIMP and target nucleus (A). To establish this interaction, we need to check how much momentum should be transferred into the target nucleus. If the velocity of DM particle ($M_\chi = 100\ GeV$) is around $v \approx 0.001c$ (this is almost at the same order with the orbital velocity of the Sun) and mass of the target nucleus $M_A = 100\ GeV$, the maximum momentum transfer is;

$$\sqrt{-Q^2} = 2v\frac{M_\chi M_A}{M_\chi + M_A} \approx 100\ MeV. \qquad 3.133$$

The momentum transfer is very small as compared to the masses of the WIMP or nuclei. So, the interaction between WIMP and nuclei will be elastic. Thus, all WIMP-nucleon elastic cross sections can be calculated with zero momentum transfer. The effective Lagrangian from eq. 3.132 thus reduces to;

$$L^{SI} = \lambda_N \bar{\psi}_\chi \gamma_\mu \psi_\chi \bar{\psi}_N \gamma_\mu \psi_N \qquad 3.134$$

where $N = p, n$. The cross section for a WIMP scattering at rest from a point-like nucleus is;

$$\sigma^{SI} = \frac{4\mu_\chi^2}{\pi}\left(\lambda_p Z + \lambda_n (A - Z)\right)^2 \qquad 3.135$$

where μ_χ is the WIMP-nucleus reduced mass ($\mu_\chi = \frac{M_\chi M_A}{M_\chi + M_A}$), Z is the nucleus charge, A is the total number of nucleons. Also, λ_p and λ_n are proton-dark matter and neutron-dark matter coupling constants respectively. As you can notice, cross section depend on A^2(G. Belanger, F. Boudjema, A. Pukhov, A. Semenov, 2008).

3.5.2. Indirect Detection

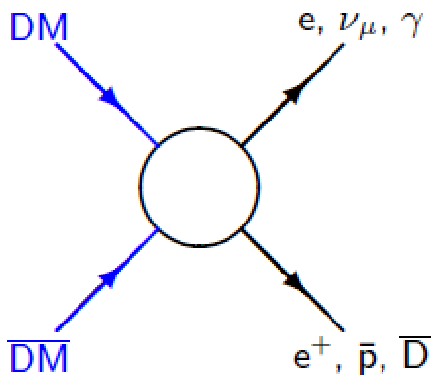

Figure 3.11. Indirect detection.

WIMPs which are gravitationally captured in Earth or Sun could annihilate. This annihilation produces energetic neutrinos. Some of them can be muon neutrinos. These neutrinos produce muons which can be detected by muon experiments like IceCUBE. So, this type of experiments are thought as annihilation experiments.

One of the potential signals for detection of DM could be the WIMP-WIMP annihilation. This annihilation can be observed with technique of indirect detection. The experiment using this technique is SIMPLE, CDMSII, IceCUBE, COUPP and Super-K. The product of this annihilation includes gamma-rays (the galactic center), neutrinos (the Sun or Earth) and antimatter. So, the effective Lagrangian for these experiments is given by;

$$L^{SD} = \varepsilon_N \bar{\psi}_\chi \gamma_\mu \gamma_5 \psi_\chi \bar{\psi}_N \gamma_\mu \gamma_5 \psi_N \tag{3.136}$$

where $N = p, n$. The cross section for a point-like nucleus at rest is given by;

$$\sigma^{SD} = \frac{16\mu_\chi^2}{\pi}\frac{J_A+1}{J_A}\left(\varepsilon_p S_p^A + \varepsilon_n S_n^A\right)^2 \qquad 3.137$$

where J_A is the angular momentum of a nucleus with A nucleons, S_p^A is expectation value of the spin for proton, S_n^A is expectation value of the spin for neutron, ε_p is coupling of proton-dark matter interaction, ε_n is coupling of neutron-dark matter interaction. Indirect cross section depends on the angular momentum of whole nucleus (G. Jungman, M. Kamionkowski, and K. Griest, 1996).

3.6. Collider Detection

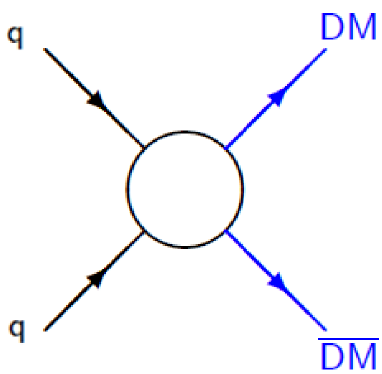

Figure 3.12. Collider detection.

SM particles could annihilate in order to produce DM in the collider experiment. This annihilation produces DM candidates which do not appear in detector.

One candidate of DM is χ which is a Dirac Fermion. In colliders, DM production is mediated by a massive mediator which couples to χ and standard-model quarks. Since the mass of mediator is too big the interaction can be considered as a contact interaction. The other important feature of mediator or particle is its width value since it is related to particle life time (Patrick J. Fox, Roni Harnik, Joachim Kopp, and Yuhsin Tsai, 2011). The relationship between total width and life time is given by;

– 3.138

where is life time, is total width for particle.

The measurement of the mass of an unstable particle gives a distribution which is called a Lorentzian or a Breit-Wigner. Let's try to understand relation between this distribution and particle width. Consider a particle whose mass is and Breit-Wigner distribution for this particle is presented in Fig 3.13.

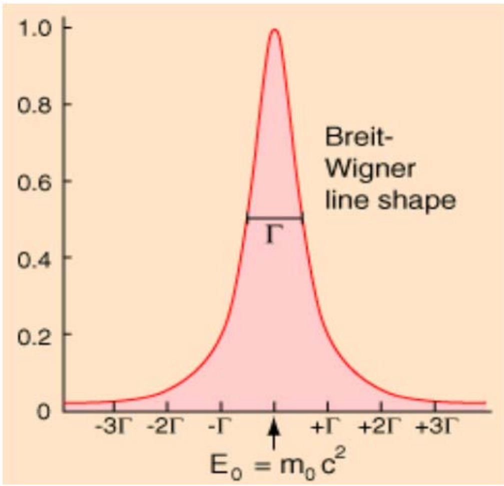

Figure 3.13. Breit-Wigner distribution.

As it can be seen from Fig. 3.13, the biggest possibility corresponds to nearly center of the plot. If width value of a particle is Γ, the particle behaves like on-shell between – and –. If the particle is on-shell, then it is recorded by MadGraph. But, if it is out of this range it behaves like off-shell and is not recorded by MadGraph.

The mediator width could be changed with the mediator mass. When the mediator mass is too heavy its width could be ignored, but when it is not too heavy its width could not be ignored. In fact, this reason is coming from the structure of propagator.

The Feynman diagram of dark matter-quark interaction is shown below (Patrick J. Fox, Roni Harnik, Joachim Kopp, and Yuhsin Tsai, 2011).

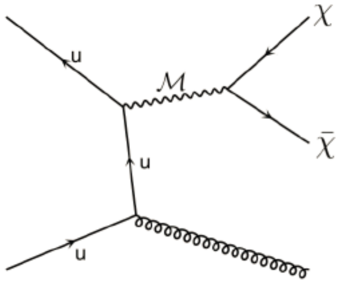

Figure 3.14. Feynman diagram for collider detection.

In Fig. 3.14, the cross section which is related to propagator is defined as following (Patrick J. Fox, Roni Harnik, Joachim Kopp, and Yuhsin Tsai, 2011);

$$\sigma \approx \frac{g_q^2 g_\chi^2}{(q^2 - M^2)^2 + \Gamma^2} E^2 \quad 3.139$$

where E is the center-of-mass energy. M, Γ and q are respectively mass, width and four-momentum of mediator, respectively. g_q is coupling constants between mediator and SM quarks and g_χ is coupling constants between mediator and dark matter. In this Feynman diagram, momentum transfer is very small since mediator mass is too big. So, q can be ignored. In this case, the cross section can be rewritten as below (Patrick J. Fox, Roni Harnik, Joachim Kopp, and Yuhsin Tsai, 2011);

$$\sigma \approx \frac{g_q^2 g_\chi^2}{M^4 + \Gamma^2} E^2. \quad 3.140$$

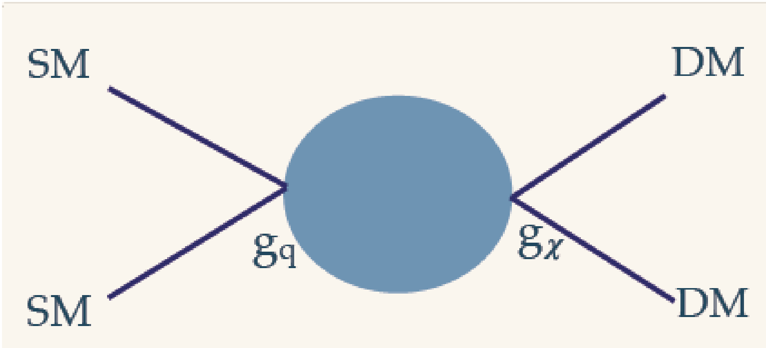

Figure 3.15. Contact interactions for collider detection.

In our study Z' is chosen as a mediator. It satisfies to create the dark matter particles which are in the mass range of 1 GeV and 1000 GeV in models of vector, axial-vector and scalar which are denoted as V, AV and D11, respectively. Events of those models are produced by Q_V, Q_{AV} and Q_{11} generator with MadGraph (Patrick J. Fox, Roni Harnik, Joachim Kopp, and Yuhsin Tsai, 2011);

$$Q_V = \frac{(\bar{\chi}\gamma^\mu\chi)(\bar{q}\gamma^\mu q)}{\Lambda^2} \quad \text{Vector Case} \quad 3.141$$

$$Q_{AV} = \frac{(\bar{\chi}\gamma^\mu\gamma^5\chi)(\bar{q}\gamma^\mu\gamma^5 q)}{\Lambda^2} \quad \text{Axial Vector Case} \quad 3.142$$

$$Q_{11} = \frac{1}{4\Lambda^3}\bar{\chi}\chi\alpha_s\left(G^a_{\mu v}\right)^2 \quad \text{Scalar Case} \quad 3.143$$

where Λ is cutoff scale, $\Lambda = \frac{M}{\sqrt{g_\chi\, g_q}}$. γ^μ and γ^5 are Dirac matrix. α_s is coupling constant of strong interaction. $G^a_{\mu v}$ is the gluon field strength tensor.

In AV and V models, mediator should be heavy because the effective field theory is also valid at collider scales. In other words, momentum transfer is too small because mediator is very much heavy. In this system, the effective field Lagrangian (L) is given in eq. 3.144 which consists three parts: first part is SM Lagrangian (L_{SM}), next one is kinetic terms of DM (χ) and last term is interactions between χ and SM quarks *q = u, d, s, c, b, t* (Maria Beltran, Dan Hooper, Edward W. Kolb, Zosia A. C. Krusberg and Tim M. P. Tait, 2010);

$$L = L_{SM} + i\bar{\chi}\gamma^\mu\partial_\mu\chi - M_\chi\bar{\chi}\chi + \sum_q \frac{G_{qij}}{\sqrt{2}}\sum_{i,j}\left[\bar{\chi}\Gamma_i^\chi\chi\right]\left[\bar{q}\Gamma_q^j q\right] \quad 3.144$$

where Γ is tensor of interaction, G_{qij} is interaction term between WIMPs and leptons in mass dimension. M_χ is dark matter mass.

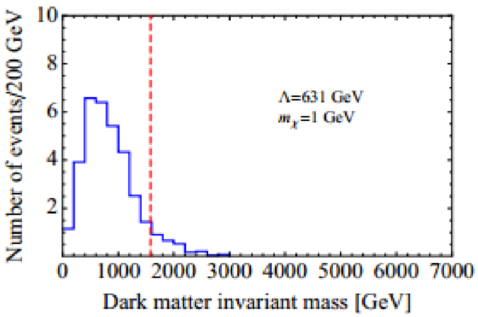

(a) $m_\chi = 1$ GeV

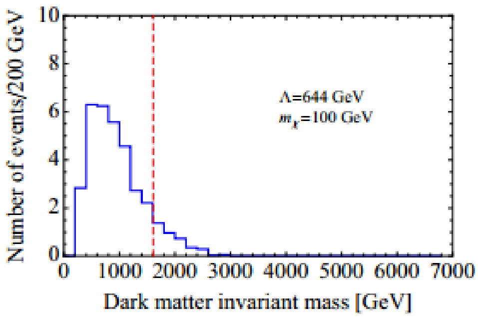

(b) $m_\chi = 100$ GeV

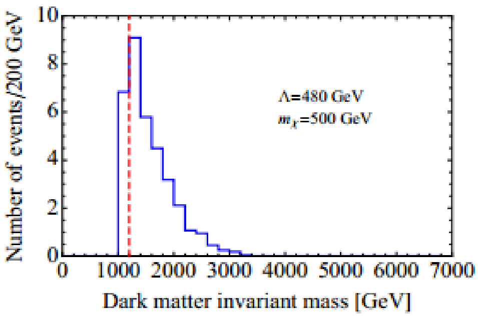

(c) $m_\chi = 500$ GeV

Figure 3.16. Unitarity for collider detection. The red line in the figure is for definition of limit point for invariant mass.

The unitarity of $q\bar{q}$ scattering with center of mass energy of $\hat{s}$ sets a limit on the production of DM. In particular, this limit is determined by the cutoff scale (Λ) over the invariant mass of $\chi\bar{\chi}$ system (Patrick J. Fox, Roni Harnik, Reinard Primulando and Chiu-Tien Yu, 2012);

$$M_{\chi\bar{\chi}} < \frac{\Lambda}{0.4} \qquad 3.145$$

where $M_{\chi\bar{\chi}}$ is invariant mass of $\chi\bar{\chi}$. This equation states that allowed $M_{\chi\bar{\chi}}$ is smaller than the cutoff scale. As it can be seen from Fig. 3.16, the fractions of events in forbidden area are 8%, 11% and 80%, respectively. So, forbidden area is going up if DM mass is increasing. Because of this reason, limit result is going bad at high DM mass.

3.7. Signal Production

3.7.1. Event Generator

"Event generators are software libraries that generate simulated high-energy particle physics events. At the matrix element level, these include the development of general purpose event generators such as MadGraph/MadEvent, CompHEP/CalcHEP, SHERPA and WHIZARD" (J. Alwall, P. Demin, S. de Visscher, R. Frederix, M. Herquet, F. Maltoni, T. Plehn, D. L. Rainwater, Tim Stelzer, 2007). In our analysis, we used the MadGraph event generator. Now, we will try to explain how to work in MadGraph/MadEvent. The structure of the MadGraph/MadEvent package used is shown in Fig. 3.17.

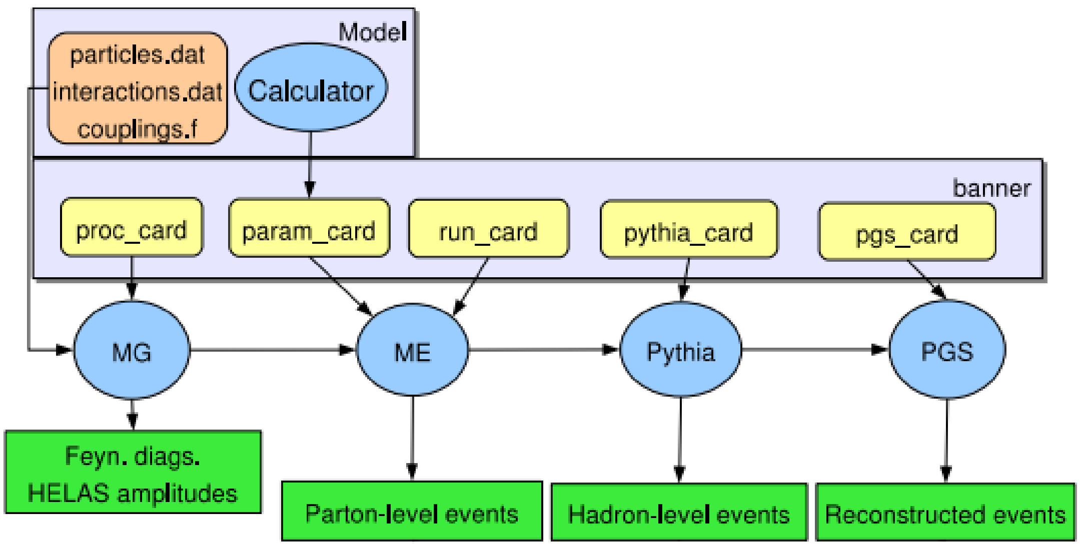

Figure 3.17. Event generation progress.

"There are four steps for event production: code creation, parton-level event, hadron-level event and reconstructed object generation. The first step is the creation of the code specific to the process that the user requests. This can be done directly by filling the process card, proc_card.dat. The second step is the parameter card, param_card.dat, which contains the numerical values of the necessary parameters for a specific model. The parameter card has a format compliant with the Les Houches

Accord, and is dependent on the physics model. The third card is the run card, run_card.dat, where all the information regarding the event generation (number of events requested, random seed), the collision (energy, beam type, pdf's, scales) and the acceptance of the detector ($P_T(min)$, $\eta(max)$) is passed. Once the cards are completed, the event generation can start. The resulting data file will have the unweighted events in the Les Houches format. The fourth step is to pass the parton-level to Pythia by specifying in the pythia_card.dat the desired options. Finally, the events at hadron level are passed to GEANT4, whose parameters are set in the pgs_card.dat. This simulates how events will appear in detector" (J. Alwall, P. Demin, S. de Visscher, R. Frederix, M. Herquet, F. Maltoni, T. Plehn, D. L. Rainwater, Tim Stelzer, 2007).

3.8. Parton Level Analysis

Parton level events are generated with MadGraph in the LHE file format. They contain number of particles, type of particle, particle momentum etc. for each event generated. Parton level analysis is based upon such files.

3.8.1. Effect of Mediator Width in Cross Section

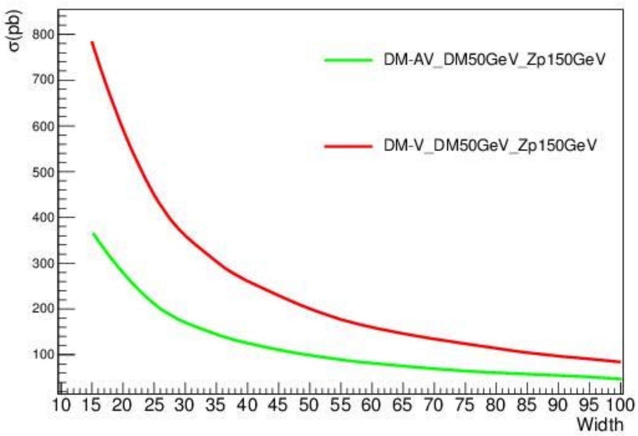

Figure 3.18. The cross section as a function of mediator width

In the analysis, DM particle mass is 50 GeV for AV and V models. Also, mediator mass of Z′ is 150 GeV. Its width value has been changed from 10 GeV to 100 GeV for both models. So, a different cross section has been gotten for each width value of Z′. According to the Fig. 3.18, cross section is inversely proportional to width value of Z′ for both models.

3.8.2. Effect of Mediator Mass in Cross Section

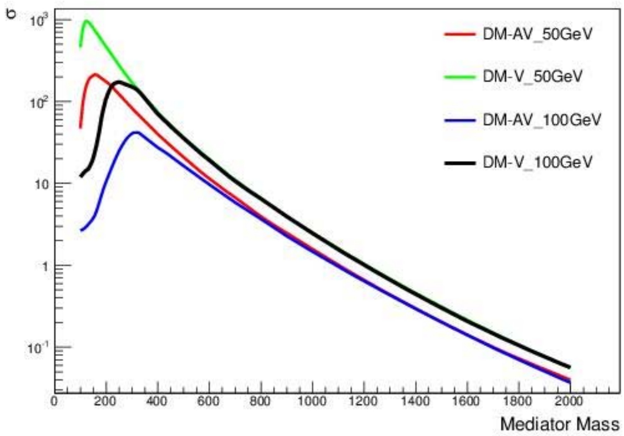

Figure 3.19. The cross section as a function of mediator mass.

Relationship between mediator mass and cross section is shown in Fig. 3.19. It could be seen that two different DM masses are chosen with 50 GeV and 100 GeV for AV and V models and also mediator mass is varied from 100 GeV to 2000 GeV. There are two main results can be driven from Fig. 3.19. One is about low mediator mass and the other is for high mediator mass. In low mediator which is called as off-shell mass, cross section is increasing exponential sharply for 50 GeV DM mass and smoothly for 100 GeV DM mass. On the other hand, in high mediator which is called as on-shell mass, cross section is decreasing as exponentially for both cases.

3.8.3. Parton Distribution Function

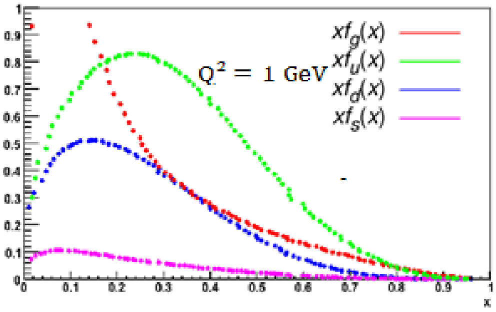

Figure 3.20. PDF distribution.

A parton distribution function(PDF) is defined as a probability density for finding a particle with a certain longitudinal momentum fraction x Bjorken Scale (BS) at momentum transfer $Q^2 = 1$ GeV (Adam Szabelski, 2012). According to Fig 3.20, u, d and s quark appear at low BS ($0 < x < 0.15$). This means that in proton-proton collisions at the LHC, interactions will most probably happen between u, d and s quarks. If the BS increases, also gluons begin to be involved in the interaction.

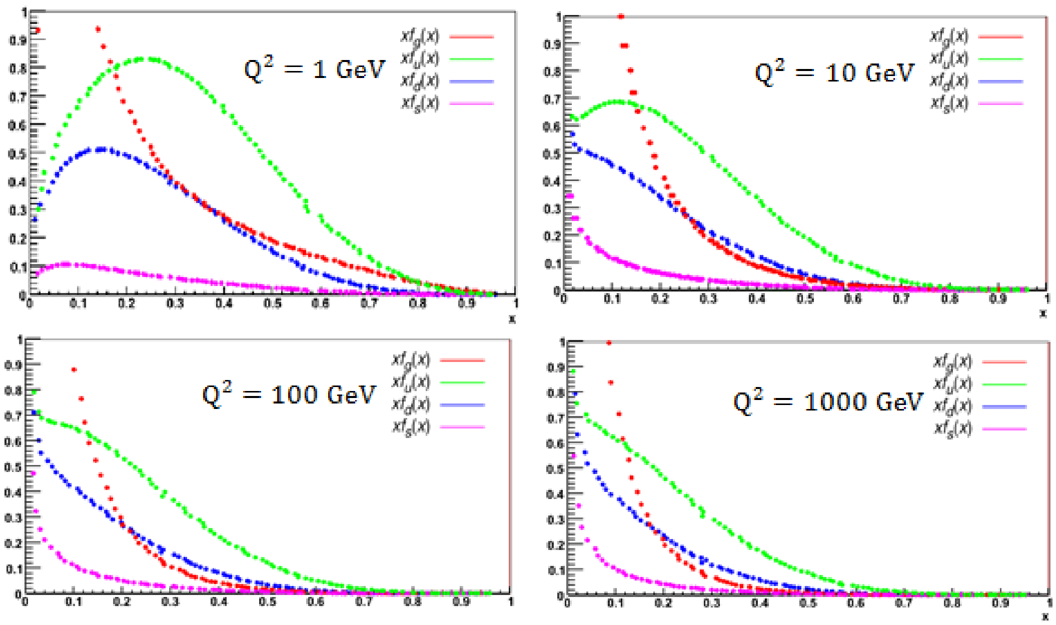

Figure 3.21. PDF Distribution according to different momentum transfers.

According to Fig. 3.21, when momentum transfer is increased from 1 GeV to 1000 GeV with ten-time steps, parton like quarks and gluon in a hadron behaves same in agreement with shape of the PDF distribution.

3.8.4. Unitarity Effect on Event Production

The unitarity is mentioned as theoretical respect in Section 3.6. In this section, its experimental aspect will be considered.

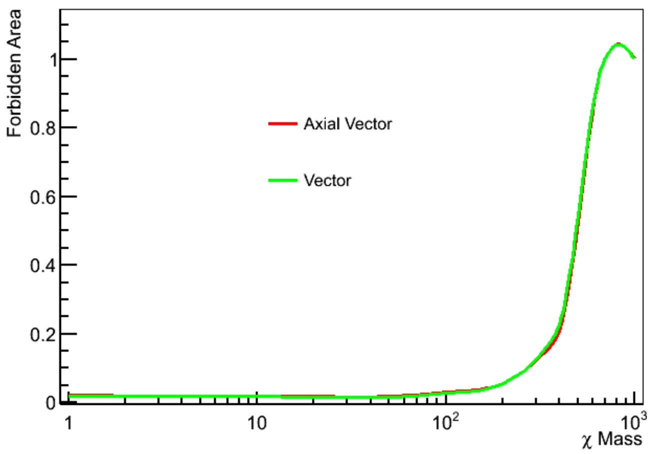

Figure 3.22. Unitarity effect.

According to Fig. 3.22, until DM mass reach 300 GeV, less of the produced events go to the forbidden area. But when DM mass goes to higher than that value, most of the produced events go to the forbidden area for both of the AV and V models. Since most of produced events go to forbidden area, the cross section limits starts to be meaningless. So, analysis will not be comfortable for this zone.

3.8.5. Kinematic of Parton on Event Production

The MadGraph are used in order to produce generator level events. The p-p collision creates a jet (due to quarks or gluons) and a mediator. This mediator decays to χ and $\bar{\chi}$ for AV and V models. This event is known as monojet event since χ and $\bar{\chi}$ will not be detected in detector. So, feature of this jet can give us an opportunity to measure some features of DM. Mediator mass and Jet P_t are selected as 40 TeV and 80 GeV respectively and the DM mass is varied between 1 GeV and 1000 GeV for part of this analysis. The kinematics of jet, like P_t, η and φ are shown in Fig. 3.23. As it can be seen from the Fig. 3.23, signal sample events behave as expected in terms of P_t, η and φ of Jet.

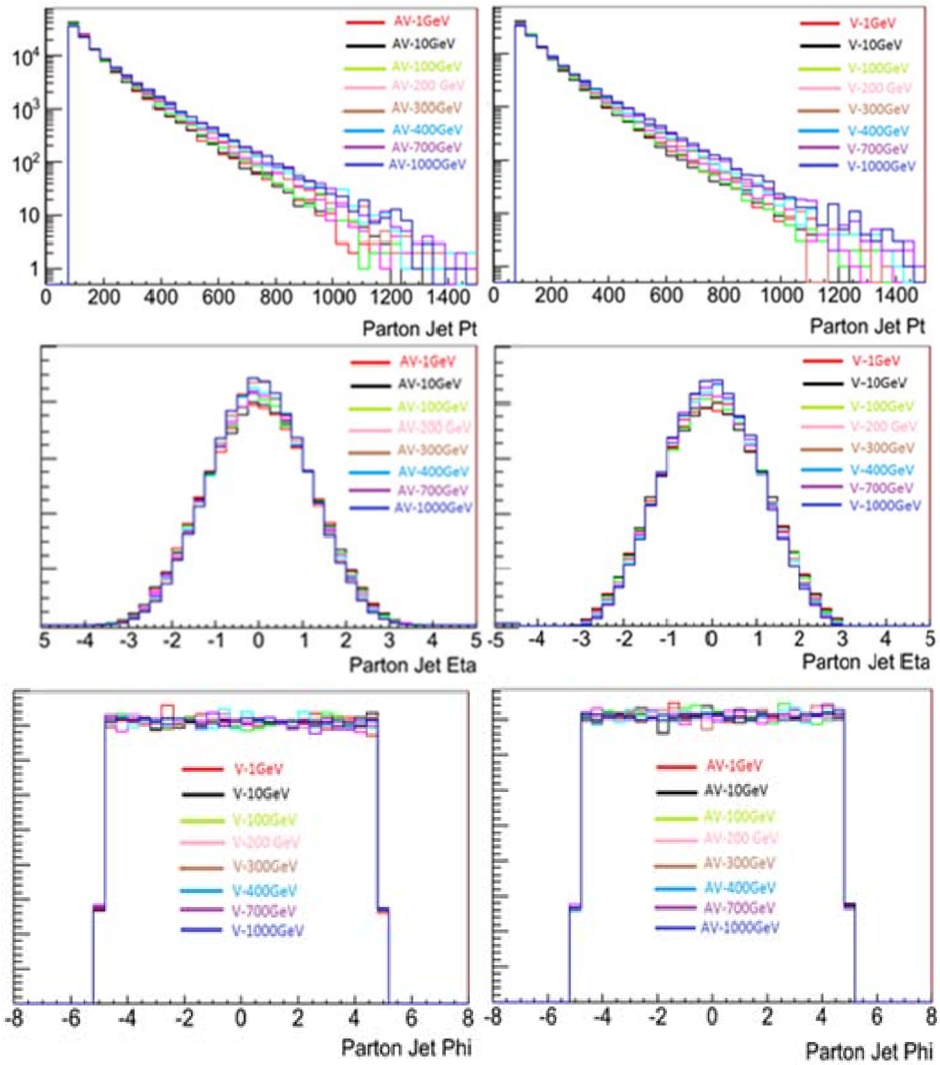

Figure 3.23. Parton jet kinematics distribution.

3.8.6. Effect of Pythia and Geant4 Simulation in Event Production

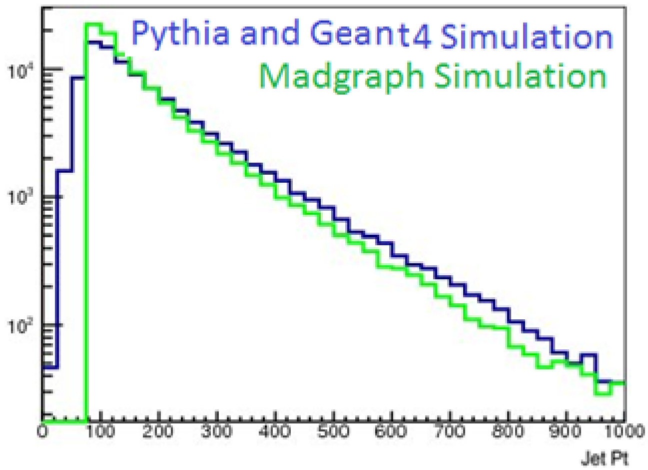

Figure 3.24. Hadronization and simulation.

Aim of this part is to see effect of Pythia and Geant4 simulation on events at production level. Starting of P_t of the jet, selected as 80 GeV for MadGraph. The events which are produced by MadGraph are given to Pythia and Geant4. As it can be seen from the Fig. 3.24, the distributions are not exactly the same for MadGraph and Pythia. This difference is due to technical problems (Pythia and Geant4 may not hadronize some events) and applied cuts during analysis.

3.8.7. Cross Section & Dark Matter Mass

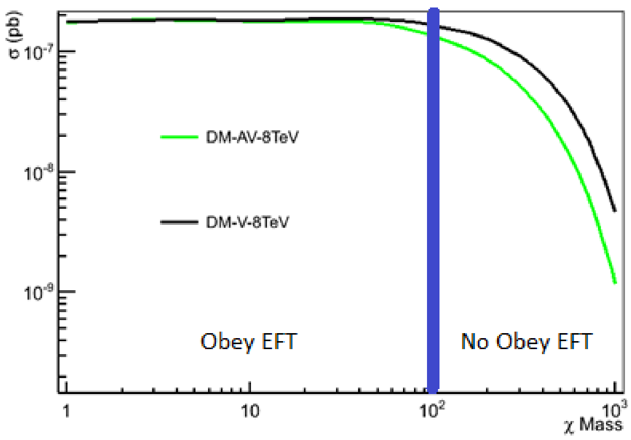

Figure 3.25. Cross section as a function of dark matter mass.

It is important to look at relation between DM mass and cross section. In order to set the best limit on AV and V models, we need to find the zone which is satisfying the Effective Field Theory (EFT). So, cross section is a flat between 1 GeV and 100 GeV for DM masses which is accepted by EFT. Once DM mass increases the 100 GeV, cross section goes down and due to that EFT breaks down in that area. This can be seen from the Fig. 3.25 and it means that we can get best limit results in EFT area. So we need to focus on EFT zone for this analysis.

3.8.8. Acceptance & Dark Matter Mass

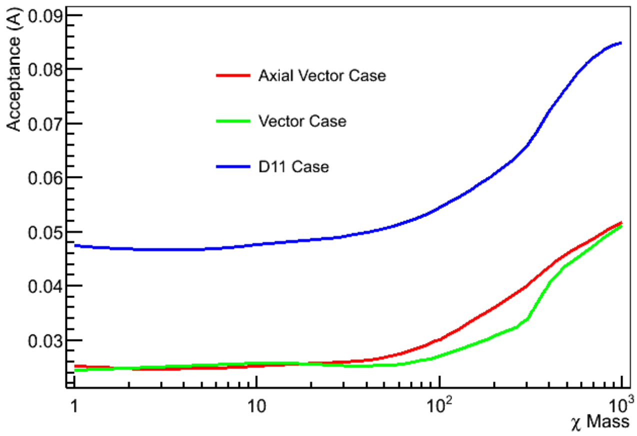

Figure 3.26. Acceptance as a function of DM mass.

There is a relationship between acceptance and limit value of cross section. As it can be seen from Fig. 3.26, acceptance is almost stable until 100 GeV because most of events are out of forbidden zone according to unitarity. In fact, acceptance is increasing after DM mass of 100 GeV. But this is not reliable all the time and we should look at some other parameters, like unitarity, to be sure this is real effect. At high DM masses most of events goes to the forbidden area and we should be careful about safety of our analysis.

4. THE SEARCH FOR MONOJET

4.1. Trigger and Data Samples

The data for this search was collected using the following triggers (see Appendix 2.A);

- HLT_MET120_HBHENoiseCleaned
- MonoCentralPFJet80_PFMETnoMu95_NHEF0p95 4.1
- MonoCentralPFJet80_PFMETnoMu105_NHEF0p95

The HLT_MET120_HBHENoiseCleaned trigger is seeded by the Level 1 triggers L1_ETM36 OR L1_ETM40 OR L1_ETM50 and requires the event to have CaloMet>120 GeV and to pass the HBHENoise filter. The MonoCentralPFJet80_PFMETnoMu trigger is seeded by L1_ETM40 at Level 1 and requires the event to pass the following cuts;

- PFMetnoMu $> 95, 105\ GeV$
- $\mathrm{P_T}(\mathrm{j_1}) > 80GeV$
- $|\eta(j_1)| < 2.6$ 4.2
- $\mathrm{NHEF}(j_1) < 0.95$

where PFMetnoMu is PFMet calculated by excluding the muons and $NHEF(j_1)$ is the fraction of jet energy assigned to neutral hadrons in the ECAL.

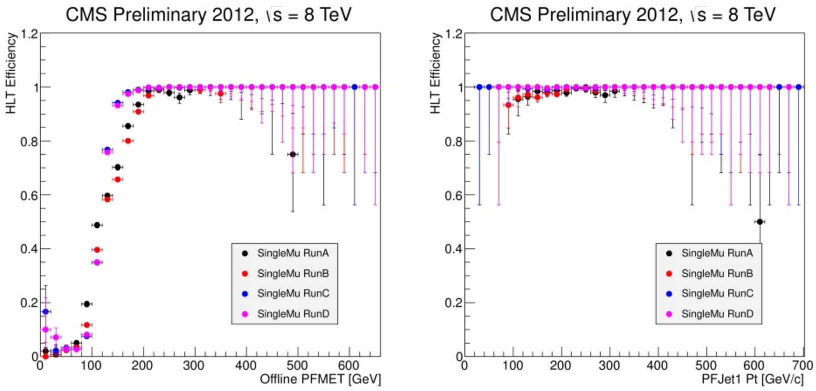

Figure 4.1. The trigger efficiency as a function of the $\boldsymbol{E_{miss}^{T}}$ (left) and $\boldsymbol{P_T}$ of the leading jet (right).

The trigger turn-on curves as a function of E_{miss}^{T} and the P_T of the leading jet are shown in Fig. 4.1. The trigger efficiency is calculated from an independent sample of events collected using the HLT_IsoMu24_eta2p1 trigger path (unprescaled). The plots show that the trigger paths become almost 100 % efficient at $P_T(j_1) \sim 110\ GeV$ and $E_{miss}^{T} \sim 220\ GeV$.

Table 4.1. Datasets with a total integrated luminosity of 19.5 fb^{-1}.

Era	Run Range	DataSet	L [pb^{-1}]
2012A	190782-190949	/MET/Run2012A-recover-06Aug2012-v1	82
2012A	190456-193686	/MET/Run2012A-13Jul2012-v1/	809
2012B	193752-196531	/MET/Run2012B-13Jul2012-v1/	4404
2012C	198049-198522	/MET/Run2012C-24Aug2012-v1/	495
2012C	198934-203002	/MET/Run2012C-PromptReco-v2/	6311
2012D	203894-208686	/MET/Run2012D-PromptReco-v1/	7274
		Total Integrated Lumi	**19500**

The data are collected on the MET primary datasets. The events are reconstructed with the CMSSW_5_3_2_patch4 release. The datasets and the specific data reprocessing and luminosity used in this analysis is listed in Table 4.1.

4.2. Signal and Background Monte Carlo Samples

The Standard Model processes considered are single top and top quark pair production, W or Z produced in association with jets and QCD processes. Monte Carlo (MC) simulation samples used in this analysis to model the backgrounds are listed in Table 4.2.

The Z+Jets MADGRAPH sample contains only events where the Z boson decays into electrons, muons or taus. The $Z(\nu\nu)$ +jets MADGRAPH sample contains only events where the Z boson decays into the three generations of neutrinos. The hadronization and fragmentation of quarks and gluons (along with the underlying event) are performed using PYTHIA with the MLM shower matching prescription (S. Hoche, F. Krauss, N. Lavesson, 2006), which avoids double counting due to parton showering. The PYTHIA Tune Z2 is used for each sample, unless otherwise specified. Pile-up effects have been included in the simulation.

Table 4.2. Standard Model Monte Carlo simulation samples.

DataSet	Xsec(pb)	L [fb^{-1}]
/DYJetsToLL_PtZ-100_TuneZ2star_8TeV_ madgraph/Summer12_PU_S10/AODSIM	34	77.3
/ZJetsToNuNu_50_HT_100_TuneZ2Star_8TeV_madgraph/Summer12_PU_S10/AODSIM	381	10.6
/ZJetsToNuNu_100_HT_200_TuneZ2Star_8TeV_madgraph/Summer12_PU_S10/AODSIM	160	27.6
/ZJetsToNuNu_200_HT_400_TuneZ2Star_8TeV_madgraph/Summer12_PU_S10/AODSIM	42	121.8
/ZJetsToNuNu_400_HT_inf_TuneZ2Star_8TeV_madgraph/Summer12_PU_S10/AODSIM	53	190
/WJetsToLNu_PtW_100_TuneZ2star_8TeV_madgraph/Summer12_PU_S10/AODSIM	229	55.7
/TTJets_MassiveBinD_TuneZ2star_8TeV_madgraph_tauola/Summer12_PU_S10/AODSIM	225	30.7
/QCD_Pt_300_to_470_TuneZ2star_8TeV_pythia6/Summer12_PU_S10/AODSIM	1760	3.4
/QCD_Pt_470_to_600_TuneZ2star_8TeV_pythia6/Summer12_PU_S10/AODSIM	114	35.1
/QCD_Pt_600_to_800_TuneZ2star_8TeV_pythia6/Summer12_PU_S10/AODSIM	27	148
/QCD_Pt_800_to_1000_TuneZ2star_8TeV_pythia6/Summer12_PU_S10/AODSIM	3.6	1.1
/QCD_Pt_1000_to_1400_TuneZ2star_8TeV_pythia6/Summer12_PU_S10/AODSIM	0.7	2654.2
/QCD_Pt_1400_to_1800_TuneZ2star_8TeV_pythia6/Summer12_PU_S10/AODSIM	0.03	58090
/QCD_Pt_800_to_inf_TuneZ2star_8TeV_pythia6/Summer12_PU_S10/AODSIM	0.002	543103
/T-s-channel_TuneZ2star_8TeV_powheg_tauola/Summer12_PU_S10/AODSIM	3.8	68.6
/T-t-channel_TuneZ2star_8TeV_powheg_tauola/Summer12_PU_S10/AODSIM	55.5	67.2
/T-tW-channel_TuneZ2star_8TeV_powheg_tauola/Summer12_PU_S10/AODSIM	11.2	44.5
/Tbar-s-channel_TuneZ2star_8TeV_powheg_tauola/Summer12_PU_S10/AODSIM	1.8	80
/Tbar-t-channel_TuneZ2star_8TeV_powheg_tauola/Summer12_PU_S10/AODSIM	30	64.5
/Tbar-tW-channel_TuneZ2star_8TeV_powheg_tauola/Summer12_PU_S10/AODSIM	11	44.1

4.3. Event Selection

We describe below the set of criteria used to select monojet events. The data events collected by the above mentioned triggers are required to pass a set of event cleaning criteria.

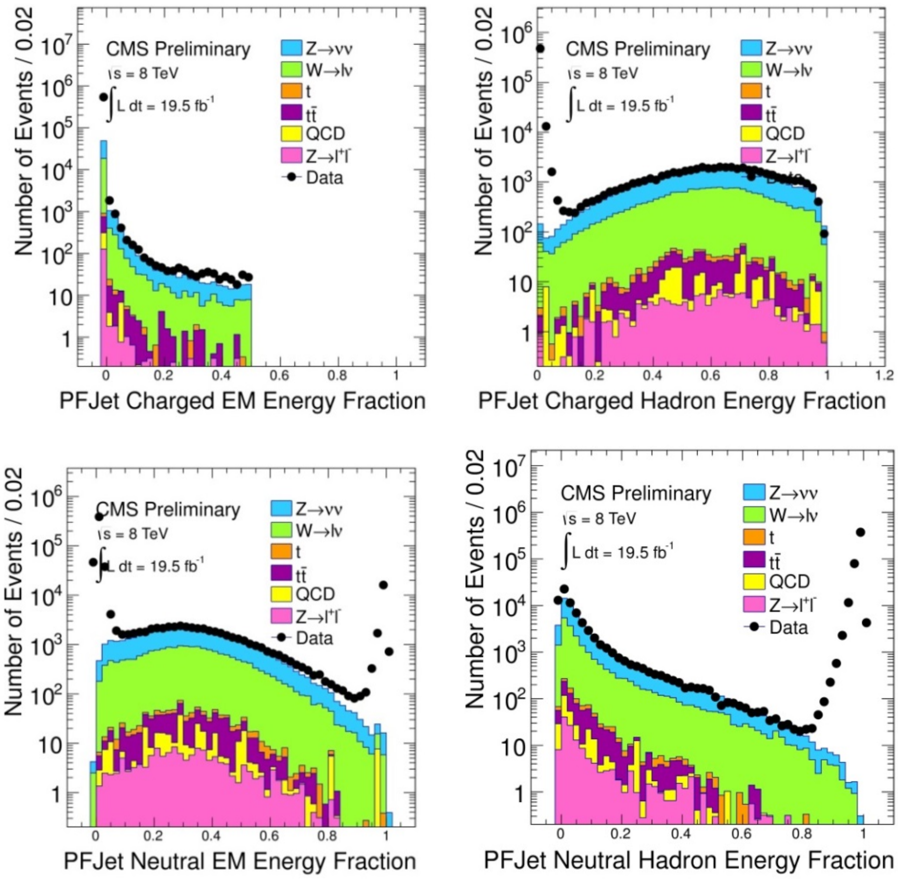

Figure 4.2. Hadronic and electromagnetic energy fractions from charged and neutral particles, before cleanup cuts on these quantities are applied. We require the charged hadronic fraction of the jet to be above 20% and the neutral electromagnetic and hadronic energy fractions to be below 70% of the total jet energy.

“Events are required to have at least one primary vertex reconstructed within a 24 cm window along the beam axis” (Collaboration, 2011), a radius of $r < 2$ cm orthogonal to the beam and a number of degrees of freedom larger than 4 (CMS Collaboration, 2010). Beam halo and cosmic muons can deposit energy in both the

ECAL and HCAL with no associated charged track: “the fraction of jet energy carried by charged hadrons is therefore required to be above 20%. In order to reject high-P_T photons and electrons misidentified as hadronic jets, the energies assigned to neutral hadrons in the ECAL and HCAL must sum to less than 70% of the total jet energy” (CMS Collaboration, 2011). A summary of these noise cleaning cuts is below;

- Charged HAD fraction > *0.2*
- Neutral EM fraction < *0.7* 4.3
- Neutral HAD fraction < *0.7*

The distributions for the neutral and charged energy fractions of the leading jet before and after these set of noise cleaning cuts applied are shown in Fig. 4.2 and Fig. 4.3. The jets are required to have $P_T > 30\ GeV/c$ and $|\eta| < 4.5$.

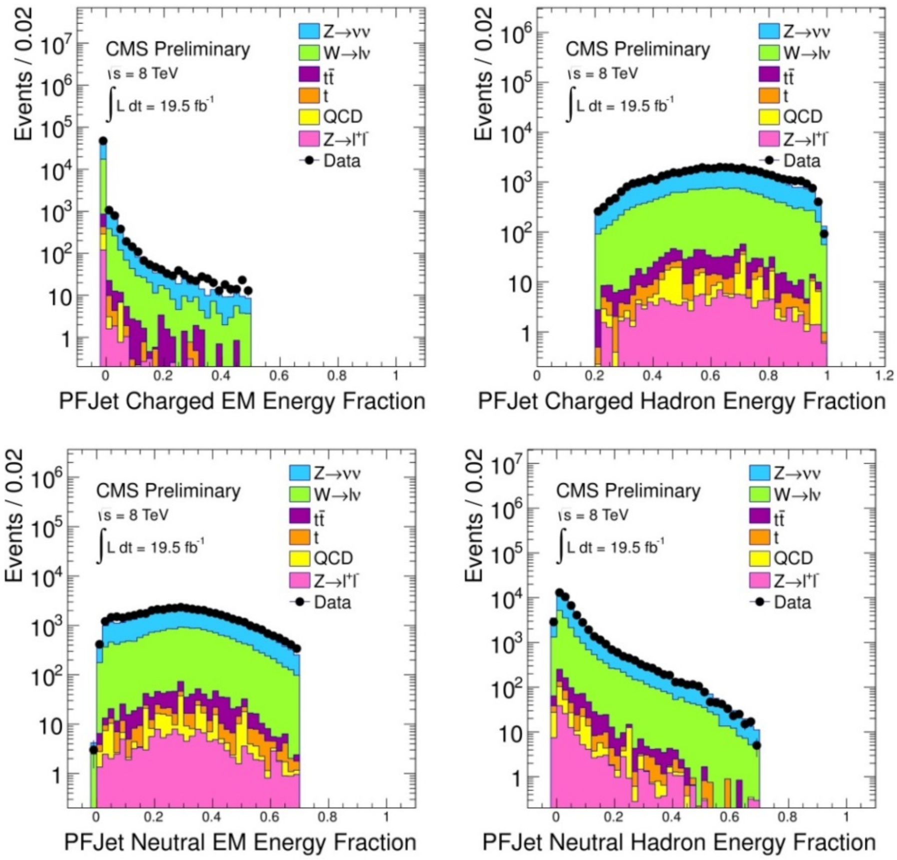

Figure 4.3. Hadronic and electromagnetic energy fractions from charged and neutral particles, after cleanup cuts on these quantities are applied.

Jets and E_{miss}^{T} are reconstructed using a particle flow technique (CMS Collaboration, 2009). "The algorithm produces a unique list of particles in each event, using the combined information from all CMS subdetectors" (CMS Collaboration, 2011). This list is then used as input to the jet clustering, which reconstructs jets using the anti-$\mathrm{k_t}$ algorithm (M. Cacciari, G. P. Salam, and G. Soyez, 2008) with a distance parameter of 0.5. "The missing transverse energy vector is computed as the negative vector sum of the transverse momenta of all particles reconstructed in the event" (CMS Collaboration, 2011). In this analysis, the E_{miss}^{T} is calculated by excluding the muons. Jet energies are corrected to establish a uniform calorimeter response in η and an absolute response in P_T calibrated at the particle level. Jet-energy-scale corrections are derived from simulation, and a residual correction is derived from the data by measuring the P_T balance in dijet events (CMS

Collaboration, 2010). The Jet energy corrections used are 'L2L3Residual' (the residual calibration of data) and 'L1FastJet'. To resolve any disambiguity in the reconstruction of jets and leptons, a jet is removed from the event if the energy fraction of a PFElectron or PFMuon in the jet is greater than 0.5. The analysis is performed in 7 regions of E_{miss}^{T}; E_{miss}^{T} > 250, 300, 350, 400, 450, 500 and 550 GeV. The most energetic jet (j_1) in the event is required to have $P_T(j_1)$ > 110 GeV and $|\eta| < 2.4$. Events with more than two jets (N_{jets} > 2) with $P_T(j_2)$ above 30 GeV and $|\eta|$ < 4.5 are discarded. In order to increase the signal efficiency a second jet (j_2) is allowed, provided that the angular separation with the highest-P_T jet satisfies $\Delta\varphi(j_1, j_2) < 2.5$, a selection that suppresses QCD dijet events. In order to reduce the background from W-boson decays, events with leptons are rejected. Events containing a PFElectron with P_T > *10 GeV* and passing the WP95 selection are rejected. Events containing a PFMuon with P_T > *10 GeV* and reconstructed as a Global and/or Tracker muon are also rejected. In addition, a tau veto is applied to remove background from hadronic taus. An event with a PFTau passing the following selection is removed;

- $P_T > 10\ GeV$
- $|\eta| < 2.3$
- HPS tau passing loose combined isolation discriminant
- pass Decay Mode Finding
- passes Against Electron Loose discriminant
- passes AgainstMuonTight2 discriminant

A control sample of μ+jet events is used to estimate backgrounds in a data-driven way. In addition to kinematic and identification requirements, muon candidates are also required to be isolated. "The relative combined isolation R is defined as the sum of the P_T of the charged hadrons, neutral hadrons and photon contributions computed in a cone of radius 0.4 around the lepton direction, divided by the lepton P_T" (CMS Collaboration, 2011);

$$R = \frac{\sum_i \left(P_{T_i}(chargedHadron) + P_{T_i}(neutralHadron) + P_{T_i}(Photon) \right)}{P_T}. \quad 4.4$$

A summary of the kinematic, identification and isolation selection criteria for muons is shown below;

Muon Identification

- $P_T > 20\ GeV$
- $|\eta| < 2.1$
- Global and tracker muon
- $|d_{xy}| < 0.2\ mm$
- $\frac{\chi^2}{dof} < 10$
- $R < 0.2$
- Tracks associated to muons must satisfy:
- at least one pixel hit,
- at least ten total hits (strip + pixel),
- at least two matches in the muon stations,
- at least one standalone hit.

A summary of all the selection criteria is given in Appendix 2.B. The $P_T(j_1)$, $\eta(j_1)$, N_{jets} and $\Delta\varphi(j_1, j_2)$ distributions are shown in Fig. 4.4 where the full monojet selection has been applied with a E_T^{miss} cut of 250 GeV. All the distributions have been normalized as described in Appendix 2.C.

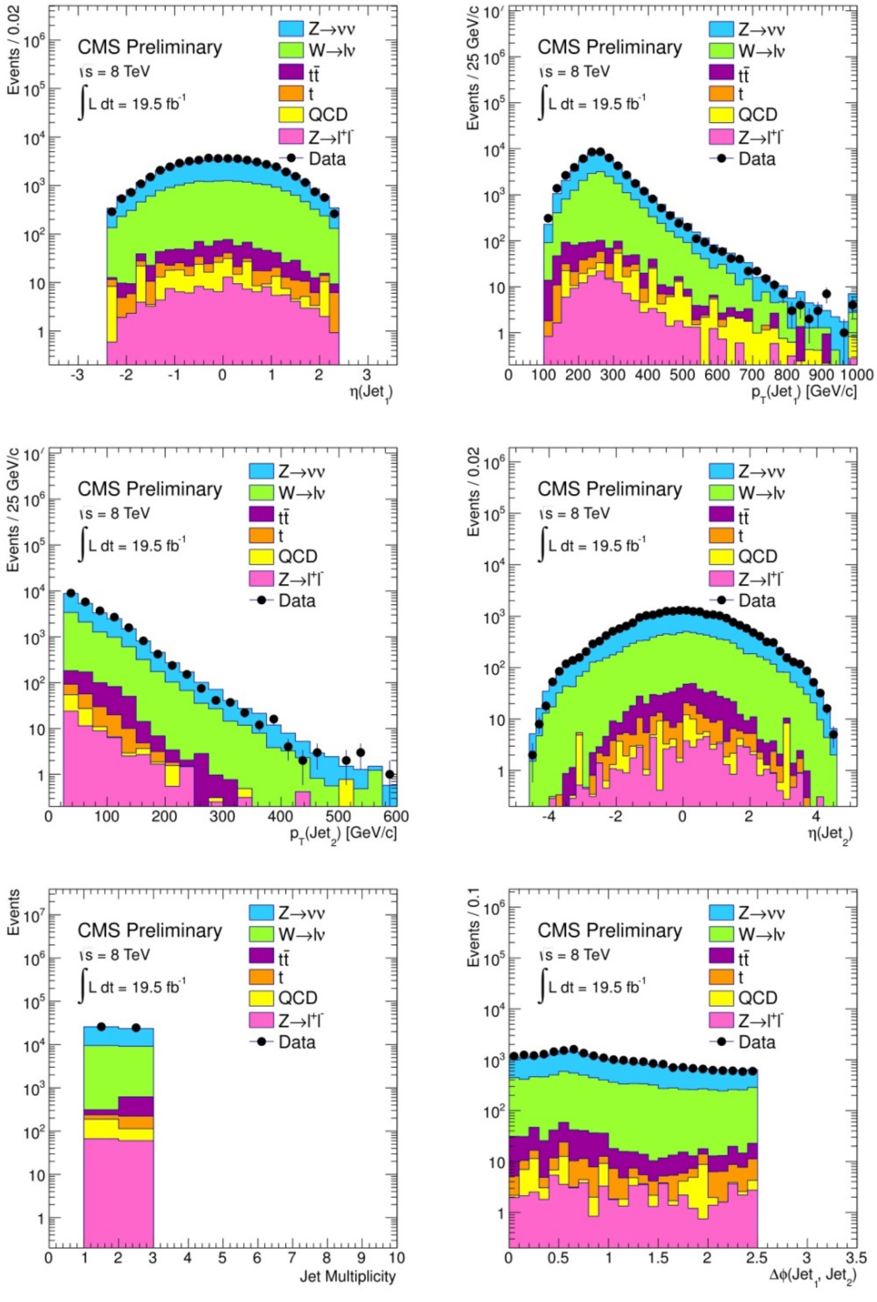

Figure 4.4. Plots of basic selection variables for jets. The figures are shown with all analysis cuts applied.

The distribution of E_T^{miss} for data and background after selecting monojet events and for a E_T^{miss} cut of 250 GeV is shown in Fig. 4.5. The E_T^{miss} cut used in the interpretation of results is chosen based on an optimization study using representative signal samples for each of the three new physics scenarios as described in Appendix

2.D. The best expected limits for ADD and DM are obtained for $E_T^{miss} > 300\ GeV$ and at $E_T^{miss} > 400\ GeV$.

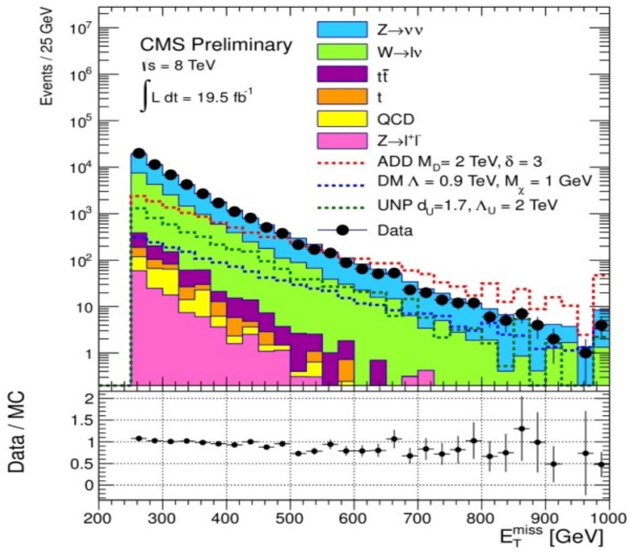

Figure 4.5. The $\boldsymbol{E_T^{miss}}$ distribution after all selection cuts are applied for data and MC.

Table 4.3 lists the number of events selected at each step of the analysis, for data and simulation.

Table 4.3. Number of selected events for data and simulation.

Selection	W+j	Z+j	Znunu+j	TTbar	OCD	SingleT	Total MC	Data
Trigger	1858501	145917	1033984	446823	765940	74416	4325580	20550144
$E_T^{miss} > 200$	204259	22864	120257	59885	49528	8791	465584	1558697
Noise Clean	189218	21339	111922	56523	46207	8085	433293	595911
$j_1: P_T > 110$	183056	20348	106463	50520	46076	7334	413798	562753
$N_{Jets} \leq 2$	160810	15056	80792	8585	15238	2723	283203	349924
$\Delta\varphi(j_1, j_2)$	147081	13798	75397	7150	585	2217	246228	301767
Muon Veto	64379	800	75395	2639	562	868	144644	175252
Elect. Veto	47702	531	75374	1603	543	610	126364	154411
Tau Veto	45839	491	74870	1506	526	573	123805	151087
$E_T^{miss} > 250$	14153	120	28818	470	177	156	43894	50419
$E_T^{miss} > 300$	5054	40	11999	175	76	52	17395	19108
$E_T^{miss} > 350$	2060	17	5469	72	23	20	7661	8056
$E_T^{miss} > 400$	919	7	2679	32	3	7	3647	3677
$E_T^{miss} > 450$	444	4	1406	13	2	2	1871	1772
$E_T^{miss} > 500$	228	1	766	6	1	1	1004	894
$E_T^{miss} > 550$	112	1	429	3	0	0	545	508

4.4. Data Driven Background Estimation

The dominant backgrounds remaining after the monojet event selection are electroweak backgrounds from "invisible Z" decays and W+jets. Both of these backgrounds are estimated from data by selecting a control sample of μ + jets events, where $Z(\mu\mu)$+jets is used to predict the invisible Z background and $W(\mu\nu)$ +jets is used to predict the remaining W+jets background. This muon control sample is derived from the same dataset as the signal.

The control samples are obtained by applying the full monojet selection with the exception of the lepton veto. In order to obtain a sample of $Z(\mu\mu)$ events, one well identified and isolated muon satisfying the selection in Section 4.3 is required and the invariant mass of this muon with another reconstructed muon in the event is required to be between 60 and 120 GeV. A sample of W($\mu\nu$) +jets is similarly obtained by requiring one well identified and isolated muon and with a reconstructed W transverse mass between 50 and 100 GeV.

Tables 4.4 and 4.5 show the event yields obtained for the Z($\mu\mu$) and W($\mu\nu$) control samples and the predicted backgrounds from MC.

Table 4.4. Event yields for the Z($\boldsymbol{\mu\mu}$) data control samples and MC.

$\mathrm{E_T^{miss}}$ Cuts	Z+jets	W+jets	Z(nunu)+jets	ttbar	single t	qcd	All MC	Data
$\mathrm{E_T^{miss}} > 250$	3405.2	0.5	0	27.4	10.6	0	3443.7	3626
$\mathrm{E_T^{miss}} > 300$	1493.7	0	0	8.8	4.1	0	1506.6	1485
$\mathrm{E_T^{miss}} > 350$	696.2	0	0	4.4	3.1	0	703.7	663
$\mathrm{E_T^{miss}} > 400$	344.9	0	0	0	0.3	0	345.8	323
$\mathrm{E_T^{miss}} > 450$	177.1	0	0	0	0	0	177.1	173
$\mathrm{E_T^{miss}} > 500$	97.1	0	0	0	0	0	97.1	84
$\mathrm{E_T^{miss}} > 550$	54.4	0	0	0	0	0	54.4	47

Table 4.5. Event yields for the W($\boldsymbol{\mu\nu}$) data control samples and MC.

$\mathrm{E_T^{miss}}$ Cuts	W+jets	Z+jets	Z($\nu\nu$)+jets	ttbar	single t	qcd	All MC	Data
$\mathrm{E_T^{miss}} > 250$	12218.6	377.7	0	595	185.6	0	13376.9	15578
$\mathrm{E_T^{miss}} > 300$	5219	140.3	0	216.5	72.9	0	5648.7	6347
$\mathrm{E_T^{miss}} > 350$	2403.2	61.3	0	79.3	31.9	0	2575.7	2893
$\mathrm{E_T^{miss}} > 400$	1198	32.1	0	39.8	13.3	0	1283.2	1381
$\mathrm{E_T^{miss}} > 450$	606.3	16.6	0	20.5	7.7	0	651.1	715
$\mathrm{E_T^{miss}} > 500$	317	9.3	0	9.2	4.2	0	339.7	378
$\mathrm{E_T^{miss}} > 550$	176.6	5.5	0	6.5	3.3	0	191.9	207

A comparison between data and MC for the dimuon invariant mass and momentum after all the selection cuts and a E_T^{miss} cut of 250 GeV/c is shown in Fig. 4.6. A comparison between data and MC for the transverse mass and momentum of the W after the full selection and a E_T^{miss} cut of 250 GeV/c is shown in Fig. 4.7, where the missing transverse energy is defined as the vector sum of the muon transverse momentum and missing transverse energy to emulate the missing energy in events where the lepton is lost.

4.5. Estimation of Z($\nu\nu$) Background

The Z($\mu\mu$) and Z($\nu\nu$) events share similar kinematic characteristics and by interpreting the pair of muons as missing energy, the topology of the process in which the Z boson decays to neutrinos can be reproduced. The missing transverse energy in the Z($\mu\mu$) event is defined as the vector sum of the transverse momentum of the muons and the E_T^{miss}.

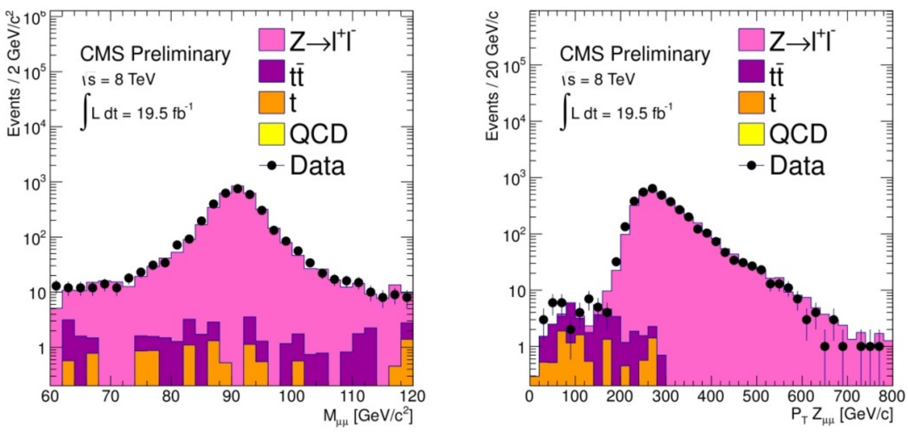

Figure 4.6. Invariant mass and transverse momentum of the dimuon pair in the Z($\boldsymbol{\mu\mu}$) control sample.

The number of Z($\nu\nu$) events can then be predicted using;

$$N(Z \to \nu\nu) = \frac{N_{obs} - N_{bgd}}{A * \varepsilon} R\left(\frac{Z \to \nu\nu}{Z \to ll}\right) \qquad 4.5$$

where “N_{obs} is the number of observed dimuon events, N_{bgd} is the number of background events contributing to the dimuon sample, A is the fiducial and kinematic acceptance of the detector and the efficiency of the Z mass window cut, ε is the selection efficiency of the event and R is the ratio of branching fractions for the Z decay to neutrinos and a pair of muons” (CMS Collaboration, 2011). These factors are determined as follows;

- $\boldsymbol{N_{bgd}}$ **:** The dimuon sample comprises predominantly of Z($\mu\mu$) events with less than 1% contamination from background. The backgrounds are taken from Monte Carlo and a 50% uncertainty is assigned to the number.
- $\boldsymbol{A}$ **:** The acceptance A is defined as the fraction of all generated events where the muons are reconstructed with P_T > *20* GeV and $|\eta|$ < 2.1 and the invariant mass of the muons is within 60 GeV and 120 GeV. This is obtained from Z+jets MC using generator level information.
- $\boldsymbol{\varepsilon}$ **:** The event selection efficiency ε is defined as the efficiency of reconstructing muons passing all the identification and isolation criteria and with an invariant mass between 60 and 120 GeV, given that they are within the detector acceptance. The efficiency is taken from MC and corrected by a scale factor to account for the difference in efficiency between data and MC, where the data/MC scale factor is found to be 0.957.
- $\boldsymbol{R}$ **:** The ratio of the branching fraction R is obtained from (Particle Data Group Collaboration, 2010) and is 5.942 ± 0.019 when $l = \mu$.

Table 4.6. Summary of the Z($\boldsymbol{\nu\nu}$) event yields.

E_T^{miss} (GeV)	250	300	350	400	450	500	550
N_{obs}	3626	1485	663	323	173	84	47
N_{bgd}	38	13	7	1	0	0	0
A	0.861	0.891	0.914	0.927	0.933	0.943	0.952
ε	0.809	0.81	0.807	0.804	0.789	0.789	0.794
R	5.942	5.942	5.942	5.942	5.942	5.942	5.942
$N_{Z\rightarrow\nu\nu}$	30600 ± 1493	12119 ± 640	5286 ± 323	2569 ± 188	1394 ± 127	671 ± 81	370 ± 58

Table 4.7. Summary of the contributions to the total uncertainty on Z($\boldsymbol{\nu\nu}$).

Uncertainty(GeV)	250	300	350	400	450	500	550
N_{obs}	1.7	2.6	3.9	5.6	7.6	10.9	14.6
N_{bgd}	0.8	0.6	0.8	0.2	0	0	0
A	2.0	2.0	2.0	2.1	2.1	2.2	2.4
ε	2.0	2.0	2.0	2.1	2.4	2.7	3.1
Total	4.5	4.9	5.8	7.1	8.9	12.1	15.6

Table 4.6 shows the observed Z($\mu\mu$) event yields and the correction factors for various E_T^{miss} cuts. Also shown is the estimated Z($\nu\nu$) background. A summary of the fractional contributions of the uncertainties to the total error on the Z($\nu\nu$) background is shown in Table 4.7. The dominant uncertainty is the statistical uncertainty from the size of the Z($\mu\mu$) sample.

4.6. Estimation of W+jets Background

The second most dominant background arises from W+jet events that are not removed by the explicit lepton veto cut. These can come from hadronically decaying taus or events in which the lepton (electron or muon) is not identified, not isolated or not within the acceptance region. Such events in which the electron, muon or hadronic tau are effectively ‘lost’ are estimated by using the W(μν)+jets control sample.

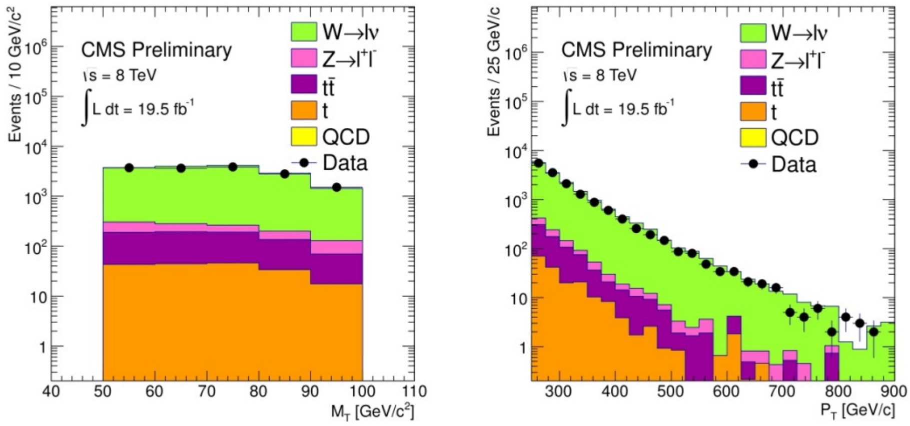

Figure 4.7. Transverse mass and transverse momentum of $\boldsymbol{W}^{\pm}$ candidates in the single-muon sample.

The W($\mu\nu$) events are first corrected for the acceptance (A') and efficiency of reconstructing the events (ε') in the detector to obtain the total number of generated events N^{μ}_{tot};

$$N^{\mu}_{tot} = \frac{N_{Data} - N_{bgd}}{A' \times \varepsilon'}. \tag{4.6}$$

This is subsequently weighted by the inefficiency factors (detailed below) to obtain the predicted number of events that would not be rejected by the lepton veto and thus remain in the monojet sample.

The total number of W($\mu\nu$)+jet events that are out of the acceptance and not identified or isolated can be written as;

$$N_{lost\ \mu} = N^{\mu}_{tot} * (1 - A_{\mu}\varepsilon_{\mu}) \tag{4.7}$$

where A_{μ} is the acceptance and ε_{μ} is the efficiency of the muon selection used in the lepton veto definition.

Similarly, for an estimation of the 'lost' electron background, we start with N^{μ}_{tot} and multiply by the ratio of the W($\mu\nu$) and W($e\nu$) events that are predicted at the generator level in MC (f_e) to obtain N_{tot} for electrons. The lost electron background is given by;

$$N_{tot}^{e} = N_{tot}^{\mu} * f_e \qquad \text{where } f_e = \frac{N_{gen}^{e}}{N_{gen}^{\mu}} \tag{4.8}$$

$$N_{lost\ e} = N_{tot}^{e} * (1 - A_e \varepsilon_e) \tag{4.9}$$

where A_e is the acceptance and ε_e is the efficiency of the electron selection used in the lepton veto definition. The electron acceptance is obtained using generator level MC and the selection efficiency is also obtained from MC with an assumed data/MC scale factor of 1.0.

The component of the W+jets background from hadronic tau events is estimated in the same way. The ratio of the generated W($\mu\nu$) and hadronic tau events (f_τ) is taken from MC and used to obtain N_{tot} for tau events. This is subsequently weighted by the inefficiency of the tau selection used in the veto to obtain the 'lost' hadronic tau background.

$$N_{tot}^{\tau} = N_{tot}^{\mu} * f_\tau \qquad \text{where } f_\tau = \frac{N_{gen}^{\tau}}{N_{gen}^{\mu}} \tag{4.10}$$

$$N_{lost\ \tau} = N_{tot}^{\tau} * (1 - A_\tau \varepsilon_\tau). \tag{4.11}$$

The tau ID efficiency is estimated from MC with a data/MC scale factor of 1.0 and assigned an uncertainty of 6% as recommended by the Tau POG. The electron and muon discriminants in the Tau ID selection can also result in the Tau veto rejecting electron and muon events. The probability of an electron or muon to fake tau is estimated from the W+jets MC and found to be negligible (below 0.1%).

All of the above components can be summarized in a Master Equation for estimating the 'Lost' W background;

$$N_{lost} = \frac{N_{Data} - N_{bgd}}{A'\varepsilon'} * \left[\left(1 - A_\mu \varepsilon_\mu\right) + f_e * (1 - A_e \varepsilon_e) + f_\tau * ((1 - A_\tau \varepsilon_\tau))\right]. \tag{4.12}$$

The factors in eq. 4.12 used to estimate the lost muon, electron and hadronic tau backgrounds are detailed in Table 4.8. A summary of the estimated remaining W+jets events in the monojet sample is shown in Table 4.9.

Table 4.8. Estimation of the remaining W+jets background from the lost electron, muon and hadronic tau contributions.

E_T^{miss} Cut	250	300	350	400	450	500	550
Nobs	15578	6347	2893	1381	715	378	207
Nbgd	1158	429	172	85	45	23	15
$A'\varepsilon'$	0.320	0.331	0.338	0.341	0.340	0.340	0.340
N_{tot}^{μ}	44953	17832	8059	3800	1973	1047	565
Lost Muon							
$A_\mu\varepsilon_\mu$	0.867	0.890	0.905	0.918	0.927	0.929	0.941
$N_{lost\,\mu}$	5991	1955	765	312	144	74	33
Lost Electron							
$A_e\varepsilon_e$	0.552	0.586	0.609	0.622	0.626	0.636	0.654
f_e	0.298	0.282	0.277	0.267	0.266	0.263	0.262
$N_{lost\,e}$	6003	2083	874	383	196	100	51
Lost Tau							
$A_\tau\varepsilon_\tau$	0.092	0.094	0.101	0.107	0.099	0.104	0.093
f_τ	0.138	0.124	0.113	0.103	0.099	0.101	0.084
$N_{lost\,\tau}$	5630	2004	819	350	176	95	43
N_{lost}	17625 ± 681	6042±236	2457±102	1044±51	516±31	269±20	128±13

Table 4.9. Summary of the contributions (in %) to the total uncertainty on the W+jets background from the various factors used in the data-driven estimation.

Uncertainty	250	300	350	400	450	500	550
N_{obs}	0.9	1.3	2.0	2.9	4.0	5.5	7.5
N_{bgd}	2.5	2.3	1.9	2.1	2.1	1.9	2.4
$A'\varepsilon'$	0.1	0.2	0.3	0.5	0.6	0.9	1.2
$A_\mu\varepsilon_\mu$	0.1	0.1	0.2	0.3	0.4	0.5	0.6
$A_e\varepsilon_e$	0.3	0.4	0.6	0.9	1.3	1.7	2.3
$A_\tau\varepsilon_\tau$	0.2	0.4	0.6	0.9	1.3	1.7	2.3
PDFs	2.0	2.0	2.0	2.0	2.0	2.0	2.0
Total	3.9	3.9	4.1	4.9	6.0	7.6	10.1

The uncertainty on the W+jets estimation includes; the statistical uncertainty on the number of single-muon events in the data, a 50% uncertainty on the background events obtained from MC, an uncertainty on acceptance from PDFs (2%) and MC statistics and an uncertainty on the selection efficiency ε from the variation in the data/MC scale factor and MC statistics. A summary of the fractional contributions of these uncertainties to the total error on the W+jets background is shown in Table 4.9. The remaining backgrounds to the monojet sample from ttbar, QCD, single top and Z+jets events are found to be at the 1% level. These are taken from MC and assigned a 50% systematic uncertainty.

4.7. Results

A summary of the predictions and corresponding uncertainties for all the SM backgrounds compared to the data are shown in Table 4.10.

Table 4.10. Summary of the SM background predictions and their corresponding uncertainties compared to the data.

Selection(GeV)	W+j	Z+j	Z(νν)+j	ttbar	qcd	t	Total BG	Data
$E_T^{miss} > 250$	17625± 681	127	30600±1493	470	177	156	49154±1681	50419
$E_T^{miss} > 300$	6042 ± 236	43	12119±640	175	76	52	18506±696	19108
$E_T^{miss} > 350$	2457 ± 102	18	5286±323	72	23	20	7875±343	8056
$E_T^{miss} > 400$	1044 ± 51	8	2569±188	32	3	7	3663±197	3677
$E_T^{miss} > 450$	516 ± 31	4	1394±127	13	2	2	1931±132	1772
$E_T^{miss} > 500$	269 ± 20	2	671±81	6	1	1	949±85	894
$E_T^{miss} > 550$	128 ± 13	1	370±58	3	0	0	501±60	508

4.8 Systematic Uncertainties on Signal

The systematic uncertainties on the background event yields have been described in detail in the previous section. The sources of uncertainties contributing to the signal are;

- Jet energy scale (JES), emulated by shifting the jet 4-vector by an η and P_T dependent factor related to the response. After these corrections, the uncertainty on signal acceptance due to the energy scale of these corrected jets varies between 4% and 6% for the ADD and DM signal. A detailed table showing the systematic on the acceptance for the DM and ADD signal points is given in Appendix 2.E. In addition, a cross-check of the Jet and missing energy scale for the monojet topology is performed using Z($\mu\mu$) events. A detailed description of this cross-check can be found in Appendix 2.F. The E_T^{miss} scale derived using this method is found to be consistent with that from the recommended JES uncertainty.
- Uncertainties on the parton density function. The signal samples are generated using CTEQL1 for DM and CTEQ66 for ADD. We follow the PDF4LHC prescription to estimate the error on acceptance due to PDF

uncertainties. The PDFs used in the uncertainty estimation are CTEQ66, MSTW2000nlo68cl and NNPDF20 100. The results fromCTEQ66 and NNPDF20 100 are similar while theMSTW2000nlo68cl PDFs gave a much smaller error. The error from CTEQ66 PDFs was used as systematic errors on acceptance in the limit calculation.

- Initial state radiation. The DM samples are generated using Madgraph with up to 2 jets so both the leading and the subleading jet in the monojet selection are included in the matrix element calculation. The ISR uncertainty is estimated by changing PYTHIA parameters and quantifying the sensitivity of the acceptance to the matching scale, yielding a variation of 5% for the DM models and 12% for the ADD and Unparticle models.
- The 4.4% uncertainty on the luminosity measurement is incorporated.
- Uncertainty due to the modeling of pile-up interactions in the background samples, estimated by comparing the sensitivity of the acceptance to two different methods of pileup reweighting, is found to be 3%.
- Sensitivity to the renormalization and factorization scale $\mu = \sqrt{\hat{s}}$. We varied the scale from $\mu/2$ to 2μ in the PYTHIA generation step for ADD, Unparticles and DM. The uncertainty on the acceptance was found to be 5% for all three models and the uncertainty on cross section was found to be 10% for ADD and Unparticles and 15% for DM.

The total uncertainty on the signal is almost 20% for all three model points which we used.

4.9. Interpretation and Exclusion Limits

“In order to interpret the consistency of the observed number of events with the background expectation in the context of a model, and also to facilitate comparison with previous results, we set exclusion limits for the ADD model, dark matter production and Unparticles” (CMS Collaboration, 2011). The upper limit on the number of non-SM events consistent with the measurements is set using the CLs method (L. Moneta, K. Cranmer, G. Schott, 2010).

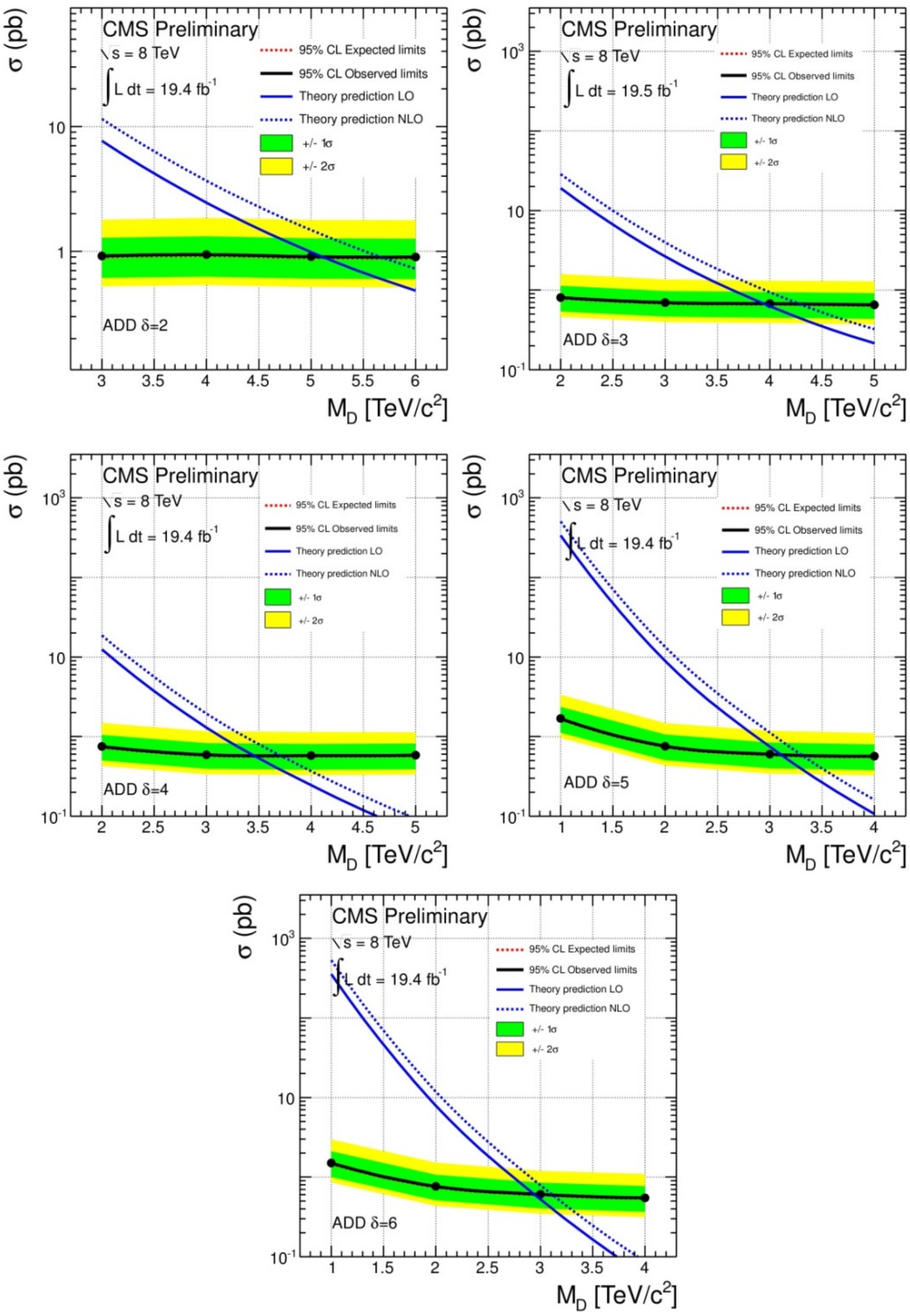

Figure 4.8. 95% CL upper limits on the ADD production rate in pb. The median 1 and 2 ***σ*** values are obtained from the distribution of upper limits obtained in 1000 pseudo-experiments performed at each model point.

In Fig. 4.8, we show the expected limit on the cross-section as a function of M_D for the data and SM expectations along with the observed 95% CL in 1 and 2, for different δ values. The 95% CL exclusion region comprises those values of M_D for which the cross-section is less than the 95% limit. Fig. 4.9 shows a comparison of the limits on M_D as a function of δ from CMS, LEP and the Tevatron experiments. Table 4.11 shows the limits with and without K-factor applied.

Table 4.11. ADD Model Limits on $\boldsymbol{M_D}$ observed and expected limits in TeV/$\mathbf{c^2}$ as a function of $\boldsymbol{\delta}$ at NLO, with K-factors of 1.5 for $\boldsymbol{\delta}$ = {2,3} and 1.4 for $\boldsymbol{\delta}$ = {4,5,6}.

	LO		**NLO**	
$\boldsymbol{\delta}$	**Exp. Limit**	**Obs. Limit**	**Exp. Limit**	**Obs. Limit**
2	5.12	5.10	5.70	5.67
3	3.96	3.94	4.31	4.29
4	3.46	3.44	3.72	3.71
5	3.11	3.10	3.32	3.31
6	2.95	2.94	3.13	3.12

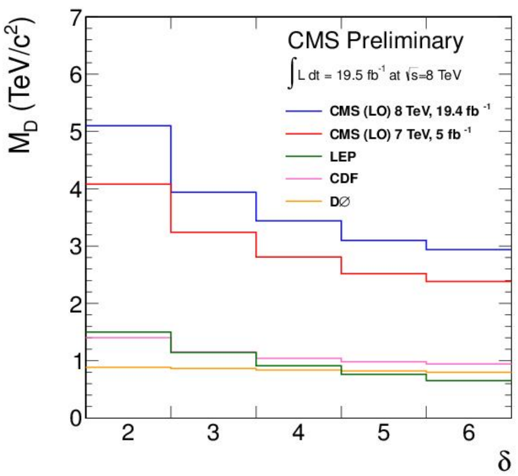

Figure 4.9. Comparison of the limits on M_D as a function of δ from CMS, LEP and the Tevatron experiments (Lep Collaboration, 2004), (CDF Collaboration, 2008), (D0 Collaboration).

.

"For DM models, the observed limit on the cross section depends on the mass of the dark matter particle and the nature of its interaction with the SM particles" (CMS Collaboration, 2011). Since the upper limit on the cross-section depends on our specific event production criteria such as P_T, we convert these limits into limits on the dark matter-nucleon scattering cross section using the following formulas

$$\sigma_{SI} = 9\frac{\mu^2}{\pi\Lambda^4} \quad 4.13$$

$$\sigma_{SD} = 0.33\frac{\mu^2}{\pi\Lambda^4} \quad 4.14$$

$$\sigma_{11} = 7.7 \times 10^{-29}\frac{\mu^2}{\Lambda^6} \text{ where } \mu = \frac{m_\chi m_p}{m_\chi + m_p} \quad 4.15$$

where SI=spin-independent, SD=spin-dependent, μ is reduced mass of dark matter and nucleon, Λ is the effective contact interaction scale and $\Lambda_{u,d}$ are the effective contact interaction scales for up-type and down-type quarks. The observed limits at the 90% CL on the DM-nucleon scattering cross section for the spin dependent and spin independent cases are shown in Table 4.12 and Fig. 4.10.

Table 4.12. "Observed 90% CL limits on the dark matter-nucleon cross section and effective contact interaction scale L for the spin-dependent and spin-independent interactions (CMS Collaboration, 2011)".

M_χ(GeV)	Spin-independent		Spin-dependent	
	Λ(GeV)	$\sigma_{\chi N}(cm^2)$	Λ(GeV)	$\sigma_{\chi N}(cm^2)$
1	892	4.14×10^{-40}	913	1.38×10^{-41}
10	902	1.24×10^{-39}	922	4.15×10^{-41}
100	892	1.53×10^{-39}	868	6.20×10^{-41}
200	863	1.75×10^{-39}	802	8.62×10^{-41}
300	796	2.43×10^{-39}	709	1.41×10^{-40}
400	779	2.66×10^{-39}	669	1.79×10^{-40}
700	597	7.71×10^{-39}	468	7.47×10^{-40}
1000	428	2.90×10^{-38}	312	3.79×10^{-39}

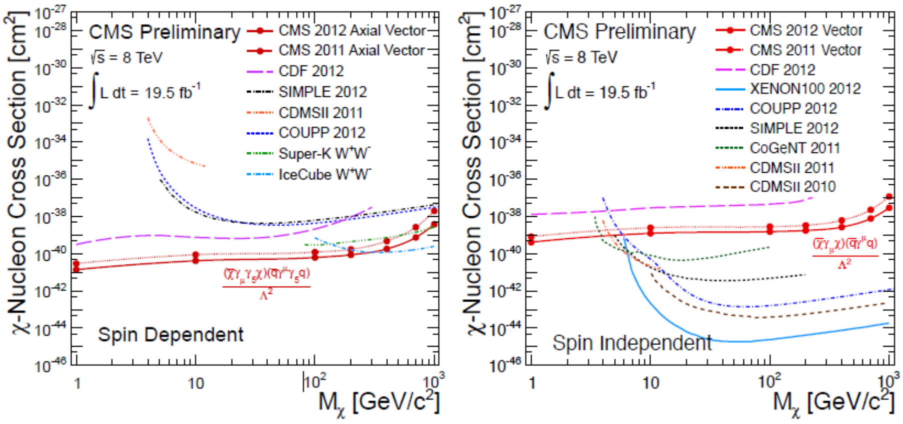

Figure 4.10. CMS 90% CL upper limits on the dark matter-nucleon cross section versus dark matter mass for the vector the axial-vector (COUPP Collaboration, 2012), (M. Felizardo et al, 2012), (CDF Collaboration, 2012), (Super-Kamiokande Collaboration, 2011), (IceCube Collaboration, 2012), (CoGeNT Collaboration, 2011), (XENON100 Collaboration), (CDMS II Collaboration, 2010), (CDMS Collaboration, 2011)

.

For this model, observed limits depend on Λ as a function of the mass of the mediator (M). Now, our aim is to produce mediator mass scan for different DM mass and decay width range as shown in Fig. 4.11.

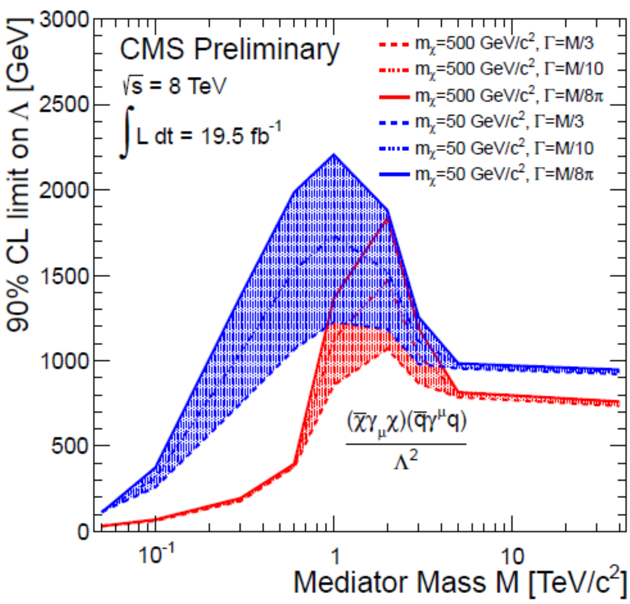

Figure 4.11. Assume vector interactions and a DM mass of 50 GeV/c^2 (blue) and 500 GeV/c^2 (red). The width of the mediator is varied between $\boldsymbol{M/3}$ and $\boldsymbol{M/8\pi}$.

Also, DM-nucleon scattering cross section of Q_{11} which is called as the effective contact interaction is shown in Table 4.13 and Fig. 4.12.

Table 4.13. Observed 90% CL limits on the DM-nucleon cross section for $\boldsymbol{Q_{11}}$.

$\mathbf{M_\chi}$**(GeV)**	**Scalar Operator**	
	$\boldsymbol{\Lambda}$**(GeV)**	$\boldsymbol{\sigma_{\chi N}(cm^2)}$
1	371	3.4×10^{-45}
10	371	1.08×10^{-44}
100	366	1.4×10^{-44}
200	350	1.8×10^{-44}
300	329	2.6×10^{-44}
400	308	3.9×10^{-44}
700	244	1.6×10^{-43}
1000	185	8.3×10^{-43}

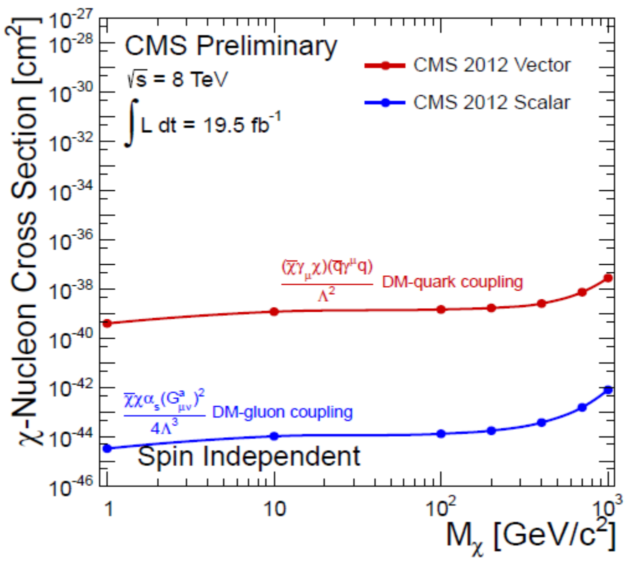

Figure 4.12. CMS 90% CL upper limits on the dark matter-nucleon cross section versus DM mass for the scalar operator.

Another interpretation of our results can be made in the context of Unparticles production. In Fig. 4.13, we show the observed and expected 95% C.L limits on the cross-sections for $S = 0$ Unparticles with $d_U = 1.5, 1.6, 1.7, 1.8, 1.9$. as a function of Λ_U. The observed 95% CL limit for these values of d_U is shown in Table 4.14 and Fig. 4.13.

Table 4.14. 95% CL upper limits on the unparticle production rate.

d_U	2011 Limit(Λ_U)	2012 Limit(Λ_U)
1.4	8.07	-
1.5	2.9	7.45
1.6	1.62	3.36
1.7	1.07	2.47
1.8	-	1.85
1.9	-	1.33

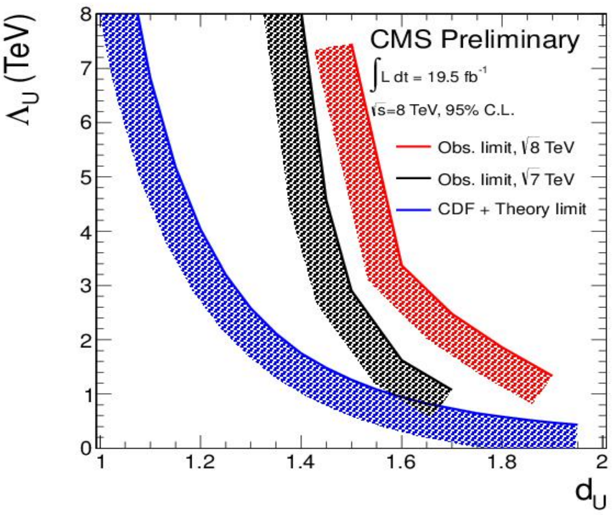

Figure 4.13. 95% CL upper limits on the Unparticles model parameters Λ_U and d_U compared to limits from previous analyses.

5. Conclusions

A search has been performed for signatures of new physics in the monojet and E_T^{miss}channel using 19.5 fb^{-1} of pp collisions at $\sqrt{s}$=8 TeV. Contributions from $t\bar{t}$ and QCD multijet processes are reduced to a negligible level using topological selections. The dominant backgrounds after the complete selection has been applied are from Z($\nu\nu$) and W+jet events. "These are estimated from data samples of Z($\mu\mu$) and W($\mu\nu$) events. The data are found to be in good agreement with expected contributions from SM processes" (CMS Collaboration, 2011). Limits are set on the dark matter-nucleon scattering cross section assuming vector, axial-vector and scalar operators to describe the interaction. In addition, limits are also set on the ADD model parameter M_D as a function of the number of extra dimensions and the production of Unparticles. These constraints are an improvement over previous results.

REFERENCES

BAYATIAN, G. L. and et al., 1998, "CMS Tracker Project Technical Design Report",CERN/LHCC-98-6.

BAYATIAN, G. L. and et al., 1997a, "CMS Electromagnetic Calorimeter Project Technical Design Report", CERN/LHCC-97-33.

BAYATIAN, G. L. and et al., 1997b, "CMS Hadronic Calorimeter Project Technical Design Report",CERN/LHCC-97-31.

BAYATIAN, G. L. and et al., 1997c, "CMS Magnet Technical Design Report", CERN/LHCC-97-10.

BAYATIAN, G. L. AND ET AL., 1997d, "CMS Muons Technical Design Report", CERN/LHCC-97-32.

MANFRED KRAMMER, 2010, "The New Silicon Strip Detectors for the CMS Tracker Upgrade", Mittersteig 2A/DG1.

CMS COLLABORATION, 2008, "Commissioning and Performance of the CMS Pixel Tracker with Cosmic Ray Muons", arXiv:0911.5434.

CMS COLLABORATION, 2010, "Tracking and Vertexing Results from First Collisions", CMS-PAS-TRK-10-001.

WOLFGANG ADAM, R FRÜHWIRTH, ARE STRANDLIE, AND T TODOR., 2005, "Reconstruction of Electrons with the Gaussian-Sum Filter in the CMS Tracker at the LHC", arXiv:physics/0306087.

J. R. VLIMANT, 2007, "Track Reconstruction with the CMS Tracking Detector", In proceedings of HCP07.

FRÜHWIRTH, WOLFGANG WALTENBERGER, AND PASCAL VANLAER, 2007, "Adaptive vertex fitting", Technical Report CMS-NOTE-2007-008. CERN-CMS-NOTE-2007-008.

MATTEO CACCIARI, 2012, "Jets and Area of Jets", LPTHE MCnet-LPCC Summer School.

MATTEO CACCIARI, GAVIN P. SALAM, GREGORY SOYEZ, 2008, "The Catchment Area of Jets", arXiv:0802.1188.

S. CATANI, YU. L. DOKSHITZER, M. H. SEYMOUR, AND B. R. WEBBER, 1993, "Longitudinally invariant kt-clustering algorithms for hadron-hadron collisions", Nuclear Physics B, 406(1-2):187 – 224.

STAN BENTVELSEN AND IRMTRAUD MEYER, 1998, "The cambridge jet algorithm: features and applications", The European Physical Journal C - Particles and Fields, 4:623–629.

GAVIN P. SALAM AND GREGORY SOYEZ, 2007, "A practical Seedless Infrared-Safe Cone jet algorithm", JHEP, 05:086.

CMS COLLABORATION, 2013, "Performance of CMS muon reconstruction in pp collision events at sqrt(s) = 7 TeV", arXiv:1206.4071.

CMS OUTREACH, 2012, http://cmsinfo.cern.ch/outreach/.

CMS COLLABORATION, 2002, "Data Acquisition and High-Level Trigger", CERN/LHCC 02-26 CMS TDR 6.

ARMIN BURGMEIER, 2011, "Data-driven Estimation of Z_0 Background Contributions to the Higgs Search in the H $\rightarrow \tau^+\tau^-$ Channel with the CMS Experiment at the LHC", IEKP-KA/2011-21.

T. SJOSTRAND, S. MRENNA, AND P. Z. SKANDS, 2006, "PYTHIA 6.4 physics and manual", arXiv:hep-ph/0603175.

GEANT4 COLLABORATION, 2003, "GEANT 4 – a simulation toolkit", Nucl. Inst. Meth. 506 250, doi:10.1016/S0168-9002(03)01368-8.

MATTEO CACCIARI AND GAVIN P. SALAM, 2007, "Pileup subtraction using jet areas", LPTHE-07-01.

JAMES BALLIN, 2010, "Particle Flow at CMS & the ILC", CERN-THESIS-2010-086.

TRIMBLE, V., 1987, "Existence and nature of dark matter in the universe", Annual Review of Astronomy and Astrophysics 25: 425–472.

DANIEL BAUMANN, 2008, Cosmology, Lectures.

T. FALK, A. FERSTL, AND K. A. OLIVE, 2000, "Variations of the Neutralino Elastic Cross-Section with CP Violating Phases", Astropart. Phys. 13, 301–316.

G. BELANGER, F. BOUDJEMA, A. PUKHOV, A. SEMENOV, 2008, "Dark matter direct detection rate in a generic model with micrOMEGAs2.2", arXiv:0803.2360.

G. JUNGMAN, M. KAMIONKOWSKI, AND K. GRIEST, 1996, "Supersymmetric Dark Matter", arxiv:9506380v1.

PATRICK J. FOX, RONI HARNIK, JOACHIM KOPP, AND YUHSIN TSAI, 2011, "Missing Energy Signatures of Dark Matter at the LHC", arXiv:1109.4398.

MARIA BELTRAN, DAN HOOPER, EDWARD W. KOLB, ZOSIA A. C. KRUSBERG AND TIM M. P. TAIT, 2010, "Maverick dark matter at colliders", arXiv:1002.4137v2.

PATRICK J. FOX, RONI HARNIK, REINARD PRIMULANDO AND CHIU-TIEN YU, 2012, "Taking a Razor to Dark Matter Parameter Space at the LHC", arXiv:1203:1662.

CMS COLLABORATION, 2011, "Search for New Physics with Monojet Final States in 5 fb−1 of pp collisions at ps=7 TeV", CMS Analysis Note AN-11-440.

CMS COLLABORATION, 2011, "Search for New Physics with a Monojet and Missing Transverse Energy in pp Collisions at $\sqrt{s}$= 7 TeV with 1.1 fb−1", CMS Physics Analysis Summary EXO-11-059.

CMS COLLABORATION, 2012, "Search for dark matter and large extra dimensions in monojet events in pp collisions at sqrt(s)= 7 TeV", arXiv:1206.5663.

CMS COLLABORATION, 2011, "Search for New Physics with Mono-Jet Final Sates in pp collisions at $\sqrt{s}$=7 TeV", CMS Analysis Note AN-11-024.

CMS COLLABORATION Collaboration, 2011, "Search for New Physics with a Mono-Jet and Missing Transverse Energy in pp Collisions at ps = 7 TeV", arXiv:1106.4775.

CMS COLLABORATION, 2009, "Search for Mono-Jet Final States from ADD Extra Dimensions", CMS Physics Analysis Summary EXO-08-011.

CMS COLLABORATION, 2009, “Search for Mono-Jet Final States from ADD Extra Dimensions at sqrt(s)=10 TeV”, CMS Physics Analysis Summary EXO-09-013.

P. J. FOX, R. HARNIK, J. KOPP ET AL., 2012, “Missing energy signatures of dark matter at the LHC”, arXiv:1109.4398.

H. GEORGI, 2007, Unparticle Physics, Phys. Rev. Lett. 98, 221601.

S. HOCHE, F. KRAUSS, N. LAVESSON ET AL., 2006, “Matching parton showers and matrix elements”, arXiv:hep-ph/0602031.

CMS COLLABORATION, 2010, “CMS tracking performance results from early LHC operation”, arXiv:1007.1988.

CMS COLLABORATION, 2009, “Particle–Flow Event Reconstruction in CMS and performance for Jets”, Taus, and E^T_{miss}, CMS Physics Analysis Summary CMS-PAS-PFT-09-001.

M. CACCIARI, G. P. SALAM, AND G. SOYEZ, 2008, “The anti-kt jet clustering algorithm”, arXiv:0802.1189.

CMS COLLABORATION, 2010, “Determination of the Jet Energy Scale in CMS with pp Collisions at $\sqrt{s}$ = 7 TeV”, CMS Physics Analysis Summary CMS-PAS-JME-10-010.

PARTICLE DATA GROUP COLLABORATION, 2010, “Review of Particle Physics”, J. Phys. G **37** 075021, doi:10.1088/0954-3899/37/7A/075021.

L. MONETA, K. CRANMER, G. SCHOTT ET AL., 2010, “The RooStats Project”, arXiv:1009.1003.

ADAM SZABELSKI, 2012, “Spin structure of the nucleon. The gluon contribution to the Sivers effect”.

J. ALWALL, P. DEMIN, S. DE VISSCHER, R. FREDERIX, M. HERQUET, F. MALTONI, T. PLEHN, D. L. RAINWATER, TIM STELZER, 2007, “MadGraph/MadEvent v4: The new web generation”.

CDMS COLLABORATION, 2011 “Results from a Low-Energy Analysis of the CDMS II GermaniumData”, Phys. Rev. Lett. 106 131302, doi:10.1103/PhysRevLett.106.131302, arXiv:1011.2482.

CDMS II COLLABORATION, 2010, “Dark Matter Search Results from the CDMS II Experiment”, Science 327. 1619, doi:10.1126/science.1186112, arXiv:http://www.sciencemag.org/content/327/5973/1619.full.pdf.

XENON100 COLLABORATION, 2011 “Dark Matter Results from 100 Live Days of XENON100 Data”, Phys. Rev. Lett. 107 131302, doi:10.1103/PhysRevLett.107.131302, arXiv:1104.2549.

COGENT COLLABORATION, 2011 “Results from a Search for Light-Mass Dark Matter with a p-Type Point Contact Germanium Detector”, Phys. Rev. Lett. 106 131301, doi:10.1103/PhysRevLett.106.131301, arXiv:1002.4703.

ICECUBE COLLABORATION, 2012 “Multi-year search for dark matter annihilations in the Sun with the AMANDA-II and IceCube detectors”, Phys. Rev. D 85 042002, doi:10.1103/PhysRevD.85.042002, arXiv:1112.1840.

SUPER-KAMIOKANDE COLLABORATION, 2011, “An Indirect Search for WIMPs in the Sun using3109.6 Days of Upward-going Muons in Super-Kamiokande”, Astrophys. J. 742 78, doi:10.1088/0004-637X/742/2/78, arXiv:1108.3384.

CDF COLLABORATION, 2012, “A Search for dark matter in events with one jet and missing transverse energy in $p\bar{p}$collisions at $\sqrt{s}$ = 1.96 TeV”, Phys. Rev. Lett. 108 211804,doi:10.1103/PhysRevLett.108.211804, arXiv:1203.0742.

M. FELIZARDO ET AL., 2012 “Final Analysis and Results of the Phase II SIMPLE Dark Matter Search”, Phys.Rev.Lett. 108 201302, doi:10.1103/PhysRevLett.108.201302, arXiv:1106.3014.

COUPP COLLABORATION COLLABORATION, 2012, “First Dark Matter Search Results from a 4-kg CF3I Bubble Chamber Operated in a Deep Underground Site”, Phys.Rev. D86 052001, doi:10.1103/PhysRevD.86.052001, arXiv:1204.3094

CDF COLLABORATION, 2012 “A Search for dark matter in events with one jet and missing transverse energy in $p\bar{p}$ collisions at $\sqrt{s}$ = 1.96 TeV”, Phys. Rev. Lett. 108 211804, doi:10.1103/PhysRevLett.108.211804, arXiv:1203.0742.

D0 COLLABORATION, 2003 “Search for large extra dimensions in the monojet + missing ET channel at DØ”, Phys. Rev. Lett. 90 251802, doi:10.1103/PhysRevLett.90.251802, arXiv:hep-ex/0302014.

LEP COLLABORATION, 2004, “Single- and multi-photon events with missing energy in e+e- collisions at LEP”, Phys. Lett. B 587 16, doi:10.1016/j.physletb.2004.01.010.

CURRICULUM VITAE

I was born at 1983 at Nevşehir. I graduated from Physics Departure at Mersin Universitesi at 2004. I took training lesson for learning english at Foreign Languages Teaching Research and Application Center from Middle East Technical University at 2005. I finished my master thesis at Mersin University at 2008. I am a PhD student at Cukurova University.

APPENDIXS

APPENDIX 1

Appendix 1.A

For a geodesic curve, Lagrange density is;

$$L(x^{\mu},\dot{x}^{\mu},\lambda)=\frac{1}{c}\left[g_{\beta\gamma}\frac{dx^{\beta}}{d\lambda}\frac{dx^{\gamma}}{d\lambda}\right]^{1/2}. \qquad 1.A.1$$

As you know, the Euler- Lagrange equations are given by;

$$\frac{\partial L}{\partial x^{\alpha}}=\frac{d}{d\lambda}\frac{\partial L}{\partial \dot{x}^{\alpha}}. \qquad 1.A.2$$

Substituting eq. 1.A.2 in eq. 1.A.1, we get following;

$$\frac{\partial L}{\partial x^{\alpha}}=\frac{1}{2c}\left[g_{\beta\gamma}\frac{dx^{\beta}}{d\lambda}\frac{dx^{\gamma}}{d\lambda}\right]^{-1/2}\frac{\partial g_{\beta\gamma}}{\partial x^{\alpha}}\frac{dx^{\beta}}{d\lambda}\frac{dx^{\gamma}}{d\lambda} \qquad 1.A.3$$

and

$$\frac{\partial L}{\partial \dot{x}^{\alpha}}=\frac{1}{2c}\left[g_{\beta\gamma}\frac{dx^{\beta}}{d\lambda}\frac{dx^{\gamma}}{d\lambda}\right]^{-\frac{1}{2}}2g_{\alpha\beta}\frac{dx^{\beta}}{d\lambda} \qquad 1.A.4$$

since

$$\frac{d\tau}{d\lambda}=\frac{1}{c}\left[g_{\beta\gamma}\frac{dx^{\beta}}{d\lambda}\frac{dx^{\gamma}}{d\lambda}\right]^{1/2} \qquad 1.A.5$$

we find;

$$\frac{\partial L}{\partial x^{\alpha}}=\frac{1}{2}\frac{d\lambda}{d\tau}\frac{\partial g_{\beta\gamma}}{\partial x^{\alpha}}\frac{dx^{\beta}}{d\lambda}\frac{dx^{\gamma}}{d\lambda} \qquad 1.A.6$$

$$\frac{\partial L}{\partial \dot{x}^{\alpha}}=\frac{d\lambda}{d\tau}g_{\alpha\beta}\frac{dx^{\beta}}{d\lambda}=g_{\alpha\gamma}\frac{dx^{\beta}}{d\tau} \qquad 1.A.7$$

so the Euler- Lagrange equations is;

$$\frac{d}{d\lambda}\left[g_{\alpha\beta}\frac{dx^{\beta}}{d\tau}\right]=\frac{1}{2}\frac{d\lambda}{d\tau}\frac{\partial g_{\beta\gamma}}{\partial x^{\alpha}}\frac{dx^{\beta}}{d\lambda}\frac{dx^{\gamma}}{d\lambda} \qquad 1.A.8$$

multiplying by $\frac{d\lambda}{d\tau}$, we get;

$$\frac{d}{d\tau}\left[g_{\alpha\beta}\frac{dx^{\beta}}{d\tau}\right]=\frac{1}{2}\frac{\partial g_{\beta\gamma}}{\partial x^{\alpha}}\frac{dx^{\beta}}{d\tau}\frac{dx^{\gamma}}{d\tau} \qquad 1.A.9$$

and using

$$\frac{dg_{\alpha\beta}}{d\tau}=\frac{\partial g_{\alpha\beta}}{\partial x^{\gamma}}\frac{dx^{\gamma}}{d\tau} \qquad 1.A.10$$

we get;

$$\frac{1}{2}\frac{\partial g_{\beta\gamma}}{\partial x^{\alpha}}\frac{dx^{\beta}}{d\tau}\frac{dx^{\gamma}}{d\tau}=g_{\alpha\beta}\frac{d^2x^{\beta}}{d\tau^2}+\frac{dg_{\beta\gamma}}{d\tau}\frac{dx^{\beta}}{d\tau}=g_{\alpha\beta}\frac{d^2x^{\beta}}{d\tau^2}+\frac{\partial g_{\alpha\beta}}{\partial x^{\gamma}}\frac{dx^{\gamma}}{d\tau}\frac{dx^{\beta}}{d\tau}$$

$$g_{\alpha\beta}\frac{d^2x^{\beta}}{d\tau^2}=-\left[\frac{\partial g_{\alpha\beta}}{\partial x^{\gamma}}-\frac{1}{2}\frac{\partial g_{\beta\gamma}}{\partial x^{\alpha}}\right]\frac{dx^{\beta}}{d\tau}\frac{dx^{\gamma}}{d\tau} \qquad 1.A.11$$

multiplying by $g^{\delta\alpha}$ gives;

$$\frac{d^2x^{\delta}}{d\tau^2}=-g^{\delta\alpha}\left[\frac{\partial g_{\alpha\beta}}{\partial x^{\gamma}}-\frac{1}{2}\frac{\partial g_{\beta\gamma}}{\partial x^{\alpha}}\right]\frac{dx^{\beta}}{d\tau}\frac{dx^{\gamma}}{d\tau}. \qquad 1.A.12$$

Now

$$\frac{\partial g_{\alpha\beta}}{\partial x^{\gamma}}\frac{dx^{\beta}}{d\tau}\frac{dx^{\gamma}}{d\tau}=\frac{1}{2}\left[\frac{\partial g_{\alpha\beta}}{\partial x^{\gamma}}\frac{dx^{\beta}}{d\tau}\frac{dx^{\gamma}}{d\tau}+\frac{\partial g_{\alpha\beta}}{\partial x^{\gamma}}\frac{dx^{\beta}}{d\tau}\frac{dx^{\gamma}}{d\tau}\right]$$

$$\frac{\partial g_{\alpha\beta}}{\partial x^{\gamma}}\frac{dx^{\beta}}{d\tau}\frac{dx^{\gamma}}{d\tau}=\frac{1}{2}\left[\frac{\partial g_{\alpha\beta}}{\partial x^{\gamma}}+\frac{\partial g_{\alpha\gamma}}{\partial x^{\beta}}\right]\frac{dx^{\beta}}{d\tau}\frac{dx^{\gamma}}{d\tau}. \qquad 1.A.13$$

Using the above result gives us;

$$\frac{d^2x^\delta}{d\tau^2} = -\frac{1}{2}g^{\delta\alpha}\left[\frac{\partial g_{\alpha\beta}}{\partial x^\gamma} + \frac{\partial g_{\alpha\gamma}}{\partial x^\beta} - \frac{\partial g_{\beta\gamma}}{\partial x^\alpha}\right]\frac{dx^\beta}{d\tau}\frac{dx^\gamma}{d\tau}$$

$$\frac{d^2x^\delta}{d\tau^2} = -\Gamma^\delta_{\beta\gamma}\frac{dx^\beta}{d\tau}\frac{dx^\gamma}{d\tau} \qquad 1.A.14$$

where $\Gamma^\delta_{\beta\gamma}$ is Christoffel symbols. So, we found the geodesic equation;

$$\frac{d^2x^\delta}{d\tau^2} + \Gamma^\delta_{\beta\gamma}\frac{dx^\beta}{d\tau}\frac{dx^\gamma}{d\tau} = 0. \qquad 1.A.15$$

Appendix 1.B

$$I = \int_0^\infty \frac{x^3}{e^x - 1}dx. \qquad 1.B.1$$

To solve this integral, we need to introduce new definition;

$$\frac{1}{e^x-1} = \frac{e^{-x}}{1-e^{-x}} = \sum_{n=1}^\infty e^{-n\,x}. \qquad 1.B.2$$

Plugging this equation into eq. 1.B.1, we get;

$$I = \sum_{n=1}^\infty \int_0^\infty x^3 e^{-n\,x}dx. \qquad 1.B.3$$

We have evaluated this integral three times by parts in order to solve this integral. If we do so, we find;

$$I = 6\sum_{n=1}^\infty \frac{1}{n^4} \qquad 1.B.4$$

where $\sum_{\mathrm{n}=1}^\infty \frac{1}{\mathrm{n}^4}$ is a well-known sum, Riemann-Zeta (4), that evaluates to $\frac{\pi^4}{90}$. So, result of eq. 1.B.1 is;

$$I = \int_0^\infty \frac{x^3}{e^x - 1} dx = \frac{\pi^4}{15}. \qquad 1.B.5$$

Appendix 1.C

$$I = \int_0^\infty \frac{x^3}{e^x + 1} dx \qquad 1.C.1$$

This integral is defined for fermion system. Now, we need to translate it to boson case. For this, we could use;

$$\frac{1}{e^x + 1} = \frac{1}{e^x - 1} - \frac{2}{e^{2x} - 1}. \qquad 1.C.2$$

If this equation is substituted into eq. 1.C.1 one, we get;

$$I = \int_0^\infty \frac{x^3}{e^x - 1} dx - 2 \int_0^\infty \frac{x^3}{e^{2x} - 1} dx. \qquad 1.C.3$$

First term is same as eq. 1.B.5. Now, we try to understand second term. Let's use same trick as eq. 1.B.2;

$$\frac{1}{e^{2x} - 1} = \frac{e^{-2x}}{1 - e^{-2x}} = \sum_{n=1}^\infty e^{-2n\,x}$$
$$\rightarrow \int_0^\infty \frac{x^3}{e^{2x} - 1} dx = \sum_{n=1}^\infty \int_0^\infty x^3\, e^{-2n\,x} dx = \left(\frac{1}{2}\right)^4 \frac{\pi^4}{15}. \qquad 1.C.4$$

In this case, result of eq. 1.C.3 integral becomes;

$$I = \int_0^\infty \frac{x^3}{e^x - 1} dx - 2 \int_0^\infty \frac{x^3}{e^{2x} - 1} dx = \frac{\pi^4}{15} - 2\left(\frac{1}{2}\right)^4 \frac{\pi^4}{15} = \frac{7}{8} \frac{\pi^4}{15}. \qquad 1.C.5$$

APPENDIX 1

Appendix 1.D

Expansion is adiabatic for Robertson-Walker metric. In this case, first law for thermodynamics can be written as;

$$\frac{dE}{dt} + p\frac{dV}{dt} = 0 \qquad 1.D.1$$

where $E = \rho\, V$ and $V = \frac{4}{3}\pi\, a^3$. So, we get;

$$\frac{dE}{dt} = \frac{4}{3}\pi\, a^3 \frac{d\rho}{dt} + 4\pi a^2 \dot{a}\, \rho$$

$$\frac{dV}{dt} = 4\pi a^2 \dot{a}.$$

When we use these results in eq. 1.D.1, we find;

$$\frac{d\rho}{dt} + 3(\rho + P)\frac{\dot{a}}{a} = 0. \qquad 1.D.2$$

This is so called the continuity equation.

Appendix 1.E

Pressure is defined as;

$$P = \frac{g}{(2\pi)^3}\int d^3p\;\; f(p)\frac{p^2}{3E} \qquad 1.E.1$$

where $f(p) = \frac{1}{e^{(E(p)-\mu)}/_{T \pm 1}}$. Differentiating eq. 1.E.1 with respect to T and using $\mu = 0$, we get;

$$\frac{dP}{dT} = \frac{g}{(2\pi)^3}\int d^3p \frac{p^2}{3E}\frac{df}{dT}$$

$$\frac{dP}{dT} = \frac{4\pi g}{(2\pi)^3}\int dp \frac{p^4}{3E}\;\frac{E}{T^2} f^2 e^{E}/_{T}. \qquad 1.E.2$$

Here, we need to use new variable to be able to solve this integral.

$$\frac{df}{dp} = -\frac{1}{T}\frac{dE}{dp}f^2 e^{E/T} = -\frac{p}{ET}f^2 e^{E/T}$$

$$f^2 e^{E/T} = -\frac{ET}{p}\frac{df}{dp} \qquad 1.E.3$$

where we used $v = \frac{p}{E}$. Then, eq. 1.E.2 becomes;

$$\frac{dP}{dT} = -\frac{4\pi g}{3T(2\pi)^3}\int dp\, p^3 E\,\frac{df}{dp}.$$

Integrating by parts, we get;

$$u = p^3 E \qquad du = 3p^2 E\, dp + p^3\frac{dE}{dp}\, dp \qquad 1.E.4$$

$$dv = dp\,\frac{df}{dp} \qquad v = f \qquad 1.E.5$$

So, integral becomes;

$$\frac{dP}{dT} = \frac{4\pi g}{3T(2\pi)^3}\left\{3\int dp\, f p^2 E + \int dp\, f p^3\frac{dE}{dp}\right\}$$

$$\frac{dP}{dT} = \frac{1}{T}\frac{g}{(2\pi)^3}\int dp\, f\, p^2 E\int d\Omega + \frac{1}{T}\frac{g}{(2\pi)^3}\int dp\, f\,\frac{p^3}{3}\frac{dE}{dp}\int d\Omega$$

$$\frac{dP}{dT} = \frac{1}{T}\frac{g}{(2\pi)^3}\int f\, E\, d^3p + \frac{1}{T}\frac{g}{(2\pi)^3}\int\frac{p^2}{3E}f\, d^3p$$

$$\frac{dP}{dT} = \frac{\rho + P}{T} \qquad 1.E.6$$

Appendix 1.F

The action of the Liouville operator is;

$$\hat{L}f_i = E\frac{\partial f_i}{\partial t} - \frac{\dot{a}}{a}p^2\frac{\partial f_i}{\partial E}. \qquad 1.F.1$$

When we divide both sides with E, we find;

APPENDIX 1

$$\frac{\hat{L}f_i}{E} = \frac{\partial f_i}{\partial t} - \frac{\dot{a}}{a}\frac{p^2}{E}\frac{\partial f_i}{\partial E} = \frac{\partial f_i}{\partial t} - \frac{\dot{a}}{a}p\frac{\partial f_i}{\partial p}.$$

By integrating this result, we get;

$$I = \frac{g}{(2\pi)^3}\left\{\int \frac{\partial f_i}{\partial t}\, d^3p - \frac{\dot{a}}{a}\int p\frac{\partial f_i}{\partial p}d^3p\right\}. \qquad 1.F.2$$

This integral has two parts. Let's try to solve each part separately.

First Part;

$$I_1 = \frac{g}{(2\pi)^3}\int \frac{\partial f_i}{\partial t}\, d^3p = \frac{d}{dt}\left\{\frac{g}{(2\pi)^3}\int f_i\, d^3p\right\} = \frac{d}{dt}\eta_i$$

Second Part;

$$I_2 = \frac{g}{(2\pi)^3}\int p\frac{\partial f_i}{\partial E}d^3p = \frac{g}{(2\pi)^3}\int p^3\frac{\partial f_i}{\partial p}dp\int d\Omega.$$

Integrating by parts, we get;

$$p^3 = u \qquad\qquad 3p^2dp = du$$

$$\frac{\partial f_i}{\partial p}dp = dv \qquad\qquad v = f_i$$

$$\rightarrow\ \frac{g}{(2\pi)^3}\frac{\dot{a}}{a}\left[p^3f_i|_0^\infty - 3\int p^2f_idp\int d\Omega\right] = -3\frac{\dot{a}}{a}\frac{g}{(2\pi)^3}\int f_id^3p = -3\frac{\dot{a}}{a}\eta_i. \qquad 1.F.3$$

So, the result becomes;

$$I = \frac{d}{dt}\eta_i - 3\frac{\dot{a}}{a}\eta_i = \frac{1}{a^3}\frac{d}{dt}(a^3\eta_i). \qquad 1.F.4$$

Appendix 1.G

Let's define new variable using temperature;

$$x = \frac{m}{T}.$$

By making derivative with temperature, we find;

APPENDIX 1

$$\frac{dx}{dt} = \frac{1}{T^2}\left(T\frac{dm}{dt} - m\frac{dT}{dt}\right) = -\frac{m}{T}\frac{1}{T}\frac{dT}{dt} = -\frac{1}{T}\frac{dT}{dt}x. \qquad 1.G.1$$

Now, we try to write this equation in term of Hubble constant. So;

$$a(t) = \frac{s_e^{1/3}}{M_{pl}}\left(\frac{45}{2\pi^2 g_{*S}}\right)^{1/12}\left(\frac{g_*}{g_{*S}}\right)^{1/4}\left(\frac{t}{t_{pl}}\right)^{1/2} = K\,t^{1/2} \qquad 1.G.2$$

where $K = \frac{s_e^{1/3}}{M_{pl}}\left(\frac{45}{2\pi^2 g_{*S}}\right)^{1/12}\left(\frac{g_*}{g_{*S}}\right)^{1/4}\left(\frac{1}{t_{pl}}\right)^{1/2}$. In this case, we can rewrite as;

$$H = \frac{1}{a}\frac{da}{dt} = \frac{1}{2t}\ . \qquad 1.G.3$$

Also, there is a relation between temperature and time. So;

$$H = \sqrt{\frac{\pi^2}{90}\frac{g_*}{M_{pl}^2}}T^2 = M\,T^2 \qquad 1.G.4$$

where $M = \sqrt{\frac{\pi^2}{90}\frac{g_*}{M_{pl}^2}}$. By using eq. 1.G.4 and eq. 1.G.3, temperature is;

$$T = \sqrt{\frac{1}{2M}}\ t^{-1/2} \quad \rightarrow \quad \frac{1}{T}\frac{dT}{dt} = -\frac{1}{2}\sqrt{\frac{1}{2M}}\ t^{-3/2} = -\frac{1}{2t} = -H. \qquad 1.G.5$$

Eq. 1.G.5 should be put into eq. 1.G.1. So, we find;

$$\frac{dx}{dt} = Hx. \qquad 1.G.6$$

Appendix 1.H

The first law of thermodynamics for cosmological fluid in a ΔV connects infinitesimal changes in volume $d(\Delta V)$ to the corresponding infinitesimal change in the total energy $d(\Delta E)$;

$$d(\Delta E) = -p\, d\left(\Delta V_{phy}\right) \qquad 1.H.1$$

where p is the pressure exerted by matter in the volume. The energy in the volume, ΔE, is $\rho\, \Delta V$ where ρ is the total energy density. There is a connection between physical and coordinate volume which is given by;

$$\Delta V_{phy} = a^3(t)\, \Delta V_{cor}. \qquad 1.H.2$$

So, if this equation is substituted to eq. 1.H.1, we get;

$$d(\rho\, a^3\, \Delta V_{cor}) = -p\, d(a^3 \Delta V_{cor})$$
$$\frac{d}{dt}(\rho\, a^3\,) = -p\, \frac{d}{dt}(a^3). \qquad 1.H.3$$

This is known as first law of thermodynamics for cosmology.

- Matter in the galaxies is approximated by a pressureless gas. So, eq. 1.H.3 becomes;

$$\frac{d}{dt}(\rho\, a^3\,) = 0. \qquad 1.H.4$$

Here, we can apply integral;

$$\int_{t_0}^{t} d(\rho\, a^3\,) = \int_{t_0}^{t} 0 dt$$
$$\rho(t)\, a^3(t) - \rho(t_0)\, a^3(t_0) = 0$$

$$\rho(t) = \rho(t_0)\ \left(\frac{a(t_0)}{a(t)}\right)^3. \qquad 1.H.5$$

For matter dominated universe, we can write energy-momentum equation like;

$$E = \sqrt{p^2 + m^2}. \qquad 1.H.6$$

Here, for p ≪ m, eq. 1.H.6 becomes;

$$E = \sqrt{p^2 + m^2} = m\left(1 + \left(\frac{p}{m}\right)^2\right)^{1/2} = m + \frac{m}{2}\left(\frac{p}{m}\right)^2$$
$$E = \sqrt{p^2 + m^2} = m\left(1 + \left(\frac{p}{m}\right)^2\right)^{1/2} = m + \frac{p}{2m} \cong m. \qquad 1.H.7$$

So, we can write energy density for this case as;

$$\rho(t_0) = \frac{g}{(2\pi)^3}\int d^3p\, f(p)\, E(p). \qquad 1.H.8$$

Adding eq. 1.H.7 to eq. 1.H.8, we get;

$$\rho(t_0) = m\frac{g}{(2\pi)^3}\int d^3p\, f(p)$$
$$\rho(t_0) = m\, n(t_0). \qquad 1.H.9$$

So, when we put eq. 1.H.9 into eq. 1.H.5, we find;

$$\rho(t) = m\, n(t_0)\ \left(\frac{a(t_0)}{a(t)}\right)^3. \qquad 1.H.10$$

• We introduced relation between pressure and energy density for radiation dominated universe;

$$p = \frac{1}{3}\rho. \qquad 1.H.11$$

This equation should be added into eq. 1.H.3. So, we get;

$$\rho \frac{d}{dt}(a^3) + a^3 \frac{d\rho}{dt} = -\frac{1}{3}\rho \ \frac{d}{dt}(a^3)$$

$$a^3 d\rho = -\frac{4}{3}\rho \ d(a^3)$$

$$\frac{d\rho}{\rho} = -\frac{4}{3}\frac{d(a^3)}{a^3}$$

$$\int_{t_0}^{t} d\ ln\, \rho = -\frac{4}{3}\int_{t_0}^{t} d\ ln\, a^3$$

$$ln\, \rho(t) - ln\, \rho(t_0) = -\frac{4}{3}\{ln\, a^3(t) - ln\, a^3(t_0)\}$$

$$ln\frac{\rho(t)}{\rho(t_0)} = -\frac{4}{3}\, ln\left(\frac{a(t)}{a(t_0)}\right)^3$$

$$ln\frac{\rho(t)}{\rho(t_0)} = ln\left(\frac{a(t)}{a(t_0)}\right)^{-4}$$

$$\rho(t) = \rho(t_0)\left(\frac{a(t_0)}{a(t)}\right)^4. \qquad 1.H.12$$

This is known as energy density for radiation dominated universe.

APPENDIX 2

Appendix 2.A

We consider the "OR" case between 3 triggers as follows;

1. HLT_MET120_HBHENoiseCleaned
    - CaloMET > 120 GeV
    - HLT HBHENoiseCleaned (Looser than offline level)
    - Unprescaled for all runs
2. HLT_MonoCentralPFJet80_PFMETnoMu95_NHEF0p95
    - P_T of leading P_T PFJet > 80 GeV/c
    - $|\eta$(leading P_T PFJet)$| < 2.6$
    - Neutral Hadron Energy Fraction of the leading P_T PFJet < 0.95
    - PFMETnoMu > 95 GeV
    - DeltaPhi(1st leading P_T PFJet, 2nd leading P_T PFJet) < 2.9
    - Unprescaled for RunA and RunB
3. HLT_MonoCentralPFJet80_PFMETnoMu105_NHEF0p95
    - P_T of leading P_T PFJet > 80GeV/c
    - $|\eta$(leading P_T PFJet)$| < 2.6$
    - Neutral Hadron Energy Fraction of the leading P_T PFJet < 0.95
    - PFMETnoMu > 105 GeV
    - Unprescaled for RunC and RunD

Appendix 2.B

Table 4.15. Selection criteria for selecting signal events.

Event Selection
$\mathrm{E_T^{miss}} + \mathrm{P_T}(\mu) > 200\, {}^{GeV}\!/_{c}$
Noise Cleaning (leading jet CHF > 0.2, NEF < 0.7, NHF < 0.7)
$P_T(j_1)$ *> 110 GeV/c,* $\lvert\eta\rvert$*< 2*
$N_{jets} \leq 2$
$\Delta\varphi(j_1, j_2)$
Lepton Veto
$E_T^{miss} > 250\, {}^{GeV}\!/_{c}$
$E_T^{miss} > 300\, {}^{GeV}\!/_{c}$
$E_T^{miss} > 350\, {}^{GeV}\!/_{c}$
$E_T^{miss} > 400\, {}^{GeV}\!/_{c}$
$E_T^{miss} > 450\, {}^{GeV}\!/_{c}$
$E_T^{miss} > 500\, {}^{GeV}\!/_{c}$
$E_T^{miss} > 550\, {}^{GeV}\!/_{c}$

Appendix 2.C

Table 4.16. Selection criteria used in the lepton veto.

Muon Selection	**Electron Selection**	**Tau Selection**
$P_T > 10$ Global OR Tracker	$P_T > 10$ not in *1.4442 <* η *< 1.5666* *R < 0.2* WP95	$P_T > 10$, $\lvert\eta\rvert < 2.3$ HPS tau LooseCombinedIsolation DeltaBetaCorr DecayModeFinding Loose electron discriminant Tight muon discriminant

Table 4.17. Selection criteria for selecting muons for Z($\mu\mu$) and W($\mu\nu$) control sample used in the data-driven estimation of backgrounds.

Muon Selection
$P_T > 10,\ \lvert\eta\rvert < 2.1$
$R < 0.2$
Global and Tracker
$\lvert \mathrm{d_{xy}} \rvert < 0.2\ mm$
$\chi^2/_{\mathrm{dof}} < 10$
Number of matches in muon stations > 1
Number of pixel hits > 0
Number of standalone hits > 0
Number of total hits > 10

TheW+jets and Z($\nu\nu$)+jets processes are normalized using the scale factor obtained from their data driven predictions for a E_T^{miss} cut of 250 GeV. The Z+jets events are normalized using a scale factor of 1.036 which is obtained from a ratio of Z($\mu\mu$) events in data and MC at a E_T^{miss} cut of 250 GeV. The normalization factor of $\mathrm{t\bar{t}}$ events is obtained by selecting a sample of events; a data-MC comparison shows that the LO MC cross-section for $\mathrm{t\bar{t}}$ events needs to be scaled by a factor of 1.6 to match the data. This is consistent with the 1.65 that is obtained in the measurement of the $\mathrm{t\bar{t}}$ cross section. The LO cross section for QCD events is scaled by a factor of 1.27 which is taken from the dijet resonance analysis. The NLO cross section is used for single top which requires a scaling of the LO cross section by 1.17. However, the event yields for the W+jets and Z($\nu\nu$) processes in the cut flow shown in the Table 4.3 are normalised to their LO cross sections. The W+jets and Z+jets processes in the Tables 4.4 and 4.5 are also normalized to their LO cross sections.

Appendix 2.D

The E_T^{miss} cut was optimised by using a representative dark matter signal sample (axial vector mediator with DM mass of 1 GeV). The expected limit for DM as a function of the E_T^{miss} cut is shown in Fig. 4.14. The measured systematic uncertainties on the signal from the previous analysis using 5 fb^{-1} of 7 TeV data were used to calculate the expected limit. The expected limit as a function of the E_T^{miss} cut for two representative ADD signal points is shown in Fig. 4.15.

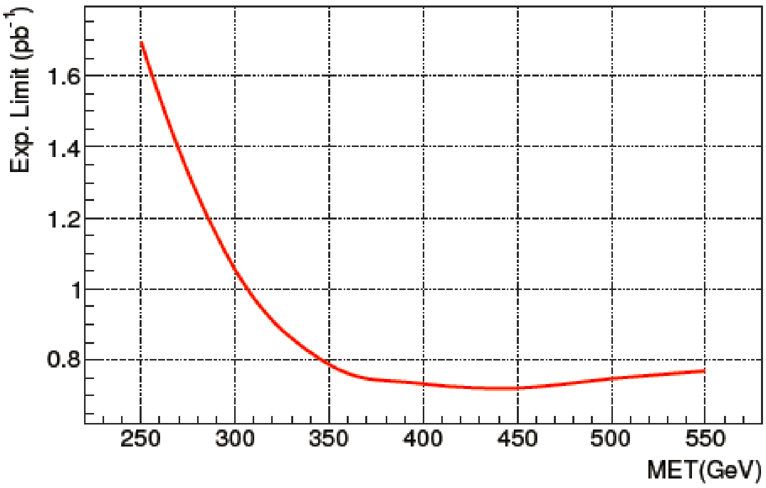

Figure 4.14. Expected limit as a function of the cut for DM.

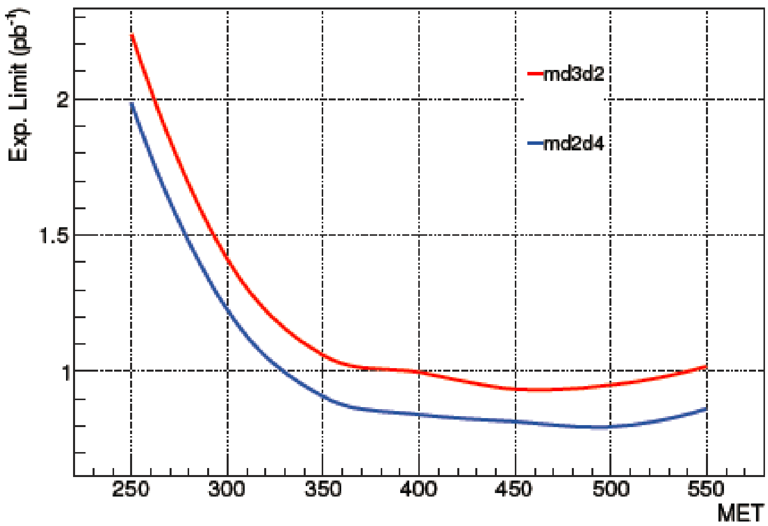

Figure 4.15. Expected limit as a function of the cut for ADD.

Appendix 2.E

Table 4.18. Acceptance of the DM signal points and the uncertainty on the acceptance from the Jet Energy Scale and PDFs.

Signal(%)	A	JES	PDF	Total Error
DM AV, $M_\chi = 1$	1.654	-5.364 /+ 5.984	-0.047 /+ 0.054	-5.365 /+ 5.984
DM AV, $M_\chi = 10$	1.641	-5.365 /+ 5.894	-0.055 /+ 0.064	-5.366 /+ 5.895
DM AV, $M_\chi = 100$	1.967	-5.932 /+ 5.776	-0.179 /+ 0.209	-5.939 /+ 5.786
DM AV, $M_\chi = 200$	2.432	-5.422 /+ 5.609	-0.319 /+ 0.376	-5.447 /+ 5.643
DM AV, $M_\chi = 300$	2.758	-6.013 /+ 5.363	-0.518 /+ 0.590	-6.073 /+ 5.450
DM AV, $M_\chi = 400$	3.025	-4.737 /+ 5.523	-0.751 /+ 0.855	-4.895 /+ 5.699
DM AV, $M_\chi = 700$	3.453	-4.226 /+ 5.479	-1.332 /+ 1.387	-4.760 /+ 5.935
DM AV, $M_\chi = 1000$	3.608	-5.180 /+ 4.654	-2.022 /+ 2.124	-6.156 /+ 5.820
DM V, $M_\chi = 1$	1.605	-5.872 /+ 4.418	-0.047 /+ 0.055	-5.872 /+ 4.419
DM V, $M_\chi = 10$	1.671	-4.777 /+ 4.533	-0.056 /+ 0.064	-4.778 /+ 4.535
DM V, $M_\chi = 100$	1.801	-4.820 /+ 4.974	-0.118 /+ 0.138	-4.824 /+ 4.979
DM V, $M_\chi = 200$	2.034	-5.019 /+ 5.545	-0.279 /+ 0.329	-5.040 /+ 5.571
DM V, $M_\chi = 300$	2.042	-5.418 /+ 6.450	-0.255 /+ 0.301	-5.434 /+ 6.469
DM V, $M_\chi = 400$	2.795	-4.648 /+ 4.745	-0.563 /+ 0.633	-4.740 /+ 4.858
DM V, $M_\chi = 700$	3.306	-4.724 /+ 4.614	-1.404 /+ 1.430	-5.258 /+ 5.179
DM V, $M_\chi = 1000$	3.572	-5.047 /+ 4.925	-1.942 /+ 2.084	-5.973 /+ 6.000

Table 4.19. Acceptance of the ADD signal points and the uncertainty on the acceptance from the Jet Energy Scale and PDFs.

Signal (%)	A	JES	PDF	Total Error
$M_D = 3, \delta = 2$	3.008	-6.209 /+ 5.878	-3.345 /+ 4.215	-8.295 /+ 9.090
$M_D = 4, \delta = 2$	2.933	-6.102 /+ 5.130	-3.439 /+ 4.357	-8.321 /+ 8.813
$M_D = 2, \delta = 3$	3.403	-6.325 /+ 5.024	-1.744 /+ 2.164	-6.945 /+ 6.157
$M_D = 3, \delta = 3$	3.845	-5.376 /+ 5.029	-1.960 / + 2.446	-6.269 /+ 6.440
$M_D = 4, \delta = 3$	3.907	-5.188 /+ 5.328	-2.377 /+ 3.046	-6.497 /+ 7.314
$M_D = 2, \delta = 4$	3.613	-6.281 /+ 5.879	-1.155 /+ 1.181	-6.562 /+ 6.191
$M_D = 3, \delta = 4$	4.365	-4.633 /+ 5.538	-1.380 /+ 1.385	-5.159 /+ 5.989
$M_D = 4, \delta = 4$	4.450	-5.063 /+ 5.267	-1.611 /+ 1.807	-5.715 /+ 6.047
$M_D = 1, \delta = 5$	1.817	-6.267 /+ 6.752	-1.620 /+ 1.995	-6.810 /+ 7.507
$M_D = 2, \delta = 5$	3.574	-5.553 /+ 5.326	-1.653 /+ 1.534	-6.183 /+ 5.893
$M_D = 3, \delta = 5$	4.450	-5.301 /+ 6.494	-1.714 /+ 1.612	-6.004 /+ 7.014
$M_D = 4, \delta = 5$	4.536	-5.430 /+ 5.998	-1.720 /+ 1.634	-6.123 /+ 6.573
$M_D = 1, \delta = 6$	1.969	-5.886 /+ 6.812	-1.726 /+ 2.139	-6.535 /+ 7.667
$M_D = 2, \delta = 6$	3.615	-5.527 /+ 5.722	-2.064 /+ 1.907	-6.487 /+ 6.526
$M_D = 3, \delta = 6$	4.253	-5.582 /+ 5.436	-2.683 /+ 2.609	-7.116 /+ 6.926
$M_D = 4, \delta = 6$	4.647	-5.220 /+ 5.468	-2.210 /+ 2.098	-6.361 /+ 6.466

Tables 4.18 and 4.19 show the acceptance of the signal for Dark matter models with vector and axial vector operators and the mass of the DM varied between 1 GeV and 1 TeV and also ADD with δ varied between 2 and 6. The systematic uncertainties on the acceptance from the Jet Energy Scale and PDFs are also shown, together with the total error which ranges between 5% to 8% for ADD and 4% to 6% for DM.

Appendix 2.F

The E_T^{miss} energy scale is cross-checked using a sample of Z($\mu\mu$) events where the full monojet selection, except the lepton veto, has been applied. E_T^{miss} is resolved into directions parallel and perpendicular to the Z as shown in Fig. 4.16. The energy scale is then checked by plotting the ratio of the parallel E_T^{miss} to the magnitude of the Z_T. The distributions of this ratio for a cut of 250 $\mathrm{GeV/c}$ on the Z_T is shown for data in Fig. 4.17 and MC in Fig. 4.18. The E_T^{miss} scales are measured to be (0.2 ± 0.2)% for data and (1.0 ± 0.1)% for MC which are consistent with the recommended JES uncertainty (CMS Collaboration, 2010).

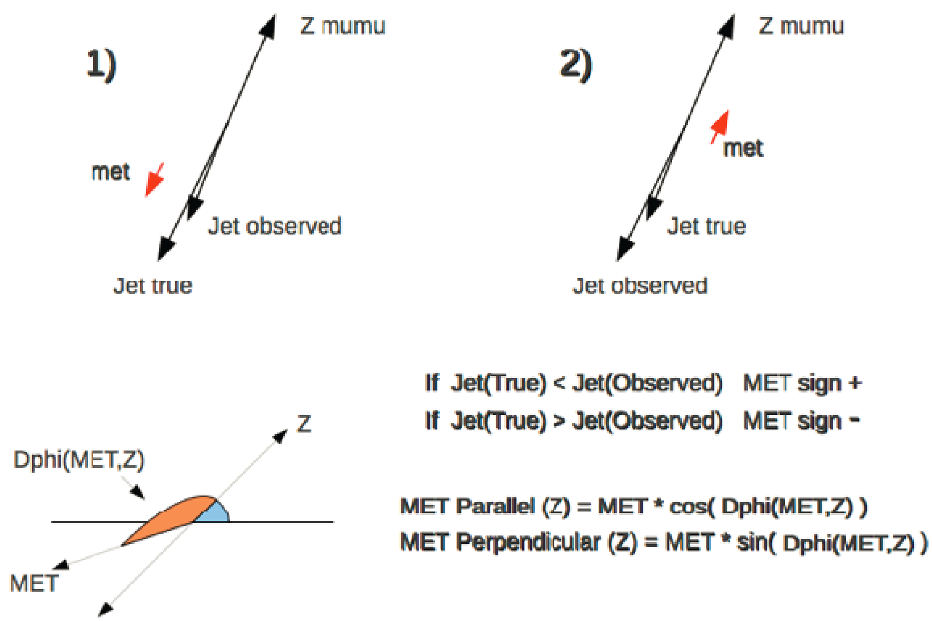

Figure 4.16. Cross check of the MET energy scale.

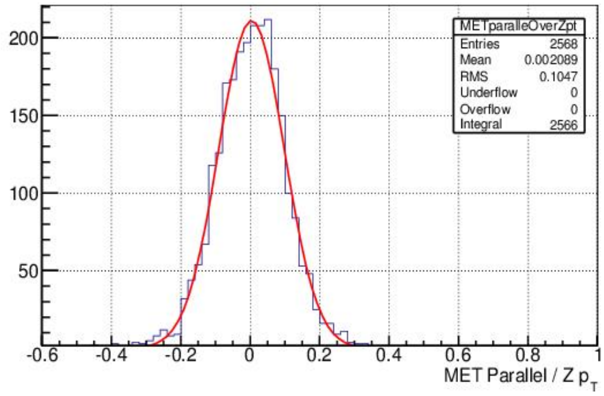

Figure 4.17. Cross check of the MET energy scale for data.

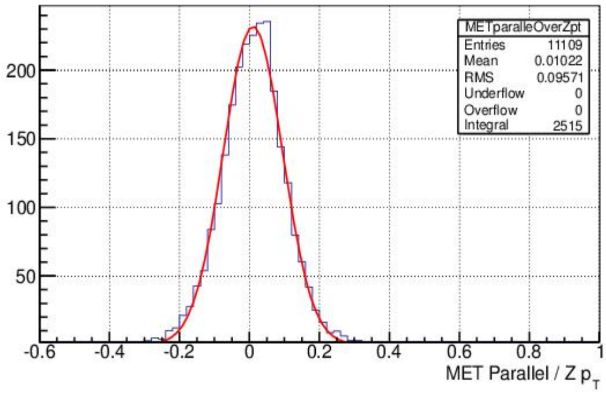

Figure 4.18. Cross check of the MET energy scale for MC.